Journal of Photochemistry & Photobiology, C: Photochemistry Reviews 67 (2026) 100758

Contents lists available at ScienceDirect

Journal of Photochemistry & Photobiology, C: Photochemistry Reviews

journal homepage: www.elsevier.com/locate/jphotochemrev

Synthesis, optical properties, and biological applications of luminescent nanomaterials: Paradigm shift towards safer semiconductor quantum dots and nanoparticles

S L Aneesha [a], Jeladhara Sobhanan [a,b], Jose V. Rival [c], Edakkattuparambil Sidharth Shibu [c], Abdulaziz Anas [d], Bengang Xing [e], Vasudevanpillai Biju [a,f,*]

[a] Graduate School of Environmental Science, Hokkaido University, Japan
[b] Occupational Health and Safety, Virginia Commonwealth University, United States
[c] Department of Nanoscience and Technology, University of Calicut, India
[d] CSIR-National Institute of Oceanography, Cochin, India
[e] Department of Applied Biology and Chemical Technology, The Hong Kong Polytechnic University, Hong Kong
[f] Research Institute of Electronic Science, Hokkaido University, Japan

ARTICLE INFO

Keywords:
Quantum dots
Bioimaging
Photosensitization
Reactive oxygen species
Photodynamic therapy

ABSTRACT

Quantum dots (QDs) are semiconductor nanocrystals (NCs) with excellent optical and electronic properties arising from strong exciton confinement. Their biomedical and technological potential have significantly contributed to nanotechnology. The QD field has evolved from traditional toxic heavy metal-based elements, such as Cd, Pb, Hg, chalcogens, and halogens, to a new focus on less-toxic alternatives from I-VI, III-V, and I-III-VI groups. Despite their attractive optical properties, the toxicity of conventional QDs limits their biomedical and clinical prospects. Recently, safer QDs based on chalcogenides of In, Ag, Ga, and Cu have been developed, offering absorption and emission in the biological I and II windows. Advances in synthesis, shell preparation, ligand exchange, and bioconjugation have further tailored these QDs for stable and specific applications, including targeted multimodal bioimaging, drug delivery, phototherapy, and image-guided therapy with high spatial, spectral, and temporal resolutions. This review highlights the transition from classical cadmium-, lead-, and mercury-based QDs to less-toxic silver-, copper-, and indium-based QDs for bioimaging and photodynamic therapy (PDT). First, we touch on classical developments in the synthesis, optical properties, and biological applications of heavy metals (Cd/Pb/Hg)-based QDs, before focusing the major parts on the synthesis, optical properties, bioconjugation, and bioimaging aspects of core only and core-shell nanomaterials from I-VI (Ag_2S, Ag_2Se, and Ag_2Te), III-V (GaN, GaP, GaAs, GaSb, InN, InP, InAs, and InSb), and I-III-VI ($CuInS_2$, $CuInSe_2$, $CuInTe_2$, $CuGaS_2$, $CuGaSe_2$, $AgGaS_2$, $AgGaSe_2$, $AgInS_2$, $AgInSe_2$, and $AgInTe_2$) groups. The discussion proceeds to the PDT potential of QDs, a minimally invasive method for treating cancers and infections that uses light-activated PSs to generate ROS, such as singlet oxygen ($^1O_2$) and superoxide ($O_2\bullet^-$). We emphasize the importance of these nanomaterials over traditional organic PSs, such as porphyrins and phthalocyanines, which suffer from poor stability, narrow-band light absorption, and limited tissue penetration. Conversely, QDs offer broad and NIR light absorption, high photostability, and tunable surfaces for bioconjugation and targeted, image-guided therapy. The review highlights the mechanism and applications of III–V and I–III–VI QDs in tumor and infection treatment, while addressing challenges such as toxicity, hypoxia tolerance, and clinical translation toward multifunctional theragnostic systems, highlighting the pathway for safer, more versatile tools in clinical testing, imaging, and therapy, driving future innovations in healthcare.

* Corresponding author at: Graduate School of Environmental Science, Hokkaido University, Japan.
E-mail address: biju@es.hokudai.ac.jp (V. Biju).

https://doi.org/10.1016/j.jphotochemrev.2026.100758
Received 13 March 2026; Received in revised form 26 April 2026; Accepted 7 May 2026
Available online 15 May 2026

1. Introduction

Quantum dots (QDs) represent a significant advancement in nanotechnology, offering unique properties and promising applications across optoelectronics, photovoltaics, and biomedicine. The recognition of their transformative potential through the Nobel Prize in 2023 underscored their importance in scientific research and technological innovation. One of the defining features of QDs is their quantum confinement effect, which produces discrete energy levels for electrons and holes within the QD structure and results in size-dependent optoelectronic properties. Earlier studies reported that Cd-, Pb-, and Hg-based QDs replaced fluorescent dye molecules in cell, molecular, and *in vivo* imaging [1–4].

In 1981, Alexey Ekimov first demonstrated blue photoluminescence (PL) from metal halide nanoparticles [5] (NPs). Subsequently, Luis E. Brus significantly contributed to the theoretical understanding of QDs, particularly their electronic structure and particle size [6]. Brus's theoretical models elucidated how the QD size affects their electronic bandgap and the quantization of energy levels. As the QD size decreases, the energy levels of electrons and holes become discrete. The valence band (hole) and conduction band (electron) states of CdSe QDs are shown as an example, where the band-edge states become nondegenerate (Fig. 1a) by crystal field splitting, e-h exchange perturbation, and spin-orbit coupling (SOC).

The SOC is negligibly small for CdSe QDs. This phenomenon resulted in size-dependent bandgap energies, with smaller QDs exhibiting larger band gaps due to significant quantum confinement energy [7,8]. As a result, smaller QDs emit in the shorter (blue or ultraviolet) and larger QDs in the longer (red or near-infrared, NIR) sides of the electromagnetic spectrum. The size-dependent PL color and absorption, and PL spectra of CdSe QDs [9,10] are shown in Fig. 1b, c. Advancements in metal chalcogenide QDs have enabled analogous strategies, such as hot injection and ligand-assisted methods, to prepare brilliantly luminescent QDs with tunable band gaps and emission in the UV-Vis-NIR region. Although these materials show well-defined crystal structures and quantitative PL, they have not been appealing for bioimaging or phototherapy due to concerns about stability and toxicity.

Early advances in the synthesis of cadmium chalcogenide QDs critically influenced the development of their less-toxic analogs [11–14]. Brus's lab performed groundbreaking research on the synthesis of colloidal QDs. Subsequently, the colloidal synthesis technique gained widespread attention, with the first example demonstrated by Murray et al., where CdX (X = S/Se/Te) QDs were synthesized from $(CH_3)_2Cd$ ($CdMe_2$) and different chalcogenide precursors by high temperature crystal nucleation-growth control, which provided white light-emitting samples with widely distributed particle sizes. However, they successfully demonstrated the relationship between quantum size and optical bandgap *via* size-selective precipitation [15]. Different groups later adopted various strategies to modify and optimize the QD synthesis procedure. For example, Katari et al. modified the QD synthesis by optimizing the temperature for injecting reagents and growing NCs, thereby allowing them to control QD size precisely [16]. Although $CdMe_2$ is toxic, volatile, and a safety concern, it was a common precursor in QD synthesis till 2000. Later, Peng et al. and Talapian et al. demonstrated that the use of alkyl phosphonic acids or amines improves quality. Over time, researchers began replacing $CdMe_2$ with more stable Cd precursors, such as cadmium acetate ($CdAc_2$), cadmium carbonate ($CdCO_3$), cadmium oxide (CdO), and cadmium chloride ($CdCl_2$), enabling precise control over QD size, structure, and high PL quantum efficiencies (QYs) [17–19]. Similarly, Vossmeyer et al. developed an alternative synthesis route by replacing $CdMe_2$ with cadmium perchlorate ($Cd(ClO_4)_2.6H_2O$), demonstrating the first synthesis of colloidal CdS QDs in aqueous solution. This approach made water-based QD synthesis safer and more environmentally friendly [20]. CdX QD synthesis was further simplified by customizing chelating ligands to produce high-quality QDs with controlled size and optical properties, making these nanomaterials more accessible for research and industrial use.

In contrast to CdX QDs emitting visible light, lead chalcogenide (PbX, where X = S, Se, Te) QDs with a narrow bandgap emission in the NIR range (700–2000 nm) with an impressive PLQY (~ 70%) were prepared. Like CdX QDs, the emission color of PbX QDs can be tuned by altering their size *via* hot injection involving lead [$PbCl_2$, PbO, or $Pb(CH_3COO)_2$] and chalcogen precursors at high temperatures in non-coordinating solvents like octadecene or diphenyl ether [21–23]. Alivisatos's group focused on such colloidal synthesis and produced stable, size-uniform PbX QDs. Their efforts laid an essential foundation for synthesizing various Pb-based QDs [24].

Core-only QDs are unstable and degraded in the presence of moisture, oxygen, and UV light. Therefore, core/shell QDs were developed, in which the shells comprise higher-bandgap semiconductors, polymers, or silica. Semiconductor coating serves multiple purposes, improving the properties of the core by enhancing photochemical stability, increasing PLQY, mitigating surface defects, and suppressing non-radiative losses. As a result, various core-shell NCs have been engineered, such as CdSe/CdS, CdS/ZnSe, CdSe/ZnS, CdTe/CdSe, and CdTe/CdS. Additionally, core structures with multiple shell layers, such as CdSe/HgTe/CdTe, CdSe/CdTe/ZnSe, CdSe/CdS/$Zn_{0.5}Cd_{0.5}S$/ZnS, CdS/HgS/CdS, CdSe/ZnS/CdSe, CdSe/CdS/ZnS, and CdS/CdSe/CdS, have been developed, which show optimal optical properties and high PLQYs [24–26]. Similarly, the optical properties and physicochemical stability of PbX QDs were improved by preparing shells from PbS, ZnS, CdS, or CdSe.

The evolution of colloidal QDs has progressed from traditional II-VI and IV-VI systems toward high-performance, heavy-metal-free

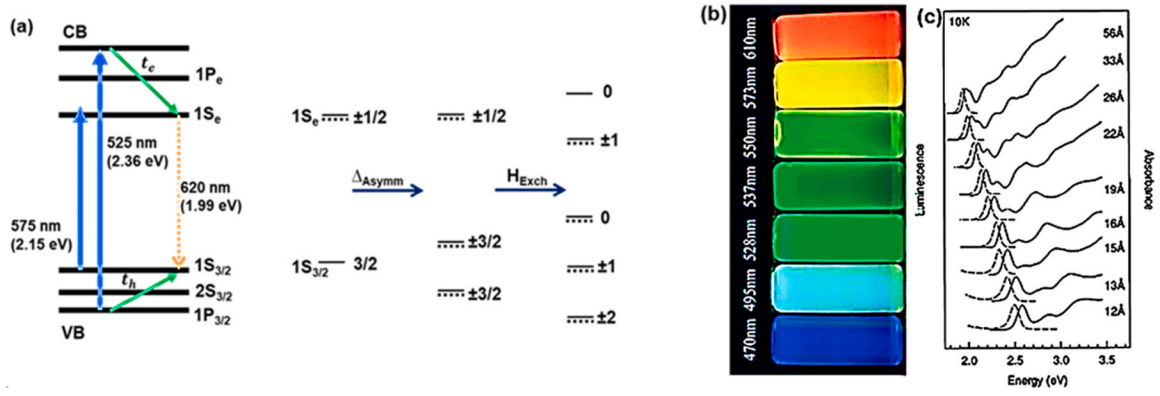

Fig. 1. (a) Electronic states and (b-c) optical properties of CdSe QDs. (a) Schematic presentation of band-edge states and nondegenerate electron and hole states, (b) photographs of CdSe QDs showing size-dependent PL, and (c) absorption and PL spectra of CdSe QDs. Reproduced with permission from (b) ref. 9; copyright 2008, the American Chemical Society, (c) ref. 10; copyright 1996, the American Physical Society.

alternatives. The structures and optical properties of classical and new-generation QDs are compared in Table 1. Historically, cadmium-based systems such as CdSe, CdS, and CdTe established the benchmark for near-unity (PLQY ~ 100%) and narrow emission linewidths, primarily through the development of "giant" or graded-alloy shells. However, recent advances demonstrate that sustainable III-V and I-III-VI QDs or NPs have effectively achieved comparable properties. For example, InP and $CuInS_2$ QDs exhibit low QY (<10%), and reach 80–100% efficiency upon coating with lattice-matched ZnSe/ZnS or GaS shells. This improvement is often accompanied by spectral shifts, particularly in narrow-gap systems (InAs, PbSe, and Ag_2Se), arising from carrier wavefunction delocalization and the relaxation of interfacial strain. The PL properties of selected QDs in the I-VI (Ag_2S, Ag_2Se, and Ag_2Te), III-V (GaN, GaP, GaAs, GaSb, InN, InP, InAs, and InSb), and I-III-VI ($CuInS_2$, $CuInSe_2$, $CuInTe_2$, $CuGaS_2$, $CuGaSe_2$, $AgGaS_2$, $AgGaSe_2$, $AgInS_2$, $AgInSe_2$, and $AgInTe_2$) groups are discussed in the preparation and properties sections of each.

Shelled (Core/shell) or multishell (core/shell/shell) QDs have demonstrated exciting optoelectronic properties, stability, and applications. However, their biological use is limited by hydrophobicity, which requires their conversion from the organic to the aqueous phase. Surface modification of QDs rendered them water-soluble for use in various biological applications [51–58], employing techniques such as ligand exchange and polymer/silica/phospholipid encapsulation [59]. In ligand exchange, hydrophobic groups on the QD surface were replaced with bifunctional ligands such as mercaptoacetic acid (MAA) [60,61], polyethylamine[62], mercaptosilanes[63], dihydrolipoic acid (DHLA) [64], cysteine65,66], polydentate thiols[67], poly(acrylic acid) [68], or peptides [69,70]. These ligands facilitate the dispersion of QDs in water and their biocompatibility. Alternatively, hydrophilic molecules were covalently attached to the QD surface, or QDs were encapsulated in amphiphilic block copolymers [71,72], polyethyleneglycol (PEG) [73–75], phospholipid micelles [76], or silica [63,77–82] to preserve their properties. Instead of ligand exchange, aqueous compatibility has also been achieved by direct synthesis of QDs in water by using various capping agents. For example, Gaopnik et al. developed water-soluble thiol-capped CdTe QDs by reacting cadmium thiolates with H_2Te gas under reflux at 100 °C for 3 days [67]. Subsequent modification of QDs with peptides [70] (Fig. 2a), streptavidin [83] (Fig. 2b), epidermal growth factor [84,85] (EGF, Fig. 2c,d), and several other moieties, including small molecules, antibodies, aptamers, DNA, and proteins, have demonstrated their potential for subcellular imaging [86–93]. Selected examples of *in vivo* imaging using subcutaneously or intravenously injected QDs are shown in Fig. 2e-i [65,71,75,86,87]. Also, specific *in vivo* applications of different QDs are shown in Table 2.

Table 1
Summary of PL properties of various QDs and NPs.

Core QD or NP	Emission wavelength (nm)	PLQY (Core)	PLQY (Core-shell)	Shell material	Refs.
CdSe	580–635	2–6%	98%	ZnS, CdS	[27, 28]
CdS	424–470	8%	~100%	ZnS, CdSe/CdS	[29, 30]
CdTe	700–800	15	97.2%	CdS/ZnS	[31, 32]
HgS	600–1000	0.1	19.8%	CdS	[33, 34]
HgSe	1700–2000	1.5%	63%	CdSe	[35]
HgTe	910–1200	< 42%	80–95%	CdS	[36, 37]
PbS	130–1600	20%	57%	CdS	[38]
PbSe	1470–1520	85%	70%	CdSe	[39]
Ag_2S	620–730	~20%	50%	ZnS	[40]
Ag_2Se	835–940	31%	42%	ZnSe	[41]
Ag_2Te	930–1085	10.7%	22.8%	SiO_2	[42]
InP	480–630	< 20%	> 90%	Zn(Se,S)/ ZnS	[43]
InAs	700–1200	8%	76%	InP/ZnSe	[44]
$CuInS_2$	500–950	3%	90%	ZnS	[45, 46]
$CuInSe_2$	700–1040	4%	40–50%	ZnS	[47]
$CuGaS_2$	471–846	< 15%	78–83%	ZnS	[48]
$AgInS_2$	540–720	< 20%	80%	ZnS	[49]
$AgInSe_2$	670–705	0.6%	5.6%	ZnSe	[50]

Although Cd- and Pb-based QDs have played a crucial role in shaping the landscape of electronic and optical properties of QDs in general, their biological applications, such as imaging, diagnosis, and therapy [65,66,71,75,86–89], are limited by the toxic heavy metal contents as well as by size, surface, and charge-based retention *in vivo*, and by the related pharmacokinetic complexities. Also, studies have shown cytotoxicity, ovarian dysfunction, oxidative stress, inflammation, and DNA damage induced by metal ions released by surface etching of QDs [72, 90–97] The impact of CdTe QDs on mitochondrial morphology and structure in HepG2 cells [98] revealed membrane potential disruption [99], increased calcium influx, and impaired cellular respiration due to the release of Cd^{2+}. These limitations were lifted by exploring alternative QDs free of toxic heavy metals. We focus on reviewing the synthesis, optical properties, and bioimaging applications of Cd-, Pb-, and Hg-free QDs, with emphasis on *in vivo* applications. The core (I-VI, III-V, and I-III-VI) QDs and their shells (Au, SiO_2, ZnS, ZnSe, InP/ZnSe, GaS_x, InS_x), surface functionalizing molecules, and selected bioconjugates of these QDs are shown in Fig. 3. Recently, I-VI, III-V, and I-III-VI QDs have received much attention in materials and physical sciences, as well as in biological applications, due to their lower toxicity compared to Cd-/Pb-/Hg-based QDs.

The biological safety of QDs is primarily governed by the intrinsic toxicity of the constituent metal ions and the stability of the nanocrystal against oxidative dissolution. Traditional II-VI and IV-VI materials, such as CdSe, PbS, and HgTe, exhibit high systemic toxicity due to the liberation of divalent cations (Cd^{2+}, Pb^{2+}, Hg^{2+}), which catalyze the formation of reactive oxygen species (ROS) and inhibit critical enzymatic functions *via* thiophilic binding. In contrast, silver-based chalcogenides (Ag_2S, Ag_2Se, Ag_2Te) and I-III-VI_2 multinary systems ($CuInS_2$, $AgInS_2$, $CuGaSe_2$) demonstrate significantly improved biocompatibility [100,101]. This is attributed to the lower toxicity of Ag^+ and Cu^+ ions compared to Cd^{2+}, Pb^{2+}, and Hg^{2+}, as well as the high lattice energy of these crystals, which resists ion leakage. However, III-V semiconductors present a distinct risk profile; while InP and GaN are relatively inert, arsenide and antimonide derivatives (GaAs, GaSb, InAs, InSb) are prone to rapid surface oxidation. This process releases toxic arsenic or antimony oxides, which induce mitochondrial stress and DNA fragmentation. Also, research indicates that toxicity is highly size-dependent; for example, InP QDs below 5 nm can undergo nuclear translocation, whereas larger, properly passivated QDs remain in the cytoplasm.

Pharmacokinetic behavior, including *in vivo* circulation half-life, biodistribution, and clearance pathways, is primarily determined by surface physicochemical properties rather than core composition. Bare cores composed of materials such as $CuInSe_2$, $AgGaSe_2$, and InTe are rapidly opsonized by serum proteins and subsequently sequestered by the reticuloendothelial system (RES), resulting in predominant accumulation within the liver and spleen. Adopting a core-shell architecture, for example $AgInS_2$/ZnS or InP/ZnSe/ZnS, is essential to establish a physical barrier against leaching and to provide a platform for further functionalization [100]. Surface charge plays a critical role: cationic particles, such as amine-functionalized $AgGaS_2$, demonstrate high cellular uptake *in vitro* but induce rapid plasma clearance and may cause pulmonary embolism *in vivo*. In contrast, zwitterionic or PEGylated coatings on Ag_2S and $CuInS_2$ promote prolonged circulation and enable renal clearance for particles with a hydrodynamic diameter below 10 nm. Recent studies indicate that Cd and Pb deposits persist in the renal cortex for several months, whereas appropriately encapsulated silver- and copper-based multinary QDs achieve nearly complete clearance within 30–60 days, provided the shell architecture effectively

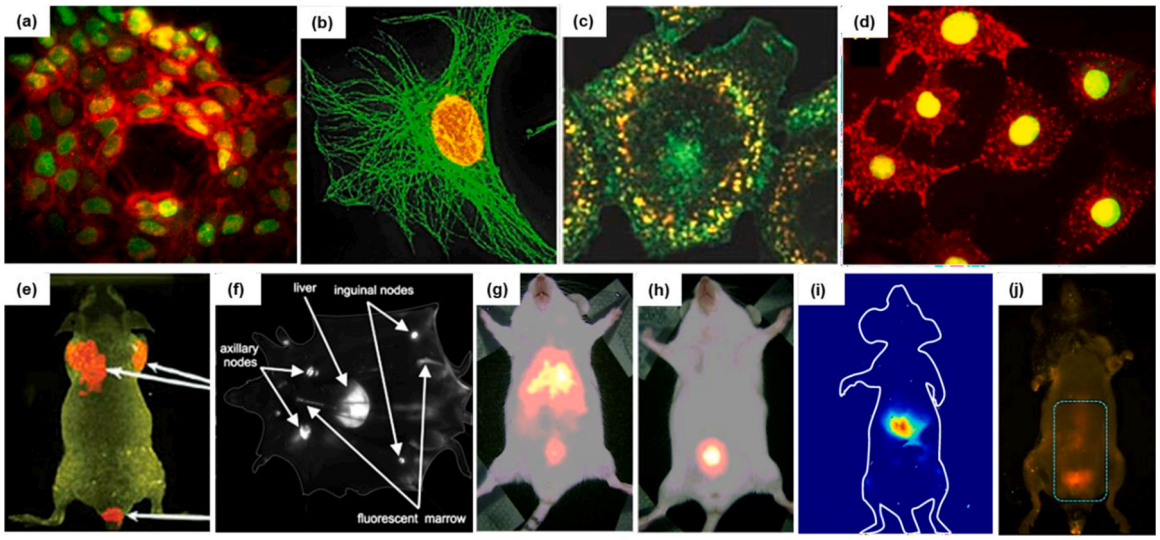

Fig. 2. (a-d) Fluorescent images of (a) H1650 cells stained with QD-AST, (b) QD-streptavidin, and (c, d) QD-EGF conjugates. (e, f) Fluorescent images of mice/rats intravenously injected with (e) QD-PSMA and (f) QD-PEG-COOH conjugates. (g, h) Radio images of CD-1 mice injected with the (g) Tc-QD574-Cys and (h) Tc-QD15-Cys conjugates. (i, j) Fluorescence images of B6 mice intravenously injected with (i) QD-EGF conjugates and (j) a photouncaging QD conjugate. Reproduced with permission from (a) ref. [70]; copyright 2009, the American Chemical Society, (b) ref. [83]; copyright 2003, Springer Nature; (c) ref. [84]; copyright 2004, Springer Nature, (d) ref. [85]; copyright 2013, Wiley-VCH, (e) ref. [71]; copyright 2004, Springer Nature, (f) ref. [75]; copyright 2007, the American Chemical Society, (g, h) ref. [65]; copyright 2007, Springer Nature, (i) ref. [86]; copyright 2015, The Royal Society of Chemistry and (j) ref. [87]; copyright 2013, the American Chemical Society.

Table 2
Selected Cd-based QDs, their bioconjugates, and *in vivo* applications.

QD	PL Wavelength (nm)	Conjugated molecule	Target/non-target(Clearance/Retention)	Animal model	Ref.
CdSe/ZnS	534, 554	DHLA, PEG, 99 m_{Tc}	Toxicity analysis, Renal excretion	Mice	[65]
CdSe (ZnCdS)	515	Cysteine, Alexa Fluor 555	Nonspecific (size-selective renal clearance)	Rat	[66]
CdSe/ZnS	700	TOPO, PSMA	Prostate cancer cells (Lessuptake in the liver and spleen)	Mice	[71]
CdS/ZnS	700	Carboxylate Pluronic F127 polymer, FA	Pan-1-tumor, acute toxicity	Mice	[72]
CdSe/CdTe/ ZnS	655	PEG 5k- COOH	Lymph node drainage (retention in lymph nodes)	Mice	[75]
CdSe/ZnS	705	EGF-AlexaFluor, Gd(III) complex	Multimodal imaging (Renal excretion)	Mice	[86]
CdSe/ZnS	705	PUNP	Nonspecific (renal clearanceafter the application)	Mouse	[87]
CdSe/ZnS	550620	GFE peptide,PEG	Lungs (95% clearance fromliver and spleen)	Mice	[88]
CdSe/ZnS	530	$^{99\ m}$Tc-EDTA-Cysteamine	Internal organs (slow clearance from the spleen)	Mice	[89]
CdSe/ZnS	655	Carboxylate functionalized	Ovary (accumulation andretention of QDs in the ovary)	Mice	[93]

prevents premature core dissolution. The toxicity and pharmacokinetics of selected QDs in the I-VI (Ag_2S, Ag_2Se, and Ag_2Te), III-V (GaN, GaP, GaAs, GaSb, InN, InP, InAs, and InSb), and I-III-VI ($CuInS_2$, $CuInSe_2$, $CuInTe_2$, $CuGaS_2$, $CuGaSe_2$, $AgGaS_2$, $AgGaSe_2$, $AgInS_2$, $AgInSe_2$, and $AgInTe_2$) groups are discussed in the biological application section of each.

Recent review articles have laid important groundwork for the development of colloidal semiconductor nanocrystals. For instance, Girma et al. summarized the synthesis and biomedical aspects of I–III–VI ternary quantum dots [100], offering valuable insights into specific materials. In parallel, recent reviews have covered the bioimaging and therapeutic aspects of silver chalcogenide QDs, especially in the first and, mainly, the second NIR biological window [101–104]. Building on these contributions, a comprehensive comparison of synthesis, PL properties, imaging, and therapeutic applications, or the challenges of classical heavy-metal-based QDs, remains highly valuable. In this review, we provide a thorough, comparative analysis that bridges traditional, high-performance yet toxic heavy-metal systems (Cd, Pb, Hg) and the next-generation biocompatible alternatives. The discussion is organized into three main families: I-VI (Ag_2S, Ag_2Se, Ag_2Te), III-V (GaN, GaP, GaAs, GaSb, InN, InP, InAs, and InSb), and a wide range of I-III-VI ($CuInS_2$, $CuInSe_2$, $CuInTe_2$, $CuGaS_2$, $CuGaSe_2$, $AgGaS_2$, $AgGaSe_2$, $AgInS_2$, $AgInSe_2$, and $AgInTe_2$) multinary QDs and NPs. By integrating recent advances in hypoxia tolerance, targeted multimodal bioimaging, and PDT theragnostic systems, this review outlines a roadmap for researchers and newcomers at the interface of materials synthesis, optical properties, and biological applications. It offers a critical look at the path toward safer, more versatile tools for precision healthcare.

2. Group I-VI QDs

2.1. Ag_2S QDs

Silver-based QDs were found to be attractive alternatives to the toxic metal chalcogenide QDs for bioimaging and image-guided therapy [105–110]. The potential of QDs for imaging and drug delivery has been significantly enhanced by the development of silver-based QDs (Ag_2S, Ag_2Se, Ag_2Te, $AgInS_2$, $AgInSe_2$, Table 3), which show low cytotoxicity and NIR excitation and emission windows. This biological window is crucial for *in vivo* imaging and phototherapy, where the NIR lasers have the advantage of evading the absorption window of biological fluids [111–117]. A field survey suggests silver-based QDs are superior to molecular or other NP fluorescence probes regarding NIR absorption, photostability, longer PL lifetimes, significant Stokes shifts, biocompatibility, and suitability for deep tissue imaging [118–123]. Table 3 summarizes the PL spectral position, bioconjugated molecules, and their *in vivo* applications of selected silver chalcogenide QDs.

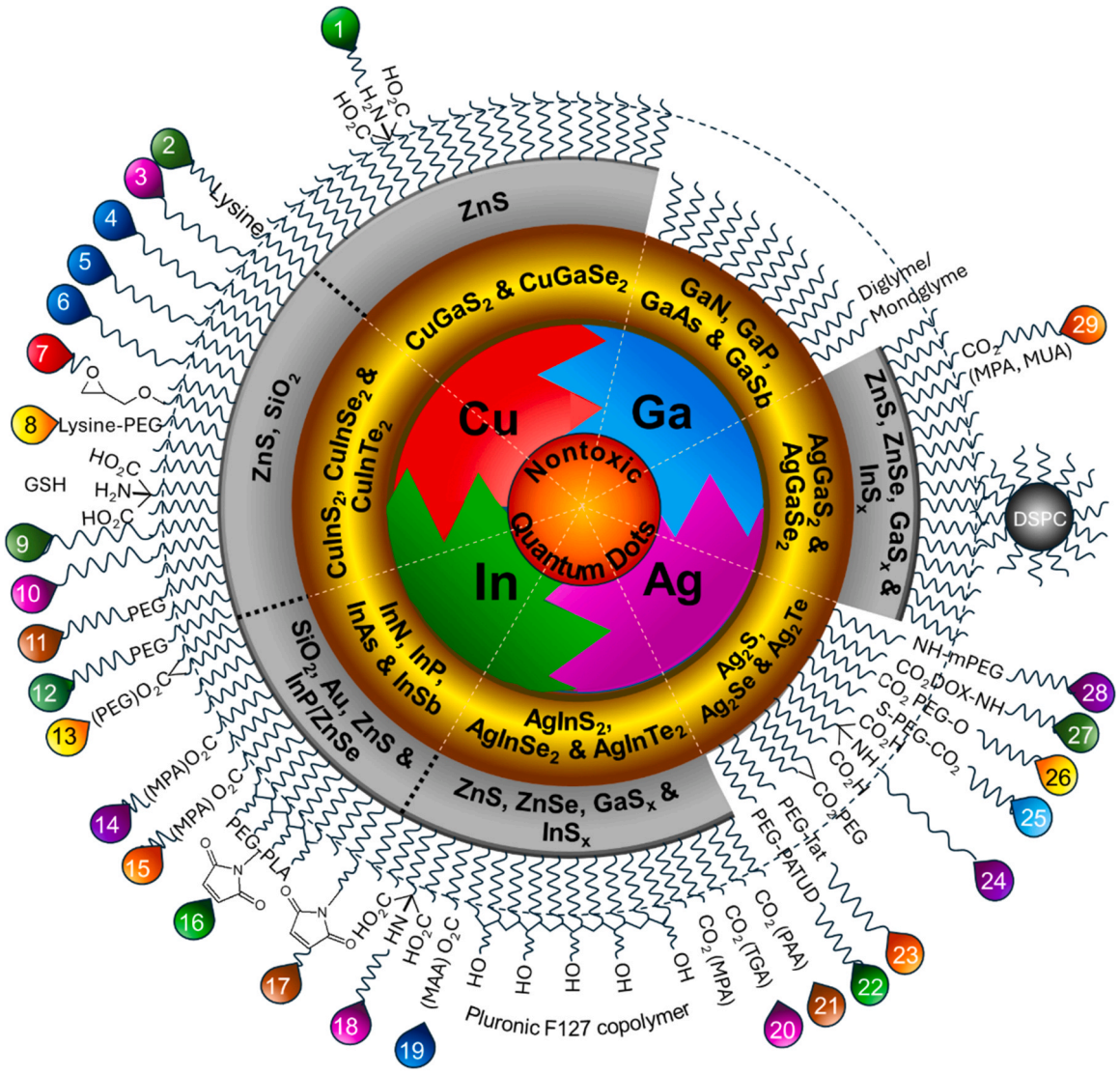

(1) PNPP-Alkaline phosphate
(2) Cystathione-γ-lyase-IgG-151
(3) PLGA-wild-invasin/911A(Ala) variant
(4) RNAse-A
(5) Chitosan
(6) PMAO-Jeffamine M1000/ED2003 or PMAO-Jeffamine M1000-BSA-At B1
(7) PLGA-wild-invasin/911A(Ala) variant
(8) LA-streptavidin
(9) GOPTS-transferrin
(10) Chitosan- FA
(11) Chitosan-RGD
(12) DSPE-PEG-2000-Anti-EpCAM ab
(13) MAA-PL-*b*-PEG-Anti-EGFR 7D12ab-Af
(14) MPA-VEGFR2 ab-miR-92a inhibitor
(15) MPA–HSA
(16) ME-anti-EFGR (7D12)-Af
(17) PEG-ME-cRGDfC
(18) GSH-PVP
(19) MAA-PAA-Baculoviral vector
(20) TGA- gelatin
(21) Octylamine-PAA-RGD
(22) PEG_{1000}-PTUD
(23) 6PEG-Tat peptide-hMSC
(24) Mn^{2+}-MV
(25) ABS
(26) [C18-PMH] –PEG
(27) Fmoc-His/Er3+-MPA-DOX-A1094
(28) DSPE– mPEG- Cy GSH
(29) signal PSA ab

Fig. 3. A scheme of I-VI, III-V, and I-III-VI QDs, their shells, and surface conjugated molecules, including selected biomolecules for *in vivo* applications: PNPP (p-nitrophenylphosphate), PLGA [poly(lactic-co-glycolic) acid], PMAO [poly(maleic anhydride-alt-1-octadecane)], At (aflatoxin), LA (lipoic acid), GOPTS (3-Glycidyloxypropyl trimethoxy silane), FA (folic acid), RGD [arginine (Arg)-glycine (Gly)-aspartic acid (Asp)], DSPE (1,2-distearoyl-sn-glycero-3-phosphorylethanolamine), PEG, EpCAM (epithelial cell adhesion molecule), ab (antibody), MAA (mercaptoacetic acid), PL (polylactide), EGFR (epidermal growth factor receptor), Af (amioflavone), MPA (mercaptopropionic acid), VEGFR (vascular endothelial growth factor receptor), HSA (human serum albumin), ME (maleimide ester), cRGDfC [cyclo(RGD-D-phenylalanine (phe)-cysteine (cys)], GSH (glutathione), PVP [Poly(vinyl pyrrolidone)], PAA (polyacrylic acid), TGA (thioglycolic acid), PTUD (polythiourea dendrimer), Tat (trans-activator of transcription), hMSC (human mesenchymal stem cells), MV (microvesicles), ABS [4-(2-Aminoethyl)benzenesulfonamide], C18-PMH [poly (maleic anhydride-*alt*-1-octadecene)], Fmoc (9-fluorenylmethyloxycarbonyl), DOX (doxorubicin), A1094 (a NIR absorbing croconaine dye), MUA (mercaptoundecanoic acid), and PSA (prostate specific antigen).

2.1.1. Synthesis and optical properties

Ag_2S NCs were first synthesized by Motte et al. through the reverse micelle method, in which water droplets acted as templates to control the NP size and polydispersity, yielding QDs in the 2–10 nm range [106]. Expanding on this, Brelle et al. reported an alternate method for direct synthesis of cysteine- or glutathione (GSH)-capped Ag_2S QDs with an average size of 9 nm. They investigated the ultrafast dynamics of photogenerated electrons in Ag_2S NPs as a function of capping agent composition, attributed to the carrier dynamics to variations in the absorption cross-sections of deep trap states [105]. Subsequently, Du et al. reported the first NIR-emitting Ag_2S QDs (10.2 nm) with an emission peak at 1058 nm, synthesized by pyrolysis of a single-source precursor of silver $[(C_2H_5)_2NCS_2Ag]$, in a mixture of oleic acid (OA), octadecene, and octadecylamine at 200 ℃ [107]. The NIR emission characteristics of

Table 3
Selected Ag_2X (X = S/Se/Te) QDs, their bioconjugates, and *in vivo* applications.

QD	PL Wavelength (nm)	Conjugated molecule	Target/non-target (Clearance/ Retention)	Animal model	Ref.
Ag_2S	1200	DHLA, PEG	4T1 tumor (fast clearance from organs)	Mice	[111]
Ag_2S	1200	cRGDfk	$\alpha_v\beta_3$ integrin receptor in tumor cells (rapid clearance)	Mice	[113]
Ag_2S	1135	PEG, ABS amide	Carbonic anhydrase in the tumor (less-toxic, no accumulation)	Mice	[120]
Ag_2S	~1250	Tat peptide	HMSCs tracking and labeling (minute toxicity)	Mice	[123]
Ag_2S	930	Cetuximab	Orthotopic tongue cancer (Slow clearance, less toxicity)	Mice	[124]
Ag_2S	820	DOX-L particles	Tumor targeting, less-toxic	Mice	[125]
Ag_2S	1550	PEG. Rare earth metals, BINAP	CD44 trans membrane protein on the tumor surface (less-toxic)	Mice	[126]
Ag_2Te	1130	BSA	GI tract (rapid clearance)	Mice	[127]
Ag_2Te	1300	Poly (lactic-co-glycolic acid)	4T1 tumor, less accumulation in the liver and spleen	Mice	[128]

Ag_2S QDs (Fig. 4) highlight their potential for bioimaging and warrant further research into their biocompatibility and colloidal stability. Surface functionalization with hydrophilic ligands, including PEG, GSH, and cysteine, has been widely employed to enhance aqueous solubility and biocompatibility. For example, PEGylated Ag_2S QDs synthesized by Wang's group exhibited NIR-II fluorescence (1000–1500 nm, Fig. 4a), demonstrating high colloidal stability across various buffer solutions and enabling *in vivo* visualization of lymphatic drainage and deep vascular networks with high spatial and temporal resolution [108]. Furthermore, they modified the synthesis procedure by exchanging dodecanethiol (DT) with DHLA to make a hydrophilic surface on Ag_2S QDs. Fig. 4b shows that DHLA-conjugated Ag_2S QDs exhibit red-shifted PL with an increase in the FWHM compared to DT- capped Ag_2S QDs. These QDs were subsequently conjugated with DHLA-PEG to enhance stability and biocompatibility [109]. Similarly, Yang et al. developed a biocompatible synthesis of Ag_2S QDs by modifying reaction conditions to facilitate the *in situ* incorporation of GSH as a surface ligand, resulting in well-dispersed NCs with reduced aggregation. Fig. 4c illustrates the tunable PL of Ag_2S NCs, where a decrease in GSH density leads to an increase in Ag_2S NP size and shifts the PL band from the visible (624 nm) to the NIR (724 nm) region. The photographs in Fig. 4c show the QD solution under daylight and UV (365 nm) irradiation [110]. Methods such as core-shell preparation, including coating Ag_2S QDs with ZnS, silica, or polymers such as polyvinyl alcohol (PVA) and polyacrylic acid (PAA), have been widely employed to enhance their stability in aqueous phase. In several colloidal methods, the as-synthesized QDs were capped with hydrophobic ligands, making the particles incompatible with aqueous media. Reports about surface ligand exchange or surface modification of Cd/Pb chalcogenides helped establish efficient ligand exchange methods for Ag_2S QDs using MPA, sodium dodecyl sulfate (SDS), or cetyltrimethylammonium bromide (CTAB), proving increasingly biocompatible QDs [111–123,129–138]. By making Ag_2S QDs water soluble, stable, biocompatible, and NIR emitting, a new class of luminescent NPs has been introduced for real-time *in vivo* imaging of various biological structures and processes.

2.1.2. Biological applications

Surface-functionalized Ag_2S QDs have been explored for *in vivo* imaging by intravenous, intramuscular, or subcutaneous injection. Dai et al. demonstrated the *in vivo* imaging potential of Ag_2S QDs coated with DHLA and 6PEG by intravenously injecting 6PEG-functionalized Ag_2S QDs into a female BALB/c mouse bearing a 4T1 tumor xenograft on the right limb. Fig. 4d demonstrates time-lapse fluorescence images showing QD circulation to the heart and lungs, and movement to the excretory system. Moreover, a gradual increase in QD accumulation was observed, predominantly at the tumor site, which becomes prominent within 2 min post-injection. From 30 min to 24 h, they observed a predominant increase in fluorescence intensity in the tumor region, with a decrease in other organs, indicating preferential tumor localization [111]. Targeted delivery has also been achieved using QD conjugated to RGD peptides, which bind to integrin αvβ3 receptors overexpressed in cancer cells. [112]. For example, Tang et al. conjugated the cyclic cRGDfk peptide to Ag_2S QDs and intravenously injected them into mice bearing the 4T1luc tumors. These QDs specifically bind to the tumor within 1 h and are cleared by renal excretion within 24 h, highlighting their potential for targeted imaging applications [113]. Similarly, Ag_2S QDs conjugated with RGD and amphiphilic peptides have been employed in animal models to locate tumor cells and track during surgical resection [114]. Gd-doped Ag_2S QDs enable dual NIR-II and magnetic resonance imaging (MRI) and precise detection of brain tumor margins for image-guided surgery, while a FRET-based system incorporating VCAM1-targetted Ag_2S QDs with an NIR absorber (A1094) enables rapid brain injury detection, underscoring their clinical potential [115].

Ag_2S QDs conjugated with poly[di(carboxylatophenoxy)phosphazene and PEG have demonstrated biocompatibility, tumor growth suppression, and biodegradation [116]. In addition, one-step QD synthesis using PEGylated polyacylthiourea dendrimer yields stable water-soluble QDs, for selective tracing of A549 cancer cells and *in vivo* imaging of vascular systems [117]. Similarly, Ag_2S QDs modified with dibenzocyclooctyne (DBCO) amine maintain stable NIR fluorescence in acidic gastric environment, enabling imaging of gastric bacterial imbalance, stomach inflammatory responses, and injuries [118]. A recent report demonstrated Ag_2S vesicles carrying a pH-responsive copolymer, thiolate polystyrene-co-poly(4-vinylpyridine), and hydrophilic PEG-SH enable dual-function *in vivo* imaging and photothermal therapy [119]. Also, Ag_2S-PEG-ABS conjugate, prepared by ligand exchange and amide condensation, is an effective *in vivo* diagnostic and therapeutic agent. This conjugate and pristine Ag_2S were injected into colon tumor-bearing mice via the tail vein. The Ag_2S-PEG-ABS conjugate was selectively localized in the tumor within 24 h post-injection, enabling accurate, high-contrast tumor imaging in the NIR-II window. Fig. 4e compares *in vivo* imaging and biodistribution at different time points with Ag_2S and Ag_2S-PEG-ABS QDs [120].

Silver QDs conjugated with targeting/drug ligands facilitate tracking drug translocation pathways in animal models, ensuring treatment efficiency. Ag_2S QD-Tat-labeled human mesenchymal stem cells (hMSCs) allow detection of as few as 1000 cells *in vivo*, exhibiting a linear correlation between cell number and NIR fluorescence intensity (R^2 = 0.99), and support real-time monitoring of transplanted cell dynamics in regenerative applications [122,123]. Similarly, Ag_2S QDs have been applied to diagnose and treat peritoneal metastases. For example, Ling et al. showed that Ag_2S QD-based nanotheranostic system incorporating doxorubicin remains inactive in healthy cells, while showing brilliant NIR fluorescence with the inhibition of tumor growth in tumor nodules [129]. Surface chemistry-dependent *in vivo* dynamics has also been investigated, with PEG-coated Ag_2S QDs showing the fastest biodistribution [130]. Temperature-dependent fluorescence decay studies

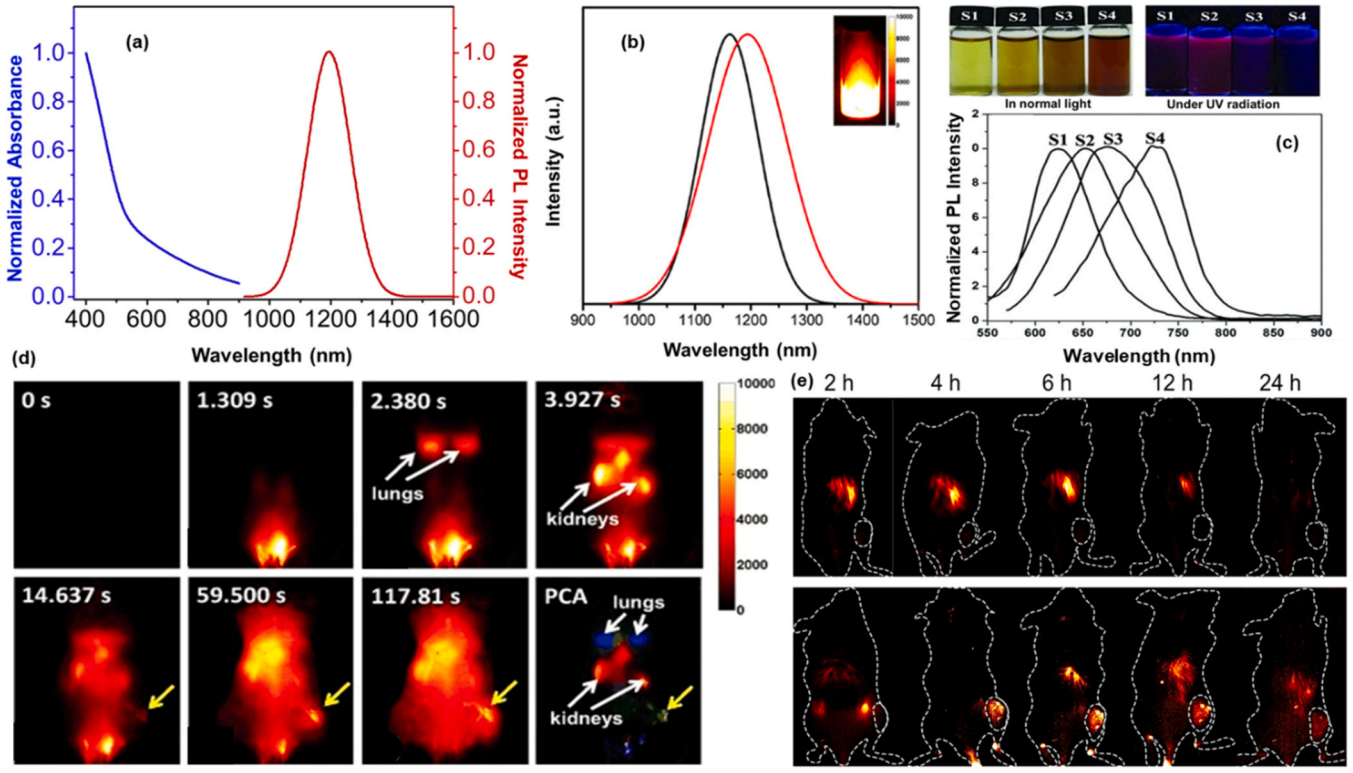

Fig. 4. (a) Absorbance and PL spectra of PEGylated Ag_2S QDs, (b) size-dependent PL spectra of Ag_2S QDs, (c) PL images and spectra of Ag_2S NCs with visible red (624) to NIR (724) emissions, (d) time-dependent *in vivo* NIR-II fluorescence images of 4T1 tumor-bearing mouse injected with PEG-Ag_2S QDs, and (e) comparison of *in vivo* fluorescence images and biodistribution of Ag_2S and Ag_2S-PEG-ABS QDs at different time points. Reproduced with permission from (a) ref. [108]; copyright 2014 Elsevier Ltd., (b) ref. [109]; copyright 2012, the American Chemical Society, (c) ref. [110]; copyright 2012, Wiley-VCH, (d) ref. [111]; copyright 2012, Wiley-VCH, and (e) ref. [120]; copyright 2024, Elsevier Ltd.

underscore the potential application of Ag_2S in luminescence nanothermometry. Femtosecond laser excitation enhances PLQY and deep *in vivo* imaging contrast [132]. Their photothermal emission enables real-time monitoring of Bestatin release from polypeptide hydrogel in animal models [133].

Recently, silver-based QDs have been explored for detecting and treating diseases caused by microbial pathogens. Ag_2S nanoclusters have significantly suppressed the viral titers of the model coronavirus and porcine epidemic diarrhea virus (PEDV) by inhibiting the synthesis of viral negative-strand RNA and viral budding [134]. Ag_2S QDs conjugated with a biomimetic silver binding peptide (AgBP2) exhibited antibacterial activity against *Escherichia coli* in liquid media through synergistic photothermal effect and reactive oxygen species (ROS) [135]. The warm temperature (46 °C) and ROS generated during photoexcitation of AgBP2- Ag_2S QDs induced cell wall breakage and bacterial cell death. Similarly, an Ag_2S QD-based wound-dressing hydrogel with $mSiO_2$ effectively cured infections caused by methicillin-resistant *S. aureus* through a synergistic photothermal effect and ROS-mediated toxicity [136]. In addition, surface-engineered Ag_2S QDs have been developed for the sensitive detection of *S. aureus*[137] and for *in vivo* imaging of inflammation in animal models [138].

2.2. Ag_2Se QDs

2.2.1. Synthesis and optical properties

As with CdSe QDs, Ag_2Se NPs have been synthesized using various methods. The Xie group reported the first room-temperature synthesis of Ag_2Se QDs in 1998, using a reaction of silver nitrate ($AgNO_3$), Se, and potassium borohydride (KBH_4) in pyridine. They obtained QDs with an average size of 20–30 nm [139]. Subsequently, Glanville et al. demonstrated Ag_2Se nanowires using silver-coated porous alumina as the templates, followed by selenium electrodeposition[140]. Cationic exchange has also emerged as a powerful synthetic method for Ag_2Se NPs. Son et al. demonstrated the transformation of CdSe QDs into Ag_2Se QDs by treating CdSe QDs dispersed in toluene with $AgNO_3$ in methanol, where Ag ions replace Cd ions. Notably, the size of the resulting Ag_2Se QDs depends on the size of the parent CdSe QDs [141]. In addition, Wang et al. demonstrated an economical and facile synthesis of Ag_2Se NPs via the reaction of Ag NPs with Se powder. To octadecylamine (ODA) heated at 180℃, $AgNO_3$ was added, and the mixture was stirred for 10 min to form Ag NPs. The reaction was stopped by adding Se powder. This weakens the Ag-N bond due to the strong interaction between Ag and Se [142]. An aqueous-phase strategy was introduced by Gu et al., where SeO^{2-} is reduced using GSH, and an Ag^{+}-alanine complex served as the silver precursor. Injection of freshly prepared Se precursors into the Ag precursors at 90 ℃ yielded monodispersed Ag_2Se QDs with a 3 nm diameter [143]. Surface passivation plays a crucial role in enhancing the properties of Ag_2Se QDs, including emission, colloidal stability, photostability, and biocompatibility. For example, Dong et al. synthesized water-soluble Ag_2Se QDs by the solvothermal method, resulting in brilliant NIR fluorescence (ca.1300 nm, Fig. 5a,b), by capping with C18 PMH-PEG [144]. The tunability of PL emission in the NIR region (1080–1330 nm, Fig. 5c) was demonstrated by the Pans group by varying the reaction time with suitable ligands, where 1-octanethiol enables efficient control over nucleation and growth [145]. These advances in surface engineering and controlled synthesis have led to the development of aqueous-phase, size-tunable, and brilliant NIR fluorescent Ag_2Se QDs [41], thereby significantly accelerating *in vivo* imaging applications.

2.2.2. Biological applications

Building on advances in surface engineering, Ag_2Se QDs have been

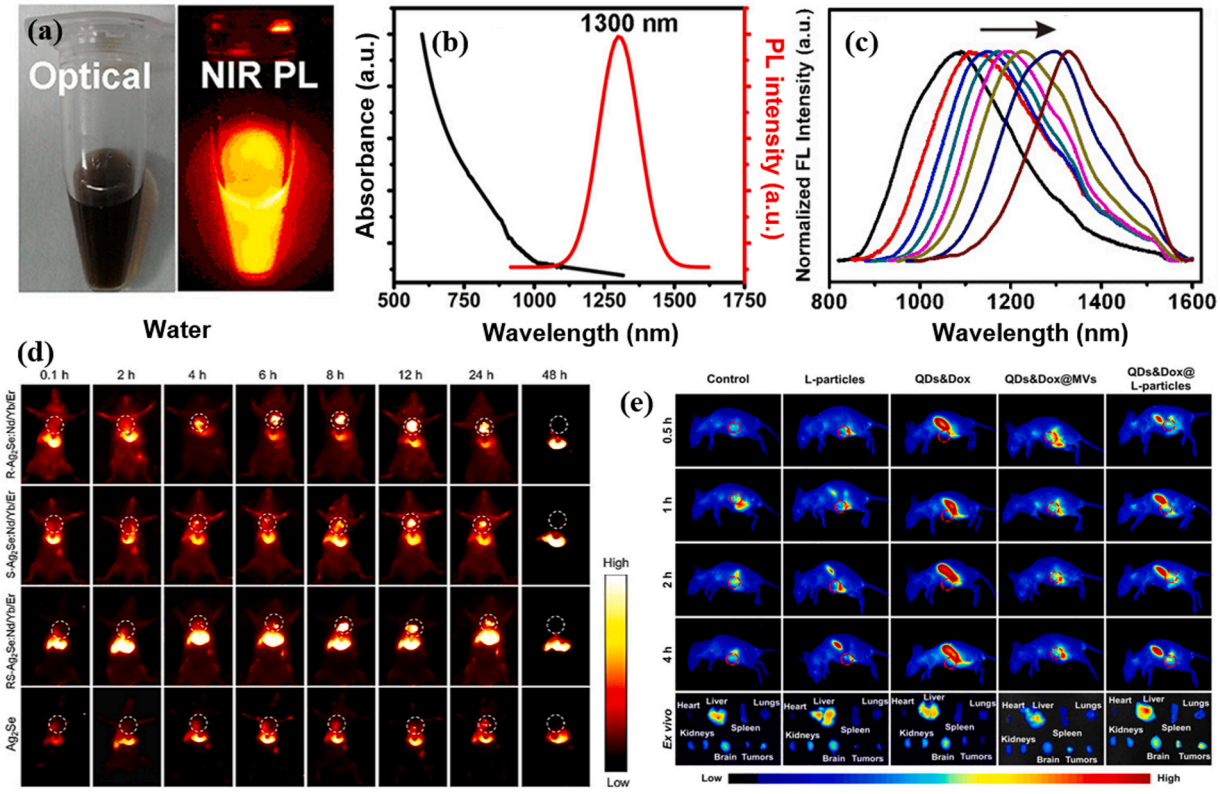

Fig. 5. (a) Bright-field and NIR PL images and (b) absorbance and PL spectra of C18 PMH-PEG Ag_2Se QDs in water. (c) PL tunability of Ag_2Se QDs by controlling the reaction time. (d) NIR PL images of mice injected with Ag_2Se:Nd/Yd/Er NPs. (e) Time-lapse PL images of a tumor-bearing mouse after intravenous injection of QDs loaded with nanovectors. Reproduced with permission from (a, b) ref. [144]; copyright 2013, the American Chemical Society, (c) ref. [145]; copyright 2013, the American Chemical Society, (d) ref. [126]; copyright 2022, Wiley-VCH, and (e) ref. [125]; copyright 2019, the American Chemical Society.

further functionalized to achieve tunable emission and enhanced biocompatibility, making them highly applicable for various biological applications, such as targeted drug delivery, cell imaging, and *in vivo* imaging. For example, Zhu et al. demonstrated low-toxicity, highly fluorescent Ag_2Se QDs conjugated with cetuximab, an EGFR-targeting antibody. These Ag_2Se-cetuximab nanoprobes demonstrated effective tumor targeting, imaging, and therapeutic efficacy in nude mice bearing tongue cancer, highlighting their potential as a multifunctional platform for cancer theranostics [124]. Some other *in vivo* applications of Ag_2Se QDs are discussed below. Yu et al. introduced 1.8 nm Ag_2Se-Mn QDs into circulating microvesicles, enabling targeted *in vivo* imaging and cancer therapy [146]. Pangs group further introduced a strategy that allows real-time imaging, drug delivery, and tumor targeting by transforming non-infectious colitic viral light (L-) particles into tumor-targeting nanovectors. This was achieved by labeling viral particles with NIR Ag_2Se QDs and loading antitumor drugs. Fig. 5e shows *in vivo* imaging of xenograft tumor-bearing nude mice intravenously injected with PBS (control), L-particles, QDs, and Dox, to evaluate therapeutic potential at different time points post-injection. The red circle in the figure represents the tumor location [125]. The suitability of Ag_2Se QDs for deep tissue imaging was further demonstrated using alanine-stabilized QDs in the abdominal cavity of nude mice [143]. In this report, robust fluorescence was detected from depths of at least 1 cm below the tissue. Such deep penetration ability of these QDs underscores the potential for noninvasive imaging applications. In addition, targeting the metabolism of cancer cells has been explored using Ag_2Se QDs functionalized with glucosamine *via* EDC/NHS coupling, enabling the probing of glucose uptake by tumor cells [147]. Similarly, Ding et al. developed rare-earth metal-doped Ag_2Se for deep imaging of tumor tissue. They developed different types of NPs using Nd, Yb, or Er. It showed a strong affinity for the CD44 receptor overexpressed on tumor surfaces, enabling *in vivo* analysis of tumor cells. The corresponding *in vivo* fluorescence images of tumor-bearing mice injected with these NPs are shown in Fig. 5d [126]. Recently, Yang et al. demonstrated precisely tunable emission from Ag_2Se QDs (600-1100 nm) by optimizing Se precursors. Due to their excellent stability, the QDs were found to be effective for gastrointestinal (GI) labeling [148]. The studies collectively highlight the potential of surface-engineered and tunable Ag_2Se QDs for high-resolution, deep-tissue, and targeted bioimaging applications.

2.3. Ag_2Te QDs

2.3.1. Synthesis and optical properties

Ag_2Te shows exciting bulk properties, including thermoelectric, magnetic, mechanical, and chemical properties [149–151]. However, when reduced to QD size, the strong quantum confinement leads to substantial modifications in their optical properties, making them attractive for optoelectronics and biomedical imaging. In most instances, Ag_2Te QDs were prepared using methods similar to those for Ag_2S and Ag_2Se, such as colloidal synthesis, cation exchange, or hot injection [127,128,152–156]. Although Ag_2Te QDs are less explored than other metal chalcogenides, there has been growing interest in their synthesis, tunability, and *in vivo* applications [42,152–154]. For example, Sahu et al. demonstrated a one-pot, low-temperature synthesis of Ag_2X (X = S, Se, Te) QDs by the injection of Ag-TOP solution into the telluride precursor, followed by rapid quenching of growth by cooling in an ice bath. The NCs were precipitated from ethanol and redispersed in hexane [152]. Pang and coworkers have further expanded the scope of Ag_2Te QDs by demonstrating their use in NIR imaging. They reported the synthesis of Ag_2Te QDs with an emission at 1300 nm. To perform *in vivo* studies, they assembled the QDs with poly (lactic-co-glycolic acid) [PLGA] using an emulsion solvent evaporation method, resulting in

improved dispersibility and stability. *In vivo* studies demonstrated high-resolution tumor imaging, and functionalizing these QDs with cell membranes derived from 4T1 cells enabled long-term, biocompatible tumor imaging with enhanced tissue penetration [128]. To address the challenge of improving the PL quantum yield of Ag_2Te QDs, Song et al. introduced NIR dyes (IR 780) as antennae that anchor on the QD surface. The QDs were synthesized using hot injection and capped with DT to maintain their stability and solubility in organic solvents, resulting in a 21-fold enhancement in the PLQY. Fig. 6a shows the absorption and PL spectra of these QDs. Furthermore, a heptamethine cyanine (an NIR-II fluorescent dye) with a GSH recognition unit was incorporated into the QDs to develop a nanoprobe for high-contrast *in vivo* imaging [153]. Controlling the reactivity of Ag precursors was another method used by Pang's group to obtain good-quality Ag_2Te QDs with high PLQY. They regulated it by varying the concentrations of Te precursors and silver(I) complexes. By controlling the growth of trialkylphosphine-Te precursors, they studied the nucleation and growth of the reaction. This helped tune the size of Ag_2Te QDs, yielding tunable emission in the 950–2100 nm range (Fig. 6b) [154]. Similarly, Shi et al. prepared high-quality, water-soluble Ag_2Te QDs *via* hot injection using an optimized TBP-Te precursor. This approach enabled efficient phase-transfer using thiol ligand exchange, resulting in QDs with exceptionally high PLQYs. These water-soluble QDs were then successfully employed for *in vivo* imaging of lymph nodes, abdominal vessels, and tumor vessels, demonstrating good biocompatibility and imaging capabilities [155]. Overall, the development of Ag_2Te QDs with tunable size-dependent NIR PL emission and excellent photostability highlights their versatility for various biological applications.

2.3.2. Biological applications

Ag_2Te QDs, which are biocompatible and free of heavy metals, are used for various biomedical applications, such as *in vivo* imaging and therapeutic monitoring [127,153–160]. However, compared to the above Ag-based QDs, Ag_2Te QDs have been less explored in biological applications. Some studies highlighting their use in biological applications are mentioned below. For example, Li et al. reported an aqueous-phase, one-pot synthesis of Ag_2Te QDs using bovine serum albumin (BSA) as a templating and stabilizing agent, which produced uniformly sized BSA-Ag_2Te QDs with excellent efficiency in CT/NIR-II GI imaging. As shown in Fig. 6c-g, NIR-II fluorescence imaging enabled clear visualization of intestinal obstructions before surgery, along with detailed *ex vivo* imaging after surgery, demonstrating significant potential for the diagnosis of gastrointestinal diseases [127]. Wang's group developed a nanoadaptor using hyaluronic acid (HA) and dibenzocyclooctyne-functionalized gold-silver (Au: Ag_2Te) QDs that target cancer cells *via* a click reaction. This innovative approach enables precise, specific *in vivo* tumor cell targeting and imaging, with new perspectives for the diagnosis and treatment of cancer [156]. Recent

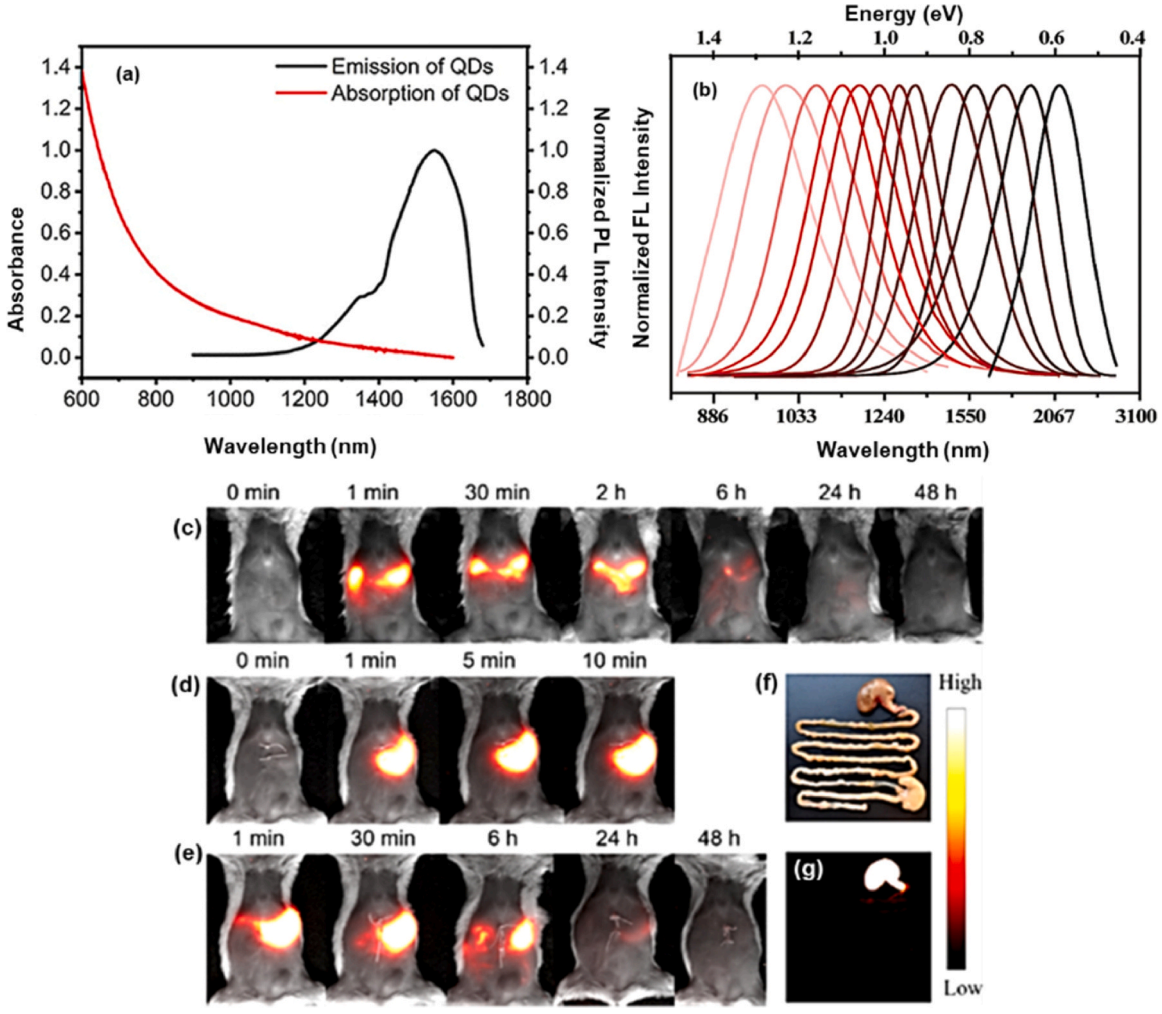

Fig. 6. (a) Absorption and PL spectra of Ag_2Te QDs under 808 nm laser irradiation, (b) PL spectra with different emission maxima, (c-f) NIR-II fluorescence images of the GI tract, (c) different times after the oral ingestion of BSA-Ag_2Te QDs, intestinal obstruction (d) before, (e) after surgery, and (f,g) ex vivo image of the GI tract [Digital (above) and NIR-II fluorescence (below)]. Reproduced with permission from (a) ref. [153]. Copyright 2021, American Chemical Society, (b) ref. [154]. Copyright 2021, American Chemical Society, and (c-g) ref. [127]. Copyright 2023, American Chemical Society.

studies also explored the photothermal properties of silver-based QDs and their application as cancer theragnostic agents. The cancer-specific RGD peptide-conjugated Ag_2S, Ag_2Se, and Ag_2Te QDs were effectively used to label and kill cancer cells [129] selectively.

Intravenous injection of silver chalcogenide QDs in murine models revealed time-dependent clearance and distinct biodistribution. Biodistribution analysis of PEGylated Ag_2S, Ag_2Se, and Ag_2Te QDs shows distinct accumulation in specific organs with fluorescence retention. PEGylated Ag_2S QDs predominantly accumulated in the liver and spleen compared to other organs, indicating slow renal clearance. In contrast, PEGylated Ag_2Se QDs initially distribute across the blood, liver, and lungs, followed by a gradual decrease in organ accumulation due to hepatic degradation. Likewise, PEGylated Ag_2Te QDs showed bright NIR fluorescence, with negligible fluorescence in major organs due to the short blood circulation lifetime of the QDs. These QDs initially accumulate in the liver and spleen (Fig. 7), followed by subsequent clearance [158–160]. Further studies demonstrate that surface functionalization of silver chalcogenide QDs with small molecules, such as biotin, amino acids, carboxylic acids, and PEG, improves their stability during *in vivo* circulation and target specificity.

3. Group III-V QDs

Group III-V quantum dots (GaN, GaP, GaAs, GaSb, InN, InP, InAs, and InSb) are an important class of semiconductor nanomaterials, owing to their high absorption coefficients, direct bandgap, and excellent stability. They are also valued for their tunable NIR emission and high quantum yields, making them suitable for various biological applications. Synthesis, optical properties, and biological applications of each QD are discussed below. Typical III-V, their PL wavelengths, bioconjugated molecules, and *in vivo* applications are listed in Table 4.

3.1. InN QDs

3.1.1. Synthesis and optical properties

Indium-based binary QDs are III-V semiconductor NCs, typically with a zinc-blend or wurtzite crystal structure and sp^3-like hybridization. Indium Nitride (InN) QDs are highly stable in air with a narrow band gap of 0.7 eV. Like other group III-V QDs, InN QDs were initially synthesized using conventional top-down techniques such as plasma-assisted beam epitaxy (PA-MBE), metal-organic vapor phase epitaxy, and metal-organic chemical vapor deposition [174]. Solution-based synthesis has also been developed for size control and scalability. For example, Chen et al. developed a hybrid solution-vapor-phase method in which indium oxide NCs were coated with silica and annealed (500–700 °C, 5 h) under ammonia vapor to yield ~5.7 nm InN QDs [175]. Later, Qaeed et al. demonstrated a low-temperature wet-chemical synthesis of wurtzite-like InN QDs. The reaction was carried out by heating indium acetylacetonate and oleylamine (OAm) at 90 °C, followed by the addition of nitric acid to form indium nitrite. The subsequent introduction of ammonium hydroxide generated indium hydroxide and ammonia gas, and prolonged heating (4, 8, and 12 h) enabled gradual substitution of oxygen by nitrogen, resulting in the formation of InN QDs. Similarly, Beaulac's group synthesized InN QDs using the hot injection method, using alkylamide as the reducing agent to form In (0), followed by nucleophilic substitution to form an indium-nitrogen bond [176]. Nagakubo et al. reported the synthesis of gallium indium nitride (GaInN) and zinc indium nitride (ZnInN) by reacting sodium amide with indium iodide or gallium iodide in phenyl ether. They used OAm, TOPO, OA, and octadecanethiol as the stabilizing ligands to achieve high crystallinity, controlled particle size (2–6 nm), and long-term colloidal stability [177]. Recently, Mulvaney's group synthesized size-tunable InN QDs by hot injection, using trimethylindium as the indium source and sodium amide as a nitrogen precursor. The indium precursor was injected into the nitrogen precursor in hexadecane and OAm at 120–180 °C. The resulting QD exhibited tunable PL emission (525–680 nm) by varying reaction time and temperature [178]. Despite these advancements in synthesis, the biological applications of InN QDs remain largely unexplored.

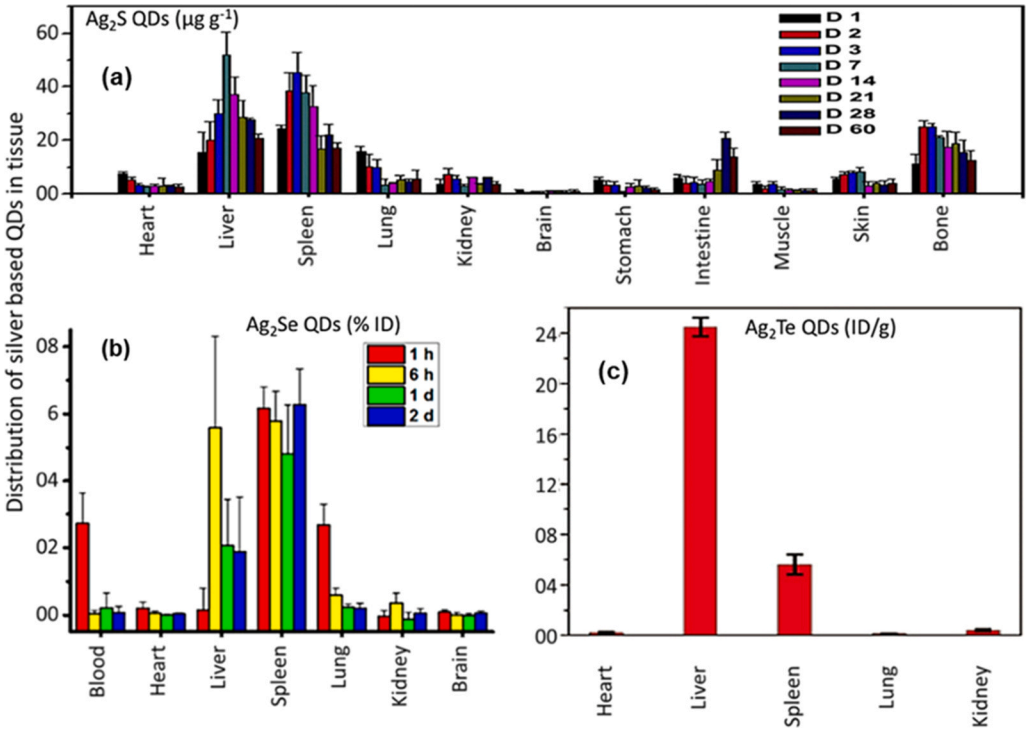

Fig. 7. Distribution of intraperitoneally injected Ag_2S, Ag_2Se, and Ag_2Te QDs in different organs of experimental mice. Reproduced with permission from (a) ref. [160]. ref. Copyright 2013, Elsevier Ltd., (b) ref. [159]. Copyright 2016, American Chemical Society, and (c) ref. [158]. Copyright 2021, American Chemical Society.

Table 4
Selected heavy metal-free group III-V, group I-III-VI QDs, their bioconjugates, and *in vivo* applications.

QD	PL Wavelength (nm)	Conjugated molecule	Target/non-target(Clearance/Retention)	Animal model	Ref.
InP/ZnS	650	Graphene-P-glycoprotein, GSH	Controlled release of miR22 in liver tumor cells	Mice	[161]
InP/ZnS	690	Au, SiO_2, PEG, cRGDfC	Cancer targeting (Slow clearance)	Mice	[162]
InP/ZnS	740	Anti-EGFR nanobodies (7D12)-aminoflavone	Breast cancer therapy (low toxicity)	Mice	[163]
InAs/ZnS	710	Dendron, DHLA, RDG	Tumor targeting (Rapid clearance and less toxic)	Mice	[164]
InAs/InP/ZnSe	940	MPA	Biodistribution (Rapid clearance)	Mice	[44]
InAs/ZnSe	750–920	DHLA-PEG	Lymph node imaging	Mice	[165]
$CuInS_2$/ZnS	625	N-succinyl-chitosan, FA	Tumor targeting (Less toxic)	Mice	[166]
$CuInS_2$/ZnS	838	Glycol-chitosan-coated MUA, cRGDyk	Tumor angiogenesis (rapid clearance)	Mice	[167]
$CuInS_2$/ZnS	680	BSA, Poly(ε-caprolactone), cRGD	Internal organs (liver and spleen)	Mice	[168]
$CuInSe_2$/ZnS	1100	DSPE-PEG, Anti-EpCAM	Tumor targeting (Rapid clearance)	Mice	[169]
$AgInS_2$/ZnS	610	PVP [Poly (vinyl pyrrolidone)]	Lymph node drainage imaging	Mice	[170]
$AgInS_2$	800	Pluronic F127 polymer	Tumor targeting (rapid clearance)	Mice	[171]
ZnSe/AgInS$_2$	790	MPA, R8 (octa-arginine)	Cytokinesis (low toxicity)	Mice	[172]
$AgInSe_2$/ZnS	755	Poly (acrylic acid) [PAA], cRGD	Tumor targeting	Mice	[173]

3.2. InP QDs

3.2.1. Synthesis and optical properties

Bulk InP exhibits a band gap of ~1.34 eV (~920 nm); however, InP QDs demonstrate size-dependent, tunable emission in the 500–1600 nm range due to quantum confinement and shell engineering. Nevertheless, achieving precise size and size distribution remains challenging for these materials because of complex growth kinetics and aggregation [179–181]. Methods such as hot injection, seed-mediated, and microwave-assisted techniques have been explored for the synthesis of InP QDs. These QDs are often coated with ZnS shells to enhance the PLQY and colloidal stability [182–184].

InP QDs were first synthesized in 1994 by Nozik and co-workers using a colloidal method, where chloroindium oxalate was reacted with tris(trimethylsilyl) phosphine [$(SiMe_3)_3$]P at 270℃, under varing In:P molar ratios (0.7:1–1.6:1). To the reaction mixture, TOPO was added and heated for three days, yielding InP QDs with a narrow size distribution and tunable NIR emission (600–900 nm) [179,180]. Here, the excess In^{3+} led to improved narrow-size-distributed QDs. In addition, solvent selection plays a crucial role in QD formation and its

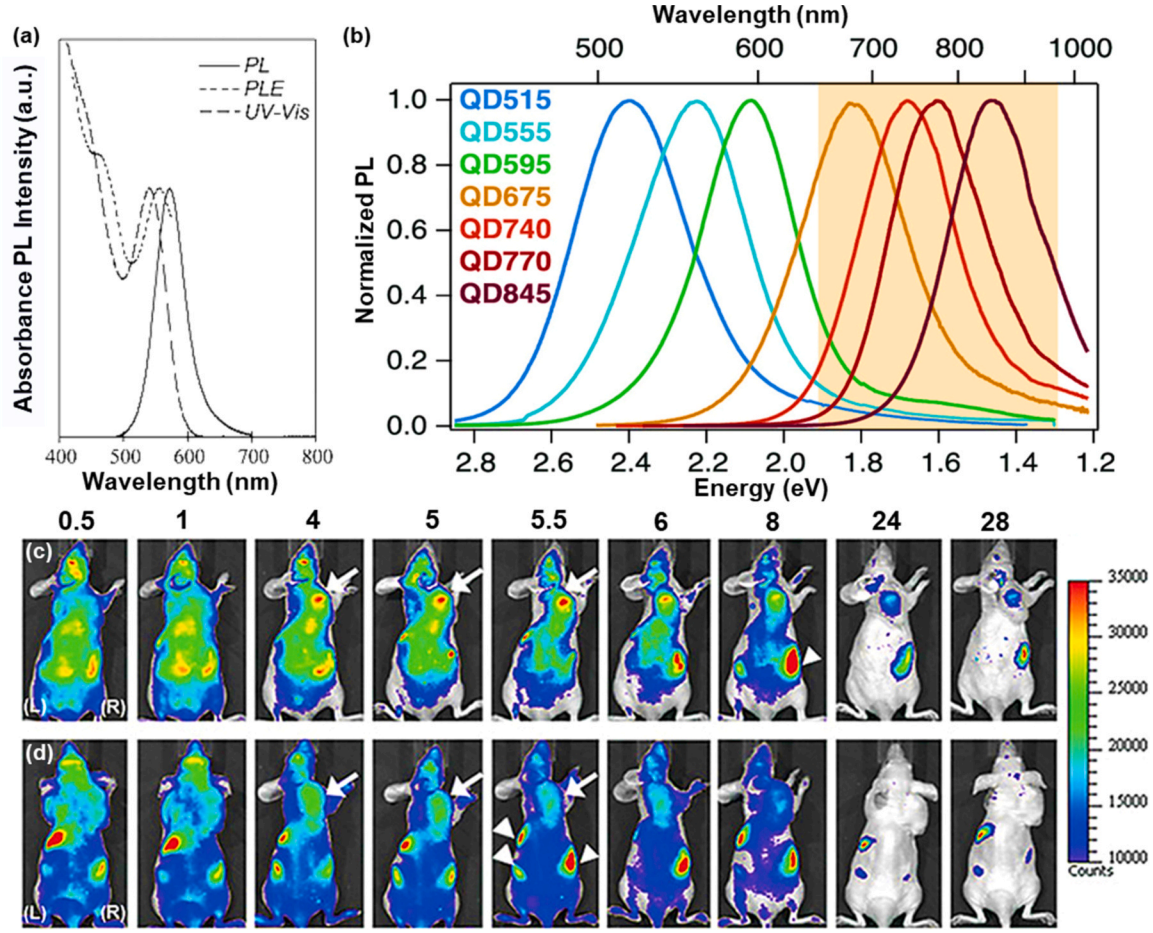

Fig. 8. Optical properties and bioimaging applications of InP QDs: (a) absorption, PL, and PLE spectra of InP QDs, (b) PL spectra of InP-ZnSe QDs with different shell thickness, and (c,d) *in vivo* images of SKOV3 tumor-bearing mice injected with (c) QD710-Dendron-RGD2 conjugates and (d) only Dendron-QD710. Reproduced with permission from (a) ref. [181]. Copyright 2002, American Chemical Society, (b) ref. [185]. Copyright 2021, American Chemical Society, and (c,d) ref. [164]. Copyright 2012, American Chemical Society.

stability. Using octadecene as the solvent, Peng's group obtained uniform-sized InP QDs with high stability [181]. Fig. 8a shows the absorption, PL, and PLE spectra of these QDs.

Despite these advances, the use of indium carboxylate precursors, such as indium myristate, indium laurate, indium oleate, and indium laurate, remains challenging, as these carboxylates often undergo undesired side reactions that reduce reproducibility, promote oxidation, and hinder scalability. Studies have shown that InP QDs can rapidly oxidize when carboxylates are used. To mitigate this issue, researchers used alternative precursors such as $[(SiMe_3)_3]P$, and tris(dimethylamino)phosphine $[DMA)_3P]$, with modified synthesis procedures including heat-up, hot injection, continuous injection, and microwave-assisted synthesis, from which hot injection and seed-mediated routes offer faster reactions and with safer solvents [186–188].

The PLQY of binary InP QDs has historically been low ($> 2.5\%$) due to surface trap states. In the hot-injection method, highly reactive phosphorus precursors such as $[(SiMe_3)_3]P$ were injected into a hot solution of indium precursors, like indium acetate or indium myristate, in the presence of coordinating solvents such as trioctylphosphine oxide (TOPO) or OAm. For example, Guzelian et al. reported that TOPO can passivate the surface of InP QDs in high-temperature synthesis, which provides stability, prevents agglomeration, and shifts the excitonic emission to the blue [183]. Moreover, the use of amines helps solvate and stabilize the precursors, suppressing dissociation and enabling better control over nucleation and growth dynamics. In contrast, seed-mediated synthesis is a two-step procedure that involves the formation of small-sized seed particles in the initial stage, followed by epitaxial growth into larger QDs [189]. Temperature plays a critical role in nucleation. At low temperatures, nucleation continues throughout the reaction, whereas at higher temperatures, it occurs rapidly and completes within 10% of the reaction time [190].

To enhance the photostability, chemical durability, and long-term stability of InP QDs, various surface modifications, such as the incorporation of inorganic shells, multi-shell structures, and crosslinked organic ligands, have been applied. CdSe, ZnSe, or ZnS shells significantly improve the stability and PLQY of InP QDs [186]. Notably, TOPO/TOP-passivated InP QDs, when etched by HF, have shown PLQY increase from 0.1% to 40%. Further enhancements have been achieved through various inorganic shells, including ZnS, ZnSe, and ZnS/ZnSe. However, alloyed ZnSeS shells tend to induce more lattice strain when compared with discrete ZnSe/ZnS shells [186]. Dennis's group demonstrated PL tunability in InP-ZnSe core-shell QDs by varying the shell thickness. Fig. 8b shows the size-tunable PL spectra of the resultant InP/ZnSe QDs, showing emission in the 515–845 nm range [185]. Similarly, ZnS passivation enhances PL intensity by 73-fold compared to the cores [186]. Recently, blue-emitting InP QDs (462 nm) with a PLQY of ~50% have been synthesized using $[(SiMe_3)_3]P$ and indium acetate with myristic acid as the stabilizing ligand, along with the development of thickness-controlled InP/ZnS core/shell QDs [191].

Ligand exchange and surface capping are essential for tuning surface reactivity, solubility, and PL QY. Replacing the carboxylate group with phosphonic acid or thiol groups enhances surface passivation and enables epitaxial ZnS shell growth. Even though ZnS shells have a lattice mismatch with InP QDs, they enhance stability by preventing surface oxidation. Halide-assisted sequential growth using $ZnI_2/ZnCl_2$ stabilizes QDs and, with subsequent ZnS coating, increases the PLQY to 94.85%. Also, depending on the halide composition, the ZnS shell induces tunable PL emission [192,193]. Similarly, Cui et al. found that embedding InP QDs into mesoporous silica (SBA-15) enhances the PLQY to 78.01%, while cation engineering through doping/alloying improves structural stability [194]. Machine-learning analysis further reveals that annealing temperature, annealing time, and Zn-based shelling critically determine particle size and emission characteristics [195].

3.2.2. Biological applications

Unlike Pb, Cd, and Hg-based QDs, InP core-only and InP-ZnS core-shell QDs exhibit low intrinsic toxicity [161,162,183–185], suppress oxidative stress through photogenerated charge carriers in the core [163,196]. Therefore, these QDs are further modified for biocompatibility and targeted imaging using antibodies, ligands, peptides, hormones, and nucleic acids [161–163,184,185,196–204]. For example, InP-ZnS QDs conjugated with L-cysteine help to detect dopamine levels. Kim et al. found fluorescence quenching of L-cysteine-capped InP-ZnS QDs with increased dopamine level [184]. Similarly, Zeng et al. conjugated InP-ZnS QDs with a combination of antibodies (monoclonal P-GP antibodies) and microRNA and loaded them onto graphene oxide for targeted drug delivery, where GSH-mediated release enables controlled microRNA delivery at the tumor site. NIR-fluorescence imaging showed enhanced accumulation of the QDs at tumor sites, and induced apoptosis in drug-resistant liver cancer cells, leading to tumor regression and slower renal elimination. Biodistribution analysis confirmed higher indium concentration in the tumor, intestine, and liver, supporting targeted drug delivery and renal clearance [161].

The *in vivo* imaging potential of InP-ZnS QDs was demonstrated using RGD peptide conjugates. For example, c(RGDfc) incorporated with gold NPs, or the anticancer drug amentoflavone-loaded VEGFR2, showed excellent tumor targeting and therapeutic effects [162,197]. Despite their *in vivo* biocompatibility and rapid clearance, macrophage activation, inflammation, oxidative and ER (endoplasmic reticulum) stress, and immunotoxicity are certain limitations [198]. Dendron-coated and RGD-conjugated InP-ZnS QDs enabled high-specificity *in vivo* imaging of ovarian adenocarcinoma cells (SKOV-3) in mouse models. Fig. 8c,d illustrates the *in vivo* images of the mice injected with QD710-Dendron-RGD_2 or QD710-Dendron with RGD_2. The conjugated QDs exhibited higher contrast and specific targeting compared to nonconjugated QDs, suggesting the possibility of the EPR (Enhanced permeability and retention) effect [164]. Folic acid (FA) conjugated InP-ZnS QDs facilitate receptor-mediated targeting of folate receptor overexpressing cancer cells (OVCAR-3) [196]. Efficient targeting and drug release were also demonstrated using InP/ZnS QDs functionalized with an amphiphilic copolymer [polylactide-b-poly(ethylene glycol)] loaded with the anticancer drug amentoflavone. When these QDs were introduced into MDA-MB-468 tumor-bearing mice, *in vivo* images showed a significant reduction in tumor cell growth [163]. Similarly, cysteine-capped InP-ZnSe QDs show anti-microbial activity against drug-resistant bacteria, including *Staphylococcus aureus*, *Bacillus cereus*, *Escherichia coli*, and *Pseudomonas aeruginosa*, *via* NIR -activated superoxide formation. Superoxide disrupts the bacterial cell function, with minimal accumulation in the liver or spleen, demonstrating efficient *in vivo* compatibility [200,201].

Nevertheless, a toxicity analysis in mice showed that InP-ZnS QDs can accumulate in the liver and spleen; however, they undergo degradation and are eliminated from the liver within 90 days, without causing any toxicity or damage to internal organs [202]. Pharmacokinetic analyses further reveal rapid clearance and negligible toxicity in serum analysis [203]. Cytotoxicity analysis in *Hydra* demonstrated that InP is less toxic than Cd-based QDs, particularly when conjugated to or coated with penicillamine, silica, or polysaccharides [204,205]. Similar studies in *Drosophila* models demonstrated the biocompatibility and *in vivo* imaging potential of InP QDs [206]. Collectively, core/shell InP QDs are safe remedies for bioimaging in living organisms.

3.3. InAs QDs

3.3.1. Synthesis and optical properties

Indium arsenide (InAs) is a group III-V semiconductor with a zinc blende (cubic) crystal structure and a narrow optical bandgap, making it ideal for various applications like NIR imaging (Fig. 9) and photodetectors [207]. Early synthesis focused on bulk crystals for diodes or sensors, typically by the Czochralski method. Thin films were later developed using chemical vapor deposition and molecular beam epitaxy. With advances in nanotechnology, researchers have begun

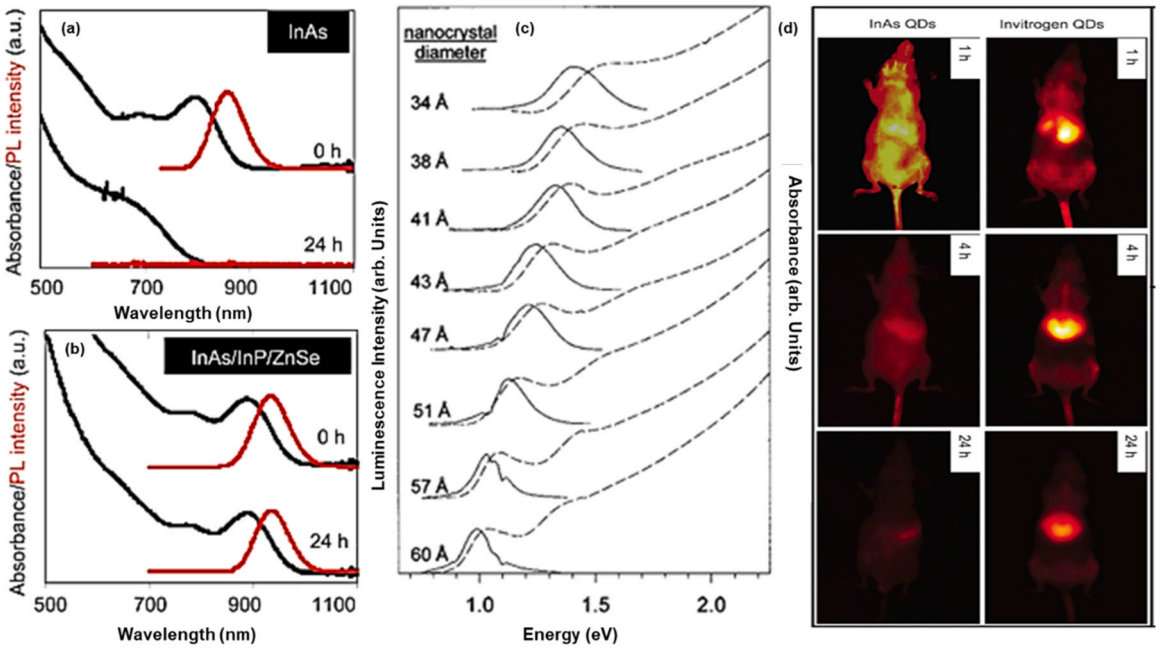

Fig. 9. (a, b) Optical properties of InAs QDs and InAs/InP/ZnSe QDs: (a) absorption and PL spectra of InAs QDs, and (b) absorption and PL spectra of InAs/InP/ZnSe QDs. (c) Size-tunable PL spectra of InAs QDs. (d) *In vivo* images of Invitrogen QD 800 ITK carboxyl (QD800) CdTe/ZnS core/shell dots and InAs/InP/ZnSe core/shell/shell in nude mice. Reproduced with permission from (a, b, and d) ref. [44]. Copyright 2008, Springer Nature, (c) ref. [212] Copyright 1996, AIP Publishing.

exploring colloidal synthesis using various approaches, aiming to produce monodisperse InAs QDs by suppressing Ostwald ripening [208]. Examples include a room-temperature reaction between indium halides and $As(SiMe_3)_3$, followed by annealing at 400 °C, dehalosilylation, and a size-focused one-pot synthesis. The first colloidal synthesis of InAs was reported by Wells et al., using a dehalosilylation reaction between indium chloride ($InCl_3$) and $As(SiMe_3)_3$ for 3 days at 75 ℃. This was further heated in benzene for 4 days, yielding a black, fluffy solid with 98% purity [209]. Studies have also shown that one-pot synthesis using a single-source precursor thermally decomposes to form InAs QDs [210]. Subsequently, the hot-injection method was widely used to achieve uniformly sized QDs. For example, Peng's group synthesized InAs QDs via a two-step hot-injection method; however, they observed degradation of the core InAs QDs. Hence, they introduced the growth of InP monolayers and ZnSe shells over the core InAs QDs, which showed excellent stability and a high PLQY (76%). Fig. 9a,b shows the absorption and PL spectra of InAs and InAs/InP/ZnSe QDs [44]. Continuous injections of the As precursor were also explored to decouple nucleation and growth, enabling better control over QD size distribution. Furthermore, InAs QDs coated with a CdSe shell extended PL tunability into the deep SWIR (Short-wave IR) region, while an additional shell of CdS or ZnS helped with efficient surface passivation, enhanced stability, and PLQY [211].

ZnSe and CdSe are commonly used shells for InAs QDs due to their wider band gaps and lattice-matching. Surfactants, such as OA and TOP, play a crucial role in controlling the stability, PLQY, size, shape, and dispersibility of QDs. Tuning the size and obtaining a narrow size distribution are significant in colloidal synthesis. Guzelian et al. adopted the synthesis method developed by Wells et al., and used TOP as both solvent and capping agent, resulting in the first size-tunable band-edge emission from InAs QDs in the NIR region (850–1200 nm) (Fig. 9c) [212]. Building on this, the Bawendi group demonstrated a scalable approach using a redox reaction between indium chloride and tris (amino)arsenic. By adjusting the temperature, they precisely tuned the emission from 700 to 1400 nm. Subsequent CdSe shell growth further extended the emission tunability, ranging from 1000 to 1500 nm [213]. However, many other studies have shown that As-TMS leads to high reactivity, and as a result, QDs tend to grow in the Ostwald ripening regime (rapid broadening of the size distribution). Some detailed studies showed that this could be controlled by choosing suitable As/In precursor ratios or by using similar precursors such as tris(trimethylgermyl) arsine and tris(isopropyl-dimethylsilyl)arsine [208]. Talapin and coworkers demonstrated nucleation kinetics by selectively choosing reducing agents. Hot-injection synthesis with the *N,N*-dimethylamine complex (DMEA-AlH_3) as the reducing agent enabled controlled reduction of As(III) to yield highly monodisperse InAs QDs. In addition, anisotropic InAs nanorods with high crystallinity have been synthesized by tuning the surfactant-precursor ratio and reaction temperature, exhibiting ~60% PLQY with ZnSe shell and tunable emission in the 1200–1800 nm SWIR [214].

3.3.2. Biological applications

Despite the presence of arsenic, InAs QDs have been reported to exhibit low toxicity, and their NIR emission enables the exploration of biological applications. For example, Allen et al. studied both *in vitro* and *in vivo* tumor vasculature imaging using InAs QDs, with excitation and PL penetration depths of up to 200 μm [215]. While Bawendi and coworkers used PEGylated InAs/CdSe/CdS QDs, which enable high-resolution cerebral vascular imaging at SWIR wavelengths [216]. Surface capping of InAs QDs has been found to increase biocompatibility, reduce toxicity, prolong circulation, and enable targeted imaging. For example, $InAs_xP_{1-x}$/InP/ZnSe QDs capped with oligomeric phosphines are demonstrated for sentinel lymph node mapping [217], and InAs/ZnSe QDs capped with dihydrolipoic acid-PEG (DHLA-PEG) for *in vivo* lymph node imaging by intravenously injecting NIR-emitting QDs into mice [165]. Targeted tumor imaging has also been demonstrated using RGD/RAD-functionalized core/shell/shell InAs/InP/ZnSe QDs, which causes selective accumulation in U87MG tumors [218]. Later, Xie et al. compared the difference between the *in vivo* fluorescence imaging of InAs/InP/ZnSe QDs capped with MPA acid and NIR-emitting CdTe/ZnSe core/shell QDs on athymic nude mice [44]. They found that NIR-emitting core/shell/shell QDs exhibit NIR fluorescence around major organs, similar to NIR-emitting CdTe/ZnSe core/shell QDs. A rapid renal clearance of MPA-capped InAs QDs was observed within 25 h. However, CdTe/ZnSe QDs accumulated at different body parts (Fig. 9d). MTT assay showed lower toxicity of In-based QDs than CdTe

QDs. In addition, deep-tissue imaging has been demonstrated with InAs/ZnCdS core-shell QDs. Hence, InAs QDs are useful for bioimaging, deep tissue penetration, and low autofluorescence in the NIR-II window.

Although InAs QDs are promising for NIR bioimaging, concerns regarding their long-term safety remain. Toxicological studies in male hamsters have indicated potential risk to their reproductive organs. InAs causes testicular damage, reduced testicular weight, and decreased sperm count, with Sertoli cells identified as potential targets of toxicity [219]. Further studies found that InAs can induce severe histopathological changes in testes, including vacuolization of the seminiferous epithelium [220,221]. These findings underscore that, although InAs QDs offer advantages for *in vivo* imaging, potential health risks and toxicity must be carefully considered.

3.4. InSb QDs

III-V semiconductors such as InSb have a narrow bandgap (0.17 eV at 300 K), enabling strong NIR-SWIR responses. Early synthesis techniques included molecular beam epitaxy (MBE) and the Stranski-Krastanov (SK) method to produce crystalline QDs with limited scalability. The first colloidal synthesis of InSb QDs was reported by Liu et al. *via* hot injection of $InCl_3$ and $Sb[N(Si(Me)_3)_2]_3$ dissolved in TOP/toluene into a mixture of OAm and lithium triethylborohydride heated at 260 °C for 20 min [222]. Subsequent coating with CdSe or CdS shells and controlling the reaction temperature and time enabled tunable size (3.3–6.5 nm) and PL (1200–1750 nm). Later, the Kovalenko group developed a scalable and controllable hot-injection method to produce InSb QDs using indium chloride and tris(dimethylamido)antimony, with ligands such as TOP and trioctylamine (TOA) to precisely control the morphology and stability of QDs [223]. Subsequently, researchers have demonstrated a stepwise crystallization approach [224], and a one-pot synthesis strategy [225] for tunable NIR-SWIR absorption [226], and ligand engineering for enhanced optical properties [227,228]. Importantly, core/shell/shell (InSb/InP/CdS) and Cd doping enhance PLQY and stability [229]. Recently, Seo et al. synthesized monodispersed, photostable, SWIR tunable, and high-quality InSb core/shell QDs with tunable absorption across the 1000–1700 nm SWIR range [230]. Although these QDs have been widely used in IR photodetectors, their applications in bioimaging remain unexplored.

3.5. Gallium-based (GaN, GaP, GaAs, and GaSb) binary QDs

3.5.1. Synthesis and optical properties

Conventionally, Gallium nitride (GaN) NPs have been synthesized by laser ablation, molecular beam epitaxy, chemical vapor deposition, and laser ablation, producing 2–12 nm particles [231–235]. Subsequent approaches, such as droplet epitaxy and solvothermal synthesis using gallium acetylacetonate with urea or $LiNH_2$ at 180–250 °C for 12–24 h, result in controlled formation of GaN QDs [236]. Later, Pan et al. reported a room temperature synthesis by reaction of Li_3N and GaX_3 (X = Cl, Br, I) in diethyl ether, yielding ~10 nm QDs with wurtzite and zincblende phases and strong emission at 3.4 eV [237]. Microemulsion [233] and plasma aerotaxy methods [232] further improved size control and optical properties, with recent studies exhibiting tunable emission in the UV-Vis range, attributed to size-dependent quantum confinement effects [235].

The synthesis of GaP has evolved to address challenges such as high vapor pressure and the need for high-purity crystals. Early synthesis methods, such as vapor-phase synthesis [238], Czochralski, Bridgman techniques, sublimation, and chemical vapor deposition impart limited control over QD synthesis. In contrast, solvothermal synthesis using gallium chloride and sodium phosphide at elevated temperatures yields 5–10 nm GaP QDs, [239], and the hot-injection method using gallium chloride and $[(SiMe_3)_3]P$ in TOP to produce ~ 4.6 nm GaP QDs with an emission peak at 486 nm [240]. Furthermore, alloyed $In_{1-x}Ga_xP$/ZnS core-shell colloidal QDs by cation-exchange reaction resulted in high PLQY (~75%) and tunable emission (474–627 nm) by varying the gallium concentration.

GaAs NCs have been synthesized using various conventional methods, including metal-organic chemical vapor deposition, gas-aerosol electrostatic deposition, and sputter coating [241]. Later, Wells and colleagues demonstrated synthesis of GaAs QDs using a single-source precursor ($AsCl_3Ga_2$ and phosphine-arsinogallanes) and using coordinating solvents such as monoglyme or diglyme, could precisely control QD size [242]. Additionally, 2–6 nm GaAs QDs were also obtained by tuning the precursor concentration and controlled reaction durations [243].

Early synthesis of GaSb primarily followed the SK growth method, droplet epitaxy on GaAs, and on a patterned GaAs buffer layer [244,245]. Later, the Wells group developed colloidal GaSb QDs using tert-butylgallium-antimony precursors with defined Ga-Sb bonding to produce colloidal GaSb QDs (~10–12 nm) via thermolysis of $(Sb(SiMe_3)_3)$ and diethyl gallium chloride (Et_2GaCl) in hexane [246].

3.5.2. Biological applications

Ga-based QDs are promising for electro-optical devices [247] and photocatalysis [248]; however, their biological applications are limited. Jewett et al. demonstrated that GaN is biocompatible and less toxic, even before surface functionalization. Although shell preparation and surface modification suppress the release of Ga ions, trace amounts of Ga (III) released in a cell culture medium demonstrated improved cell adhesion [249]. Similarly, Young et al. reported that GaN substrates support the growth and differentiation of granule neurons [250]. Nevertheless, focused cytotoxic and pharmacokinetic studies are required to evaluate the biocompatibility, biodistribution, and toxicological impact of GaN QDs before *in vivo* applications.

Similarly, the *in vivo* biocompatibility of GaP remains poorly investigated. A recent study by Vogel's group demonstrated the pulmonary toxicity associated with GaP nanowires (NWs). They found that female C57BL/6j mice administered with varying doses of GaP NWs resulted in lung accumulation, genotoxicity, and partial degradation in the liver, followed by secondary accumulation in the liver, spleen, uterus, and brain [251]. In another study, implantation of GaP discs into the abdominal walls of rats to study the tissue reaction, however, resulted in a chronic inflammatory response, which further caused gallium accumulation in the brain, liver, and kidneys [252].

GaAs QDs also remain unexplored in *in vivo* studies, due to concerns about the occupational toxicity of bulk GaAs. Several studies have shown that GaAs exposure causes pulmonary toxicity and abnormal gene expression [221]. In addition, GaAs has been reported to cause testicular toxicity in hamsters, characterized by spermatid retention and reduced epididymal sperm count. In contrast, comparable experiments with arsenic oxide did not result in testicular toxicity, indicating that toxicity is caused by gallium [219]. Studies by Carter et al. demonstrated that oral administration of GaAs to rats leads to significant weight loss and increased porphyria [253]. These findings further underscore the toxicity of arsenic and gallium for any biological applications.

Studies have reported that continuous exposure to Ga compounds like GaSb, GaAs, or GaN leads to gallium poisoning [254], which causes gastrointestinal problems, skin issues, fatigue, and headaches. In addition, Sb is classified as a possible carcinogen and has been associated with pulmonary toxicity [255]. Recently, Fujihara et al. reported that even at low concentrations, GaSb can penetrate the skin barrier and reduce fibroblast viability [256].

In general, Gallium-based (GaN, GaP, GaAs, and GaSb) binary QDs exhibit significant toxicity concerns in biological systems, including pulmonary toxicity, testicular toxicity, organ accumulation, and reduced cell viability.

4. Group I-III-VI QDs

4.1. $CuInX_2$ (X = S, Se, Te) QDs

4.1.1. Synthesis and optical properties

The synthesis of copper indium chalcogenide QDs ($CuInX_2$; X = S, Se, Te) is a complex process that requires careful control over the relative reactivity of the metal cations (Cu^+ and In^{3+}) with chalcogenide (S^{2-}, Se^{2-}, and Te^{2-}) precursors. Various synthetic approaches have been employed, including solvothermal, hot injection, hydrothermal, microwave-assisted, and heating-up methods. A significant advancement in synthesis has resulted from the use of metal precursors with Cu-S and In-S bonds, which help maintain phase purity and control particle size [257]. In particular, alkanethiol-mediated synthesis introduces excess thiol ligands, which help balance reactivity and produce high-quality $CuInX_2$ QDs. Also, thermal decomposition of metal salts such as ethyl xanthates and dithiocarbamates in OAm at elevated temperatures leads to the formation of $CuInS_2$ QDs. Alkanethiol-mediated synthesis effectively balances the reactivity of Cu^+ and In^{3+} with sulfur anions [45,258,259]. Cation exchange is another method to obtain well-defined $CuInS_2$ QDs. For example, Xia et al. synthesized $CuInS_2$ QDs with 2.7–6.1 nm diameter by partial cation exchange of Cu^+ ions with In^{3+} in $Cu_{2-x}S$ template crystals [260]. The significance of the Cu/In ratio in $CuInS_2$/ZnS QD synthesis and its effect on stability were studied by Grandfils's group, where they demonstrated that a 1:4 ratio leads to excellent PL and stability; in contrast, a 1:1 ratio leads to rapid PL quenching [261]. Highly luminescent $CuInS_2$ QDs with a high PLQY of ~90% have been developed by a scalable reaction between Indium acetate and Cu(I) Iodide at 230℃, followed by CdS or ZnS shell passivation. Fig. 10a shows the absorption and PL spectra of $CuInS_2$ QDs, with the inset showing the size dependency of the QDs on their PL energy [262]. $CuInS_2$ QDs are direct-bandgap semiconductors with relatively small band gaps, and can exhibit tunable emission from visible-to-NIR optical absorption and emission *via* size tuning [260,263–265]. For example, Peng's group demonstrated the PL tunability in the visible-NIR region (500–950 nm, Fig. 10b) for monodispersed $CuInS_2$/ZnS, where the growth of the ZnS shell on the $CuInS_2$ QD core increased the PLQY from 3% to 30%. The ZnS shell on the $CuInS_2$ QD core not only drastically increases the PLQY but also provides good long-term stability [45]. Unlike CdSe/CdX-type QDs, ZnS shell formation on the core of $CuInS_2$ QDs blue-shifts the emission spectra with an increase in the PLQY, attributed to alloying or cation exchange on the surface of the QDs. Water-soluble $CuInS_2$/ZnS QDs with excellent stability, biocompatibility, and tunable properties are crucial for bioimaging applications. To render hydrophobic QDs dispersible in aqueous media, various strategies, such as silica coating, ligand exchange, and amphiphilic polymer encapsulation, have been widely used, enabling their use in live-cell imaging [264,266–268].

Although $CuInSe_2$ QDs have been less explored, they are typically synthesized *via* thiol-mediated or hot-injection methods. Early reports demonstrated NIR-emitting $CuInSe_2$ QDs (820–940 nm), with a low PL quantum yield [269]. Subsequent hot-injection approaches using bis (trimethylsilyl) selenide as the chalcogenide precursor resulted in 2.0–3.5 nm $CuInSe_2$ QDs with 25% PLQY due to the strong exciton confinement [270]. Similar to $CuInS_2$/ZnS systems, surface passivation significantly enhances the PLQY of $CuInSe_2$ QDs, making core-shell NPs promising for *in vivo* imaging. For example, Park et al. reported a one-pot synthesis of $CuInSe_2$/ZnS core/shell QDs with PLQY of up to 60%, accompanied by blue-shifted emission with a broad PL spectrum, indicating the formation of an alloy at the core-shell interface with a broader size distribution. Fig. 10c shows the comparison of absorption and PL spectra of $CuInSe_2$ QDs before and after ZnS passivation. Following

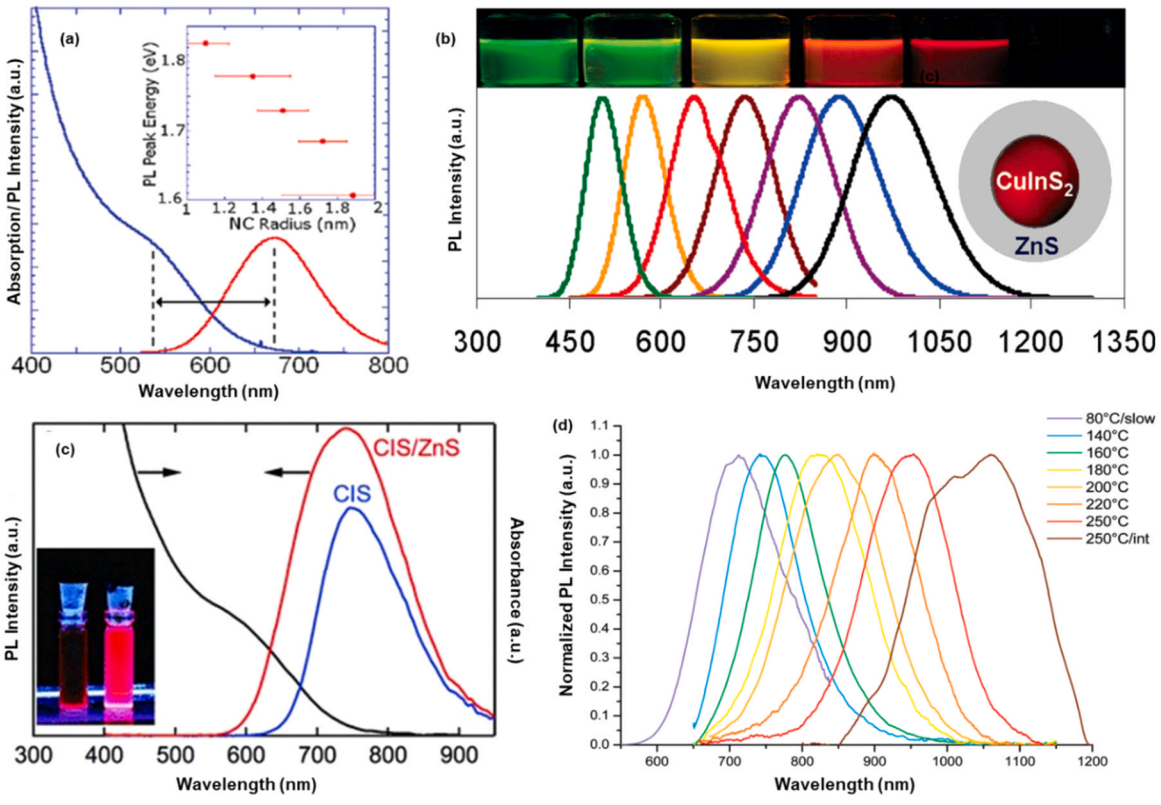

Fig. 10. Optical properties of $CuInS_2$ and $CuInSe_2$ NCs: (a) absorption and PL spectra (inset: the size-PL energy relationship), (b) PL tunability of $CuInS_2$/ZnS, (c) absorption and PL spectra of $CuInSe_2$ and with ZnS passivation, and (d) PL tunability with different reaction temperatures. Reproduced with permission from (a) ref. [262]. Copyright 2011, American Chemical Society, (b) ref. [45]. Copyright 2009, American Chemical Society, (c) ref. [265]. Copyright 2011, Wiley-VCH, and (d) ref. [47]. Copyright 2010, American Chemical Society.

thiolation and lipid coating, these QDs have been successfully applied in *in vivo* imaging [265]. Similarly, Cassette et al. compared the optical properties of $CuInSe_2$ QDs with and without ZnS surface passivation. They demonstrated that ZnS passivation not only enhanced PL intensity but also enabled tunable emission from 700 to 1040 nm by varying the synthesis temperature (Fig. 10d) [47].

The synthesis of $CuInTe_2$ QDs is highly intricate due to the strong affinity between soft Cu^+ cations and Te^{2-} anions. The first colloidal synthesis of $CuInTe_2$ QDs was unlocked by Kim et al. by the reaction with indium acetate, copper iodide, and tri-n-octylphosphine telluride in the presence of DT as a surfactant. These QDs exhibited tunable emission in the 800–1000 nm range [271]. Subsequently, amide-promoted synthesis with lithium bis(trimethylsilyl)amide enhances nucleation kinetics, yielding smaller indium-rich $CuInTe_2$ QDs at higher temperatures [272]. Alternatively, a sequential cation-exchange reaction helps transform CdTe QDs into Cu_2Te QDs, which, when mixed with an In^{3+} solution to form $CuInTe_2$ QDs, enables controlled compositional transformation [273]. Typical I-III-VI QDs, their PL wavelengths, bioconjugated molecules, and *in vivo* applications are listed in Table 4. Despite their NIR emission, the biological applications of $CuInTe_2$ QDs remain underexplored.

4.1.2. Biological applications

$CuInS_2$-based QDs, particularly those emitting in the NIR region, have been widely used for tumor targeting and *in vivo* imaging owing to their low cost, high durability, and low toxicity [47,166,167,169,269–271,273–278]. Functionalization with biomolecules enables diverse sensing and imaging applications. For example, fibrinogen-conjugated $CuInS_2$ QDs enable the detection of thrombin in human serum by forming water-soluble QD complexes with fibrinogen, *via* the PL quenching mechanism [274]. Similarly, as-synthesized QDs have been conjugated with various molecules, such as IgG-ab, chitosan, GSH, MPA, transferrin, and aflatoxin, and applied *in vitro* and *in vivo* applications [166,167,266,275–279]. For example, Han's group conjugated lipophilic silane micelles to holo-transferrin for cancer cell imaging [279]. Spangler et al. conjugated $CuInS_2$/ZnS with IgG antibodies using EDC/NHS cross-linkers for cellular imaging (THP-1 cells) [266]. $CuInS_2$ QDs were also employed to detect lysozyme by exploiting electrostatic interactions and electron transfer with a cationic polyelectrolyte [276]. Amphiphilic polymer-based conjugation further expanded the applications of $CuInS_2$ QDs. For example, PEG-containing amphiphilic polymers conjugated with aflatoxin BI proteins enable quantitative immunoassays. Similarly, amphiphilic bioconjugates with BSA (Bovine Serum Albumin) as the hydrophilic segment and PCL (poly(Ɛ-caprolactone)) as the hydrophobic segment facilitate targeted cell imaging, which was further conjugated with cRGD peptide for enhanced tumor targeting in female nude mice [168]. Folate-N-succinyl-N'octyl chitosan-modified $CuInS_2$/ZnS QDs showed excellent bioprobes for targeted, multiplexed tumor imaging [166]. In addition, glycol chitosan-coated $CuInS_2$/ZnS-11-mercaptoundecanoic acid showed significant tumor-targeting efficiency. When these NPs were injected into RR1002 tumor-bearing mice, the NPs accumulated predominantly in the liver and spleen, with NIR PL intensity increased prominently by 24 h, followed by renal clearance (Fig. 11a) [167]. In contrast, although

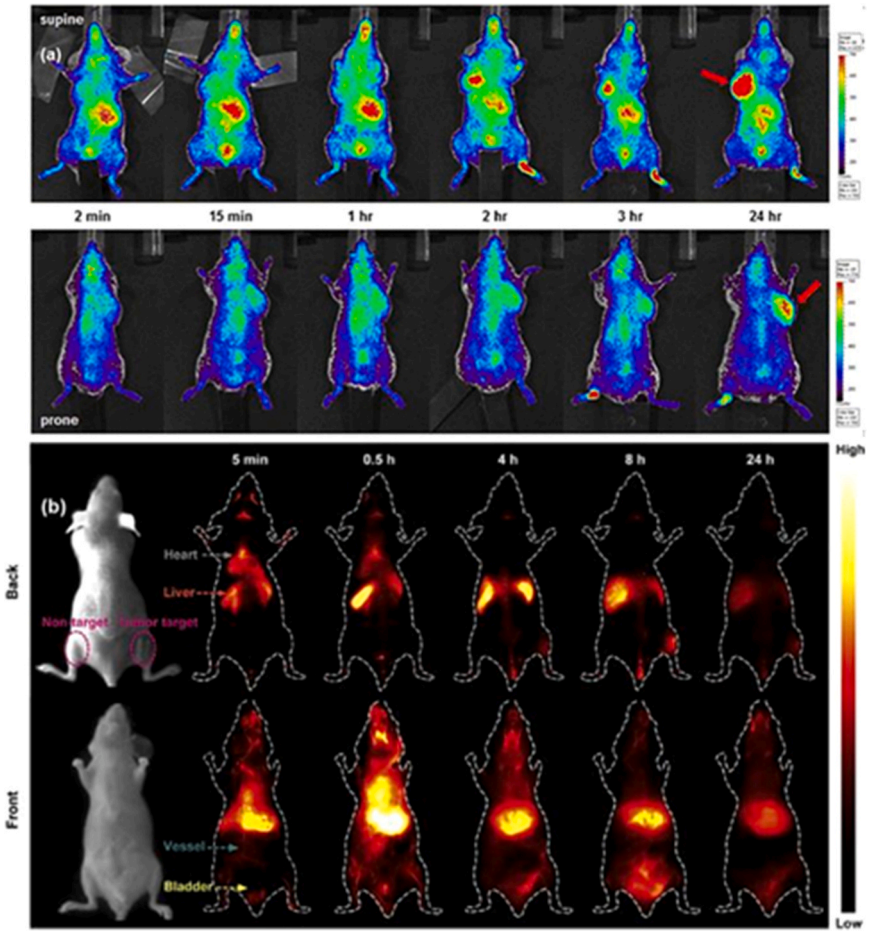

Fig. 11. (a) NIR fluorescence images of RR1022 tumor-bearing mice showing time-dependent accumulation after intravenous injection with cRGDyk-GCM-QDs, (b) NIR fluorescence images of mice injected with a $CuInSe_2$/ZnS-EpCAM nanobioprobe with time and its rapid clearance. Reproduced with permission from (a) ref. [167]· Copyright 2017, Springer Nature, and(b) ref. [169]· Copyright 2020, Elsevier Ltd.

$CuInSe_2$ QDs are widely studied for optoelectronic applications such as light-emitting diodes and solar cells, their biological applications remain underexplored. Some studies show that EpCAM (epithelial cell adhesion molecule)-conjugated $CuInSe_2$/ZnS QDs serve as effective nanobioprobes for regional lymph node detection, specifically binding to MCF-7 breast cancer cells. The tail-vein injection of Ab QDs into tumor-bearing mice showed that the QDs circulate *via* the blood and accumulate in the heart and brain, then spread to other organs, as demonstrated in Fig. 11b. *In vivo* imaging of the tumor becomes prominent between 0.5 and 8 h post-injection, with increased NIR fluorescence at the tumor sites. Moreover, rapid clearance was observed, revealing excellent biocompatibility of $CuInSe_2$/ZnS QDs [169].

Although copper indium chalcogenide QDs offer tunable NIR properties for noninvasive imaging [47,166–169,266,267,269–271,273–277,279], their long-term safety remains a concern due to accumulation in internal organs. As a result, their toxicity was assessed in different organisms using and models. For example, Liu and co-workers investigated the degradation and cytotoxicity of $CuInS_2$/ZnS QDs in *Caenorhabditis elegans*, revealing that surface modification with o-carboxymethyl chitosan prevented the oxidation of $CuInS_2$/ZnS for up to 96h [278]. Similarly, Dennis's group evaluated the cytotoxicity of core-only $CuInS_2$, Zn-alloyed $CuInS_2$, and surface-passivated $CuInS_2$/ZnS QDs in a murine model. They reported that core-only $CuInS_2$ QDs are highly toxic and rapidly degrade, resulting in accumulation in the kidneys, liver, spleen, lungs, and heart. Zn alloyed $CuInS_2$ QDs also showed significant toxicity [280]. In contrast, surface-passivated $CuInS_2$/ZnS QDs exhibited much less stress and toxicity with minimal degradation. Further conjugation with PEG demonstrated excellent biocompatibility in mouse models. Similarly, Wang's group reported that PEGylated $CuInS_2$/ZnS QDs showed minimal toxicity and enhanced biocompatibility compared with non-PEGylated QDs [281]. $CuInTe_2$ QDs show NIR emission; however, their biological applications have yet to be demonstrated [271]. In general, the copper indium chalcogenide QDs offer strong potential for biosensing and imaging, owing to their high PL QYs, NIR absorption and emission, and affinity for bioconjugation.

4.2. $AgInX_2$ (S, Se) QDs

4.2.1. Synthesis and optical properties

$AgInS_2$ QDs are ternary QDs exhibiting high photostability, tunable emission, and promising biological applications, owing to their low toxicity and biocompatibility. These QDs are synthesized by various chemical methods, such as hot injection, hydrothermal, or one-pot solvothermal synthesis, enabling control over crystallinity and particle size [170,282–286]. Surface passivation using ZnS significantly enhances PL intensity, particle size, and tunable emission. However, at higher reaction temperatures, Zn ions diffuse to the core QDs. In another study, Ag-Zn-In-S QDs show composition-dependent PL tunability, with increased Ag/Zn stoichiometries, the absorption band edge and PL emission blue shifted, with the highest PLQY ~34% at a 1:1 ratio of Ag/Zn (Fig. 12a,b) [286]. PL tunability has also been achieved through cation-exchange reactions. Song et al. demonstrated the conversion of Ag_2S QDs to $AgInS_2$ and Ag-Zn-In-S QDs by precisely controlling the cation ratio during ion-exchange reactions [287]. In contrast, $AgInSe_2$ QDs have been relatively less explored. These QDs have also been synthesized *via* colloidal synthesis, microwave-assisted, high-pressure, thermolysis, ion exchange, and aqueous phase methods, employing capping agents such as TOP, ZnSe, MPA, thioglycolic acid, or GSH [50,173,288–290]. For example, the Tsolkile group synthesized water-soluble $AgInSe_2$/ZnSe QDs stabilized with thioglycolic acid and gelatin. They compared the PL properties of $AgInSe_2$ QDs with and without ZnSe, and found that ZnSe passivation results in blue-shifted PL with enhanced emission intensity (5.6%), while maintaining the characteristic absorption shoulder at 425nm (Fig. 12c,d) [50].

4.2.2. Biological applications

Similar to other Ag- and In-based QDs, $AgInS_2$ QDs exhibit high absorption coefficients and NIR emission, making them promising for deep-tissue imaging [171,172,286,291]. These QDs can serve as

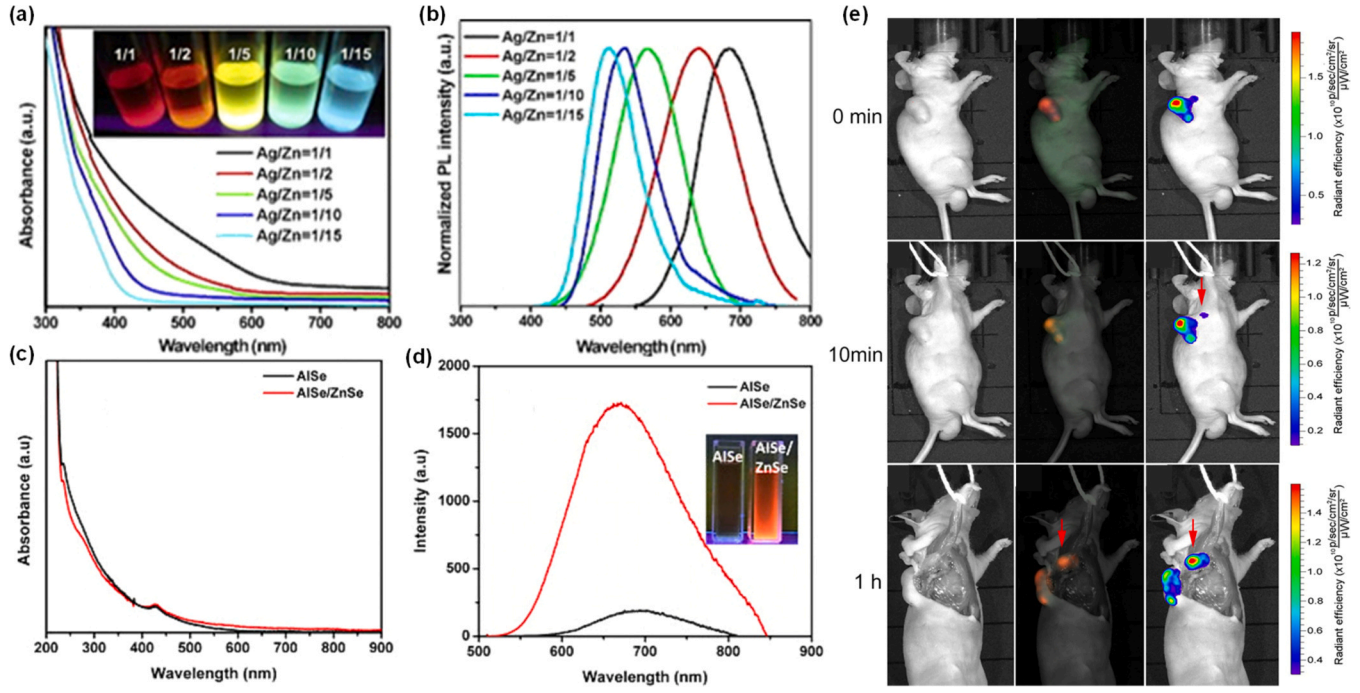

Fig. 12. (a, b) Optical properties of $AgInS_2$/ZnS QDs, (a) Absorption spectra, and (b) PL tunability of $AgInS_2$/ZnS QDs in different Ag/Zn ratios. (c, d) Optical properties of $AgInSe_2$ QDs, (c) Absorption spectra, and (d) PL spectra of $AgInSe_2$ QDs and $AgInSe_2$/ZnSe QDs. (e) *In vivo* images of H460 tumor-bearing mice injected with $AgInS_2$/ZnS QDs with the capping of PVP. Reproduced with permission from (a,b) ref. [286]. Copyright 2014, Elsevier Ltd., (c, d) ref. [50]. Copyright 2020, Elsevier Ltd. (e) ref. [170]. Copyright 2021, American Chemical Society.

high-contrast biological probes for live-cell and tumor imaging. For example, $AgInS_2$ QDs encapsulated within Pluronic F127 triblock copolymer micelles exhibit improved biocompatibility, preferential accumulation in the liver, and gradual renal excretion within 24h, underscoring favorable pharmacokinetics for practical applications [171]. Similarly, PAA- and MAA-capped $AgInS_2$/ZnS QDs showed very low cytotoxicity and rapid renal excretion [291]. Studies from Yang's group demonstrated the imaging potential of $AgInS_2$ QDs in mouse models. Intratumoral injection of poly(vinyl pyrrolidone) (PVP)-modified $AgInS_2$/ZnS QDs into a subcutaneously inoculated H460 tumor in a mouse enabled detection of NIR emission from the QDs through both the tumor tissue and the overlaying skin, as well as the draining lymph node (Fig. 12e). Although the emission intensity of the QDs decreased considerably within 10min post-injection, the tumor drainage lymph node became clearer after skin removal. Nevertheless, systemic injection of these QDs did not show any significant targeting efficiency to the tumor. Conversely, these QDs accumulated in the liver without affecting histopathology [170].

Beyond tumor imaging, $AgInS_2$ QDs have also been applied to stem cell tracking. ZnS-coated and octa-arginine-conjugated $AgInS_2$ QDs enabled high-efficiency labeling and quantitative imaging of adipose-derived stem cells, helping analyze biodistribution in various body parts, such as the lungs [172]. Similarly, $AgInSe_2$ QDs have been explored by some researchers for biological applications. For example, water-soluble NIR-emitting (600–950nm) AgInSe2/ZnS conjugated with RGD peptides demonstrates intense tumor-localized fluorescence in MDA-MB231 tumor-bearing mice within 6h post-injection, signifying a potential candidate for applications [173]. However, there has been no clear in-depth study of the cytotoxicity of these QDs, which is essential for evaluating their biocompatibility.

Although water-soluble and surface-functionalized indium-based binary QDs hold promise for many bioimaging applications, from tumor targeting, lymph node mapping, and vasculature imaging, addressing their degradation and retention in the reticuloendothelial system requires detailed pharmacological studies.

4.3. Ga-based bimetallic chalcogenide QDs ((Ag, Cu) Ga (S, $Se)_2$) QDs

4.3.1. Synthesis and optical properties

Yang's group synthesized highly luminescent $CuGaS_2$ QDs *via* hot injection of sulfur into copper iodide, gallium iodide, DT, and OAm at 180 °C. These QDs were coated with ZnS shells, resulting in an average size of 4.2 nm, with a broad emission peak in the entire visible region [292]. Furthermore, incorporating Zn into Cu-deficient sites results in stable blue-shifted PL and an increase in the band gap from 2.95 to 3.14 eV [48]. Similarly, Kim et al. synthesized $CuGaS_2$/ZnS QDs *via* hot injection, and ZnS shell coating yielded QDs with an average size of 6.1 nm with PL emission at 491 nm [293,294]. Cation exchange of Cu^+ with Ga^{3+} in $Cu_{2-x}S$ and $CuInS_2$ QDs using $GaCl_3$-TPP (triphenylphosphite) resulted in $CuGaS_2$ QDs with a blue-shifted emission and 10-fold PLQY enhancement [295,296]. The growth of the $CuGaS_2$ QDs can be controlled by changing factors such as temperature, solvent polarity, ligand, and Zn concentration, enabling precise tuning of QD morphology [297,298]. Likewise, $CuGaSe_2$ QDs were first synthesized using the hot-injection method. Copper and gallium acetylacetonate in OAm, as the metal precursor, were injected into selenium powder in OAm at 250 °C, followed by annealing for 1 h to promote effective crystallization and phase purity [299]. The resulting QDs had an average size of 16 nm with an absorption peak at 729 nm. In addition, nanosheets and plate-like 2D $CuGaSe_2$ structures have also been reported.

$AgGaS_2$ and $AgGaSe_2$ are ternary QDs that have attracted significant attention for their chemical stability and biocompatibility. Among various synthesis methods, hot-injection enabled the synthesis of high-quality $AgGaS_2$ QDs [300,301]. For example, hot-injection of gallium acetylacetonate and silver iodide to sulfur powder dissolved in OAm and DT at 305 ℃, followed by capping with a ZnS shell, yielded ~5 nm $AgGaS_2$ QDs with a high PLQY and emission at 482 nm. Tunable PL emission, QD size, stability, and PLQY were further enhanced by capping with CdSeS [302], $AgInS_2$[303], and GaS_x[304] and controlling the Ga/Ag ratio [305].

Early synthesis methods for $AgGaSe_2$ were limited by oxidation, high-temperature requirements, and poor crystal quality [306]. Later, Torimoto's group synthesized colloidal Ag-(In, Ga) [$(S, Se)_2$] QDs by a two-step thermolysis reaction [307]. Metal precursors (silver acetate, indium acetylacetonate, and gallium acetylacetonate) with thiourea/selenourea in a 1:1 ratio were heated at 100 °C for 30 min, followed by heating at 250 °C for an additional 30 min under an inert atmosphere, resulting in $AgGaSe_2$ QDs. Moreover, bandgap engineering by varying Se/(S+Se) or In/Ga ratio resulted in tunable PL from 580 to 890 nm [308]. Similarly, shells such as GaS_x and ZnSe improve stability, PLQY, and emission tunability across the visible region (443–632 nm) [309].

4.3.2. Biological applications

Water-soluble $CuGaS_2$/ZnS QDs were obtained using various ligands such as MPA and GSH, which exhibited well-dispersed and stable QDs. MTT assay on MCF-7 cells revealed low cytotoxicity and stable cell viability, demonstrating biocompatibility for biological applications [310]. Similarly, biocompatibility of $AgGaSe_2$/ZnSe QDs has been achieved through ligand exchange using metallated mercaptoundecanoic acid (Zn-MDA) [309]. Although Zn-MDA exhibited greater inherent toxicity than MPA, the ligated QDs showed higher biocompatibility. Additionally, ZnSe shells effectively reduced cation leakage, contributing to the overall lower toxicity of the QDs [309]. However, further studies are necessary to understand the bioimaging potential of these QDs.

5. QDs for PDT

PDT has emerged as a minimally invasive treatment for cancer and various microbial infections. It relies on light-activated photosensitizers (PSs), called photodrugs, which degrade biomolecules and induce cell death *via* ROS generation or direct electron transfer. The ROS generation itself involves energy or electron transfer from a photoactivated PS and proceeds through two main pathways: Type I and Type II. In the Type I pathway, electron transfer from the photoexcited PS to a biomolecule or dissolved oxygen generates reactive radical ion species such as superoxide, whereas the Type II pathways involve energy transfer to ground-state oxygen, generating singlet oxygen ($^1O_2$), and subsequent ROS formation [311–315]. Details of these pathways are discussed in the following section. Organic photosensitizers, such as porphyrins and phthalocyanines [291,292], have been extensively used in clinical settings; however, they have certain limitations. These include photobleaching, low absorption cross-sections, narrow absorption bands, and limited bioavailability. These issues led to the search for nanomaterials for PDT [3,313,316,317]. Although chemical modifications can yield NIR-absorbing PSs, most organic PSs rely on dissolved oxygen and the ROS pathway in PDT, limiting their PDT efficiency under hypoxic conditions.

Over the past 25 years, researchers have explored nanodrugs, including inorganic and carbon/graphene QDs and NCs [318]. These nanodrugs have superior properties compared to organic PSs, including broad and near-infrared (NIR) light absorption, large absorption cross-sections, high photostability, bright PL, and a large, flexible surface area. Therefore, these nanodrugs enable not only efficient utilization of light sources and deep-tissue applications but also the conjugation of targeting molecules, enabling site-specific, image-guided therapy. Like classical PS drugs, these nanodrugs generate ROS such as singlet oxygen ($^1O_2$) and superoxide ($O_2^{\bullet-}$) through Type I and Type II photosensitization mechanisms, in addition to direct, targeted, electron-transfer-induced damage to biomolecules, cells, and tissues, minimizing damage to healthy cells and tissues [313,316]. The

following section covers mechanistic, *in vitro*, and *in vivo* studies on semiconductor NP-mediated PDT, highlights the limitations of Cd-based II–VI QDs, and underscores the advantages of emergent III–V and I–III–VI QDs [100,319].

Cd-based QDs were initially studied for PDT because of their bright luminescence and tunability. Early research by Samia et al. showed that CdSe QDs could act as energy donors for phthalocyanine PDT *in vitro* [317]. Further studies revealed that CdTe QDs directly produced $^1O_2$ in cell cultures. *In vivo*, CdSe/ZnS–photosensitizer conjugates reduced tumor growth in nude mice. However, cadmium toxicity and oxidative degradation limited their use in medicine [320]. Encapsulation in silica, PEGylated lipids, or polymers stabilizes QD core or core-shell structures and enhances biocompatibility. Despite these efforts, regulatory challenges for cadmium-based materials remain significant.

To reduce toxicity issues, Ag_2S, Ag_2Se, $AgInS_2$, $CuInS_2$, InP, and InAs QDs emerged as Cd-free alternatives. Studies have shown that these QDs generate ROS upon visible-light excitation, leading to apoptosis in cancer cells. Limited *in vivo* studies suggest they can suppress tumor growth with lower toxicity, though proper surface modification remains essential. For example, $CuInS_2$ QDs have gained popularity for their low toxicity and strong Type I photosensitization under low oxygen conditions. PEGylated $CuInS_2$/ZnS NCs accumulated in tumors through the EPR effect, inhibiting xenograft growth in mice when exposed to visible light [321]. InP QDs provided similar results with effective ROS production [201].

We summarize studies in cellular and animal models demonstrating the ability of these QD-based nanodrugs to inhibit tumor growth and combat infections. We also include mechanisms underlying $^1O_2$ production and electron-transfer pathways, while addressing issues related to toxicity, resistance to low-oxygen conditions, and the challenges of transitioning from cell-based assays to clinical use. This section summarizes recent advances in nano-drug-based PDT. It clarifies the potential and challenges of such drugs, while also outlining perspectives on lead-free QDs, NIR-II excitation, and multifunctional nanotheranostic platforms.

5.1. Mechanistic aspects

Photochemical reactions mediated by semiconductor photosensitizers follow two distinct pathways: Type I (electron-transfer) and Type II (energy-transfer), each with distinct mechanisms and therapeutic implications. In the Type I mechanism, as in the PSs, NCs absorb photons and generate electron-hole pairs called excitons, which exist as optically allowed bright excitons, analogous to molecular singlet states, or optically forbidden dark excitons, analogous to molecular triplet states [319,322]. Here, a high-energy electron acts as a powerful reducing agent (an electron-donating state). In contrast, the hole acts as a potent oxidizing agent (an electron-accepting state). The active electron (or hole) then interacts with biomolecules or oxygen to initiate a chain of redox reactions [316,323].

Although a photoexcited QD in the singlet state can generate a charge-separated state by electron transfer to or from a nearby molecule, the spin-allowed interband relaxation, radiative or nonradiative (picoseconds to nanoseconds), competes with the electron transfer processes. Further, back electron transfer extinguishes the charge-separated states. Therefore, the singlet exciton states typically produce radical species less efficiently. However, the situation changes dramatically with dark exciton states, where back electron transfer is spin-forbidden, altering the reaction mechanism and allowing efficient charge separation, generating excited charge-separated (CS) states that persist for microseconds to milliseconds. The long-lived CS states, including QDs, biomolecules, and oxygen, drive progressive chemical reactions and biomolecular damage in PDT, and the regeneration of neutral QDs is key to its efficiency.

One PDT pathway for the radical species involves triggering a cascade of reactions with molecular oxygen, producing a variety of ROS, including the superoxide anion radical ($O_2\bullet^-$), hydroxyl radical (•OH), hydrogen peroxide (H_2O_2), and hydroperoxyl radical ($HO_2\bullet$). Among these ROS, •OH stands out as the most reactive and destructive, capable of inducing DNA fragmentation, protein cross-linking, lipid peroxidation, and ultimately cell death [323]. This makes the Type I mechanism particularly valuable for antimicrobial PDT, where such aggressive oxidative damage is desirable. Fig. 13 demonstrates the mechanism for ROS generation. For example, $CuInS_2$ QDs have demonstrated efficient ROS production *via* the Type-I mechanism, resulting in superior PDT effects in hypoxic tumor models compared to traditional porphyrin-based photosensitizers [321,324]. Similarly, ZnO NCs follow the Type I PDT pathway [325], efficiently generating •OH under visible-light irradiation, making them promising candidates for cancer and antimicrobial PDT.

In contrast, the Type II pathway is an entirely different mechanism in which energy transfer rather than electron transfer generates ROS. The key step involves long-lived triplet-like dark exciton states of NCs interacting with ground-state (triplet, $^3O_2$) molecular oxygen *via* triplet-triplet energy transfer (TTET), also known as Dexter energy transfer (DET). The excitation energy from the NCs transfers to $^3O_2$, translating it to one of the singlet excited states ($^1O_2$) [313,323], a potent natural or stimulated cytotoxic agent, capable of inducing severe oxidative damage to biomolecules, such as lipids, proteins, and nucleic acids, in cells and triggering apoptotic cell death.

Whether the PDT proceeds through Type I or Type II pathways, and the relative contributions of the two pathways, largely depend on the tumor microenvironment, where photochemistry and cell biology become active [326]. In hydrophobic environments such as plasma membranes or specific cellular compartments, the CS states generated through the Type I mechanism are poorly stabilized. However, the $^1O_2$ pathway becomes effective in such environments, where its extended lifetime allows it to diffuse over long distances and react efficiently with biomolecules. Therefore, the Type II mechanism predominates in hydrophobic regions of cell/tissue microenvironments. The situation reverses in the polar regions, such as the cytoplasm and extracellular spaces, where water and ionic solutes effectively quench $^1O_2$, drastically reducing its lifetime to less than 10 microseconds. Conversely, the CS states, or radical ions, are stabilized by solvation with polar molecules, making Type I pathways more favorable. This environmental sensitivity provides cells and tissues with a built-in site-specific spatio-temporal control over PDT [313,323].

Oxygen concentrations in cells and the tumor microenvironment play critical roles in PDT mechanisms. At high oxygen concentrations, dissolved oxygen efficiently quenches or accepts energy from the triplet-like states of semiconductor NPs through collisional encounter, favoring the Type II mechanism. Therefore, Type II PDT is favored in well-oxygenated normal cells and tissues. However, under hypoxic conditions, which are intrinsic to many solid tumors where oxygen levels can be 1% or lower, the collision-induced energy transfer from triplet-state NCs to oxygen becomes inefficient. Therefore, under hypoxic conditions, PDT preferentially directs photoexcited NCs to interact directly with biomolecules, generating radical species *via* the Type-II pathway, where oxygen availability plays no role.

Despite the origin of these mechanisms from the excited state processes and photochemical reactions based on molecular photosensitizers, the validity of the Type-II mechanism was demonstrated using CdSe and CdTe QDs, which effectively sensitize $^1O_2$ production *in vitro*, with appreciable yields measured using $^1O_2$ sensors, such as Singlet Oxygen Sensor Green (SOSG) and 1,3-diphenylisobenzofuran (DPBF) [316]. These early results expanded the scope of QDs for PDT, where Cd-free QDs such as Ag_2S, Ag_2Se, $AgInS_2$, $CuInS_2$, InP, and InAs help address toxicity concerns while maintaining PDT efficacy. *In vitro* PDT studies using these QDs confirm $^1O_2$ generation and apoptosis triggering in various cancer cell lines, including HeLa (cervical cancer) [327], A549 (lung cancer), and MCF-7 (breast cancer) [328,329], under visible or NIR photoactivation.

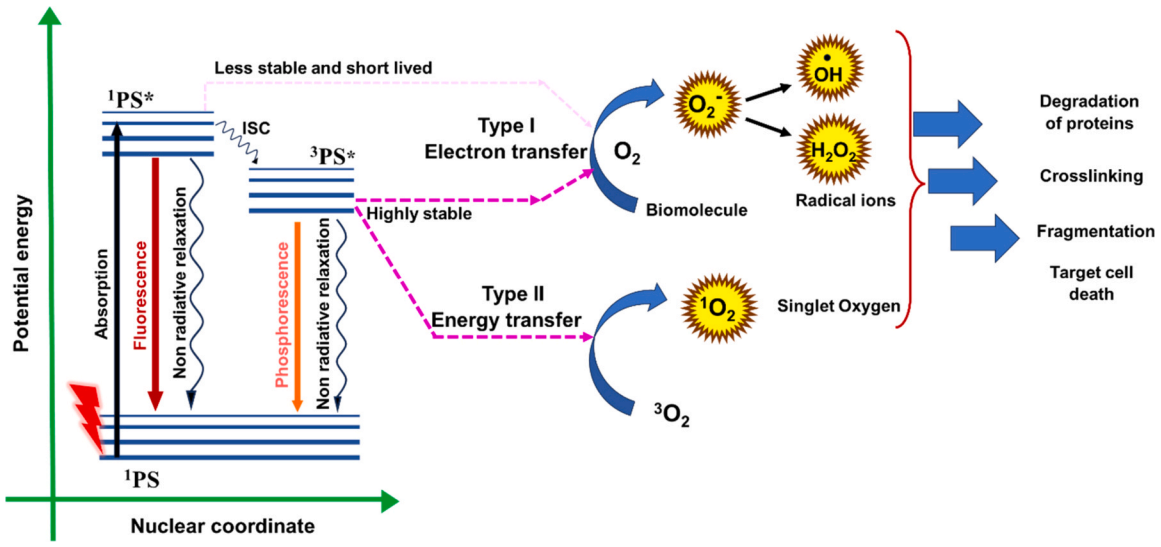

Fig. 13. The mechanism for ROS generation by Type I and II pathways.

Nevertheless, the TTET efficiencies of QD-based sensitizers are far below those of Pt- porphyrins and phthalocyanines. Several factors contribute to the low TTET, including quantum confinement, which alters the kinetics of triplet (dark-exciton) state formation, biexciton- and defect-assisted fast relaxation that competes with TTET rates, and weak spin-orbit coupling (SOC), which affects intersystem crossing to triplet states. This efficiency gap was a driving force in the development of QD-organic photosensitizer hybrid systems, in which the excellent light-harvesting antennae role of QDs has been utilized. Successive Förster Resonance Energy Transfer (FRET) from the QD to a photosensitizer not only enables efficient $^1O_2$ generation but also suppresses undesired photobleaching of the PS [323]. In this way, the advantage of FRET overcomes the limitations of DET. This pathway was demonstrated by Samia et al. in 2003 by preparing a CdSe QD-phthalocyanine FRET system for PDT in HeLa cells [317]. The attempt demonstrated the efficient utilization of the large absorption cross-section of QDs (10^{-14} cm^2, orders of magnitude larger than that of organic photosensitizers), enabling direct excitation of a photostable QD and indirect activation of a triplet sensitizer, paving the way for prolonged irradiation or repeated PDT. Since this seminal publication, QD-photosensitizer hybrid systems have expanded, demonstrating tunable excitation wavelength and NIR PDT. Such hybrid QD-photosensitizer systems are promising solutions to overcome the limitations of $^1O_2$ generation efficiency by QDs alone, offering synergistic platforms for imaging, PDT, and image-guided PDT that outperform the properties and applications of individual components.

Table 5 shows the efficiencies and the associated mechanisms of various QDs and NPs in producing ROS. As discussed above, ROS generation shows the photochemical interactions between photoexcited QDs or NPs and their environment, including solvent molecules, oxygen, and biomolecules. These interactions and the reactive species generated also affect the stability of QDs and NPs, metal ion release, and biological safety. The nanomaterial structure plays a crucial role in ROS generation. For example, unpassivated GaAs, GaSb, and HgSe core QDs/NPs generate reactive species that can be cytotoxic. However, silver-based QDs/NPs, such as Ag_2S QDs, have significantly lowered oxidative activity. Although high levels of ROS cause photodegradation, particularly in As-based materials, this characteristic can be advantageous for PDT for less toxic materials. Surface-passivated InP/ZnS and $CuInS_2$ QDs have been developed, which show $^1O_2$ QYs as high as 25%, comparable to those of conventional porphyrin- or phthalocyanine-based photosensitizers, where energy transfer produces $^1O_2$. By comparing the PLQY with the rates and mechanisms of energy or electron transfer across materials ranging from wide-bandgap to mid-infrared (MIR)-active, one can guide the selection of QDs/NPs for targeted therapeutic use. The cell-based and in vivo PDT applications of prominent examples are discussed below.

Table 5
Summary of ROS generation by various QDs and NPs.

QD or NP	ROS	Mechanism	Efficiency or Yield	Reference (s)
CdSe/CdS/ZnS	$^1O_2$	Type II	31%	[330]
CdSe/ZnS	$O_2^{\bullet-}$	Type I	35%	[331]
PbS/SiO_2	$^1O_2$, $^{\bullet}OH$, $O_2^{\bullet-}$	Type I/II	12–20%	[332]
Ag_2S	$O_2^{\bullet-}$	Type I	High	[333]
Ag_2S,ZIF	$^1O_2$, $^{\bullet}OH$	Type I/II	High	[334]
Ag_2Se	mtROS	Mitochondrial stress	High	[335]
InP/ZnS	mtROS	Type II	44.3%	[198]
InP/ZnSe	$O_2^{\bullet-}$	Type I	High	[201]
$CuInS_2$/ZnS	$^1O_2$, $O_2^{\bullet-}$	Type I/II	30–50%	[336]
$AgInS_2$/UCN	$^1O_2$, $^{\bullet}OH$, $O_2^{\bullet-}$	Type II	27% reduction in cell viability	[327]

5.2. Cell-based PDT

Over the past 25 years, many studies have shown that semiconductor QDs and NCs perform well in PDT at the cellular level. These investigations have aimed to clarify how ROS is generated, test its effectiveness across various cancer cell lines, and examine where in the cell these materials localize, which affects therapy outcomes.

The first evidence for ROS detection *in vitro* in QD-mediated PDT came from studies using chemical probes like dichlorodihydrofluorescein diacetate (DCFH-DA) and dihydroethidium (DHE), as well as singlet oxygen sensors such as SOSG and DPBF [337]. Later, CdTe QDs exposed to visible light produced significant $^1O_2$ yields, as shown by quenching studies with sodium azide. However, the inherent toxicity of Cd-based QDs led to the development of less toxic Cd-free QDs for biological applications.

Cd-free QD systems, such as Ag_2S, Ag_2Se, InP/ZnS, $CuInS_2$, and $AgInS_2$, have emerged as versatile platforms for biological applications. They can be classified based on their functional roles: (i) QDs used solely as PS for ROS generation, (ii) NIR imaging combined with PS for ROS

generation, (iii) PDT integrated with drug-mediated chemotherapy (DOX), and (iv) for PTT treatments. These QDs have demonstrated significant cell viability reductions in HeLa, MCF-7, HepG2, and 4T1 under specific light irradiation [327–329]. Notably, Type I ROS generation is dominant in QDs and maintains cytotoxicity under hypoxic conditions. Also, surface functionalization enhances tumor selectivity, biocompatibility, targeted delivery, and the therapeutic precision of QD-based PDT.

Acar and coworkers developed a multifunctional Ag_2S-based theranostic NCs system for colorectal cancer therapy. In this system, they conjugated Ag_2S QDs to the EGFR antibody cetuximab, which acts as a targeting ligand to enable selective binding to cells [338]. Additionally, the system was loaded with 5-aminolevulinic acid (ALA), a photosensitizer that generates ROS for PDT. They observed that cell viability decreased to 35–40%, and further to 15% upon conjugation with the chemotherapeutic agent 5-fluorouracil. Moreover, ALA-Ag_2S QDs with MnO_2 shell decompose H_2O_2 to O_2 for enhanced ROS production, especially •OH [339]. Fluorescence and 2',7'-Dichlorofuorescin diacetate (DCFH-DA) assays in breast cancer cells (SKBR3 and MDA-MB-231) demonstrated a significant decrease in cell viability to 5–10% under combined PDT and PTT treatments.

Ag_2S QDs functionalized with pillar[6]arene (CP6, as the host) and DOX (as the guest) formed a host-guest system, enabling synergistic chemo-PDT in MCF-7 cells [327,328]. Under 808 nm irradiation, the QDs generated $^1O_2$ by the altered electronic transmission, while the host-guest interface enabled selective and controlled release of DOX. MCF-7 cells treated with functionalized QDs exhibited low cell viability (8–10%), thereby synergistically enhancing ROS-mediated apoptosis and chemotherapeutic efficacy. Similarly, $NaYF_4$-Yb, Er-Ag_2S upconversion system demonstrated PDT activity under 975 nm excitation, where upconversion-induced FRET to Ag_2S [340]. The resulting ROS generation, confirmed by cellular assays and DPBF degradation, demonstrated strong NIR-triggered phototoxicity suitable for deep-tissue PDT applications.

Nann et al. studied the mechanism of $^1O_2$ production by the InP/ZnS QDs for PDT [341]. They used chlorin e6 (Ce6) as the PS and found that upon 660 nm excitation, the InP QDs absorb photons and transfer energy non-radiatively to the Ce6 molecule via FRET. The singlet excited state of Ce6 undergoes ISC to form a triplet excited state and transfers its energy to ground-state oxygen to produce $^1O_2$. *In vitro* studies in MDA-MB-231 breast cancer cells confirmed that the generated $^1O_2$ oxidized cellular components, damaged membranes, and mitochondria, causing cell death. Similarly, Ren et al. demonstrated that Ag-doped InP/ZnS QDs capped with MPA exhibited green-to-green-red emission under two-photon excitation and functioned as type-I PSs [342]. Doping with Ag introduces mid-gap states, which facilitate efficient charge separation and electron transfer (Type I mechanism), generating ROS such as superoxide and hydroxyl radicals under two-photon excitation, as confirmed by DCFH and HPF fluorescence assays. MTT cell viability tests using U251 human glioma cells revealed 80% cell death, even under hypoxic conditions. Hence, Ag-doped InP/ZnS QDs are efficient for deep-tissue NIR-activation, oxygen-independent ROS generation for PDT.

Cu-In-S (CIS) heterostructure nanorods conjugated with Ce6 and functionalized to HA exhibited dual PTT-PDT activity against cancer cells [343]. Under 808 nm irradiation, CIS nanorods acted as an efficient PTT agent, Ce6 served as a PS for ROS ($^1O_2$) generation, and HA enabled aqueous solubility and selective targeting of the CD44 receptor in overexpressing B16F1 cancer cells. Cell viability studies showed 15–20% viability following combined PTT-PDT treatments, confirming extensive apoptosis and necrosis. Similarly, $CuInS_2$/ZnS conjugated with porphyrin PS effectively generated $^1O_2$ under 630 nm excitation. $CuInS_2$/ZnS QDs conjugated with porphyrin demonstrated FRET-mediated energy transfer under 800 or 1300 nm excitation, promoting Type II ROS generation and reducing cell viability to 35–40% [344].

Maji et al. demonstrated $AgInS_2$-coated upconversion nanoparticles (UCNs) as photocatalysts for NIR-activated PDT of cancer cells [327]. The NaY_4:Yb^{3+}/Er^{3+} UCN core, capped with OA, absorbs 980 nm NIR light and transfers the energy non-radiatively to the $AgInS_2$ shell *via* luminescence resonance energy transfer (LRET). The $AgInS_2$ shell then acts as a photocatalyst, generating ROS through both Type I and II processes. In type I, the photoexcited $AgInS_2$ generates charge carriers, where the electrons interact with the oxygen to form superoxide radicals, and holes oxidize water to generate hydroxyl radicals. In type II, the photoexcited holes ($> +0.95$ eV) transfer energy directly to ground-state oxygen, thereby generating $^1O_2$. HeLa cancer cells treated with UCN-$AgInS_2$ NPs exhibited a 27% reduction in cell viability in the MTT assay. Live/dead cell staining with Calcein-AM and propidium iodide (Fig. 14) showed that HeLa cells treated with irradiated NPs exhibited strong red fluorescence, confirming that the PDT induced tumor cell death. Similar studies and observations have been found for Ag_2Se QDs.

Subsequently, $AgInS_2$-ZnS (ZAIS) NCs capped with MPA were synthesized, exhibiting tunable emission across the visible to NIR region. These NCs functioned as dual imaging-PDT agents [345]. Upon photoexcitation, ZAIS undergoes Type I and II pathways to produce superoxide, hydroxide radicals, and $^1O_2$, respectively. HeLa cells incubated with ZAIS NCs showed efficient cytoplasmic uptake and caused cell death, demonstrating PDT. Cell viability varies with dose and irradiation time, reaching a maximum of 11% with a cell death efficiency of 89%. Furthermore, MPA-capped AIS loaded with ALA showed enhanced intracellular accumulation of photo porphyrin IX (PpIX), a naturally occurring photosensitizer within the cells [346]. Under light irradiation (420 nm), PpIX absorbs photons, transfers energy to molecular oxygen, and produces $^1O_2$ by the Type II PDT mechanism. *In vitro* studies in HeLa cells showed apoptotic cell death and a 55–60% decrease in cell viability.

5.3. Small animal PDT models

While *in vitro* experiments provide mechanistic insights, *in vivo* animal models are crucial for validating the therapeutic potential of QDs in clinical conditions. Rodent xenograft tumor models have been widely used to assess the effectiveness, distribution, clearance, and toxicity associated with QD-mediated PDT and PTT.

Ag_2S QDs conjugated to HSA exhibited NIR-II fluorescence and photoacoustic imaging, enabling complete tumor ablation under NIR irradiation *via* the PTT effect. *In vivo* studies in 4T1-tumor-bearing mice showed that QDs showed prolonged circulation and substantial tumor accumulation [347]. Under 808 nm irradiation, the QDs generate strong hyperthermia and complete tumor ablation at higher doses. It shows gradual renal clearance with minimal toxicity. Bandgap-engineered Ag_2S QDs biomineralized with mussel-protein (MAP-AgP35) exhibit strong NIR-II fluorescence, high ROS (O_2•$^-$) generation, and ~59% PTT conversion efficiency under 808 nm excitation [348]. *In vivo* studies in melanoma-bearing mice reveal precise, localized tumor ablation by PTT. Similarly, intravenously administered Ag_2S/g-C_3N_4 NCs in tumor-bearing BALB/c nude mice exhibited preferential tumor accumulation by the EPR effect [349]. Under 808 nm NIR laser irradiation, the NCs activate synergistic PTT and PDT by producing Type II ROS (O_2•$^-$, •OH) and generating significant heat with a photothermal conversion efficiency of 31.28%, leading to apoptosis and complete tumor ablation [350]. Likewise, brominated hemicyanine-loaded and folate receptor-conjugated Ag_2S QDs enhance $^1O_2$ generation through enhanced spin-orbit coupling and serve as dual NIR fluorescence and photoacoustic imaging probes, enabling real-time tumor visualization and precise light-guided therapy. Ag_2S QDs with ZIF-90 form a core-shell structure, loaded with L-Arg and indocyanine green (ICG), which demonstrates PTT/PDT against periodontal biofilm [334,351]. At 808 nm, Ag_2S absorbs photons, raising the system temperature by 44.3 °C via PTT effects, whereas ICG generates $^1O_2$ from its triplet state for PDT. The combined PTT and PDT effects of Ag_2S QDs and ICG oxidize

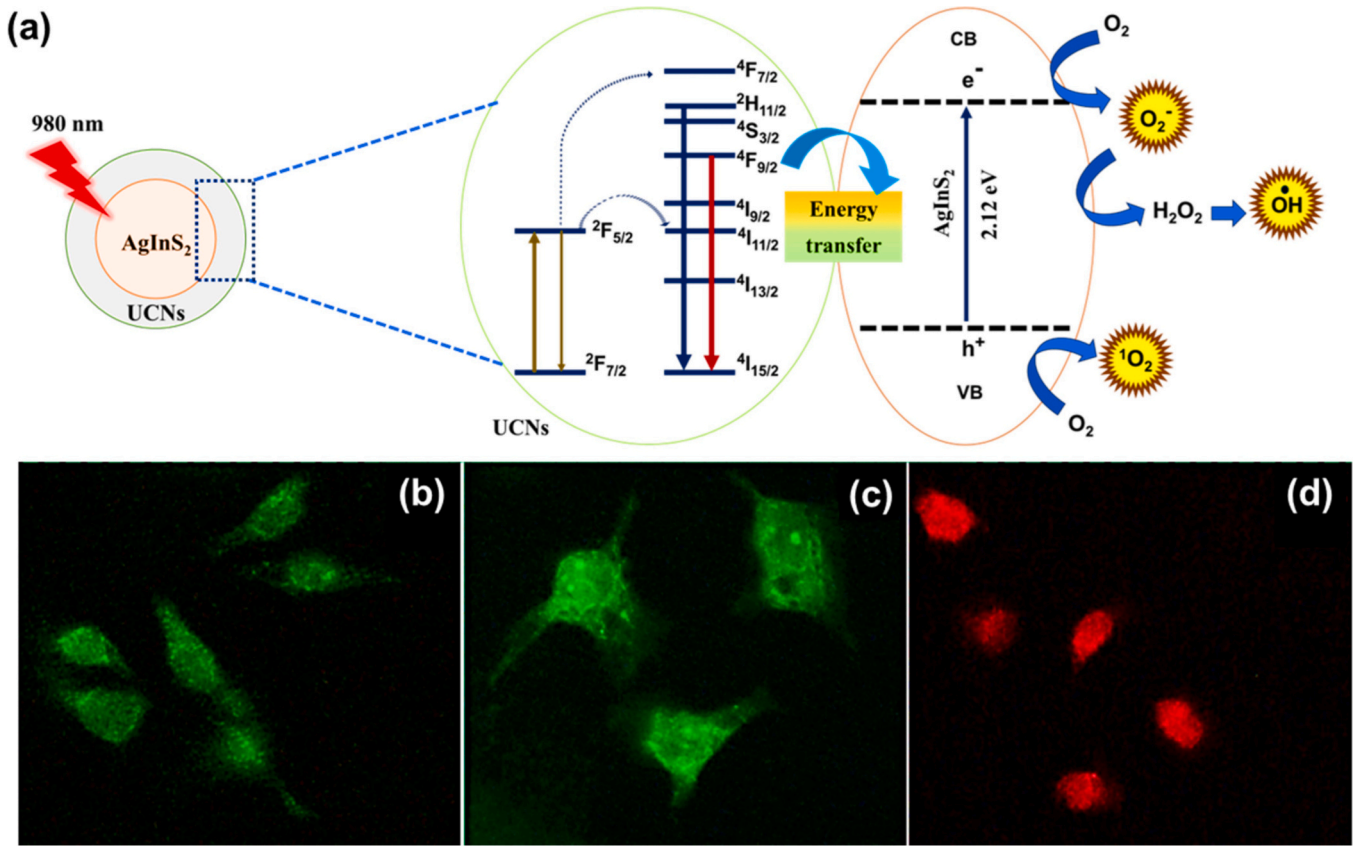

Fig. 14. (a) Scheme showing ROS generation through the energy transfer from UNSs to $AgInS_2$ NPs. (b-d) PDT in HeLa cells stained with Calcein AM (green fluorescence, live cell) and propidium iodide (red fluorescence, dead cell) (b) control, (c,d) cells treated with UCN-$AgInS_2$ NPs (c) under dark (d) under 980 nm irradiation. Reproduced with permission from (b-d) ref. [327]; copyright 2022, the American Chemical Society.

L-Arg, leading to NO production and a synergistic anti-inflammatory and antibacterial effect. *In vivo* studies in Wistar rats with periodontal inflammation showed that treatment with the nanocomposite effectively reduced bacterial counts, alleviated gingival inflammation, and restored periodontal health. Fig. 15 shows the scheme of NO production and *in vivo* treatment for periodontal inflammation.

Studies have shown that modification of PEGylated Ag_2S QDs with polydopamine (PDA) enhances their reactivity with ambient molecular oxygen, thereby generating ROS. 1,3-Diphenylisobenzofuran (DPBF) assay and triplet electron spin analysis proved the generation of $^1O_2$[352]. *In vivo* studies in 4T1 tumor-bearing female mice intratumorally injected with the QD system and irradiated at 808 nm resulted in reduced tumor size and complete tumor regression within 12 days. *In vivo* PDT and PTT effects have also been studied using Ag_2Se QDs, due to their strong NIR absorption, and incorporating UCNPs with QDs enables photostability and ROS generation. Song et al. used $NaYF_4$: $Yb^{3+}/Gd^{3+}/Er^{3+}$ and Ag_2Se system encapsulated with phosphatidylcholine to study PDT effects on 4T1 and lung carcinoma tumor-bearing mice [353]. They found that under 808 nm irradiation, energy transfer from QDs to Yb^{3+} occurs *via* a Type II mechanism, resulting in ROS formation. *In vivo* studies showed that both mouse models resulted in tumor tissue damage, cell apoptosis, and inhibition of further tumor growth and division. Similar studies have been reported by Du et al., who demonstrated a chitosan-Ag_2S QD system coated with $NaYF_4$: Yb/Er-$NaLuF_4$:Nd/Yb-$NaLuF_4$ (UCNPs) for photoacoustic multimodal imaging and PTT [354]. Under 808 nm irradiation, the nanocomposite

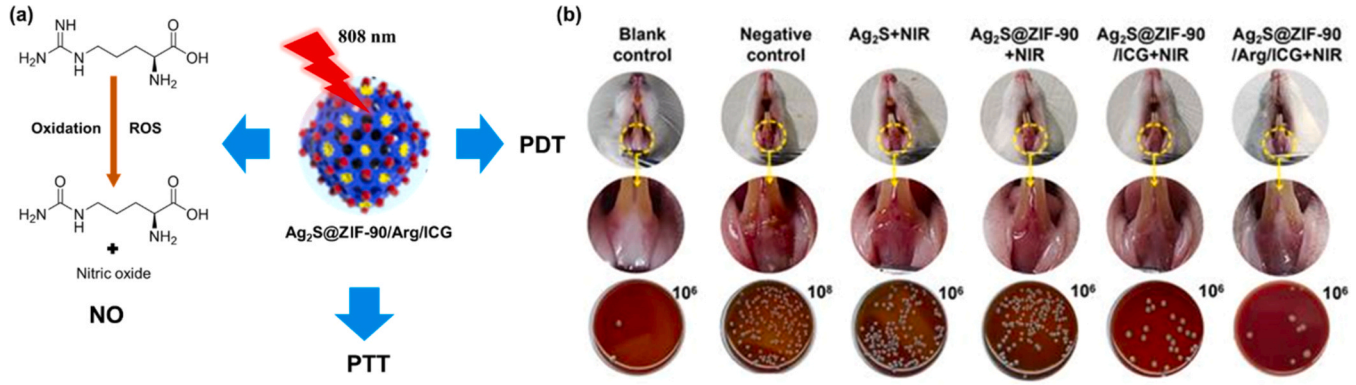

Fig. 15. (a) Scheme for PTT, PDT, and NO production from Ag_2S@ZIF-90/L-Arg/ICG nanocomposite. (b) Comparison of intraoral images and microbial colonies isolated from the gingival tissues treated with each nanocomposite. Reproduced with permission from (b) ref. [334]; copyright 2023, Ivyspring International.

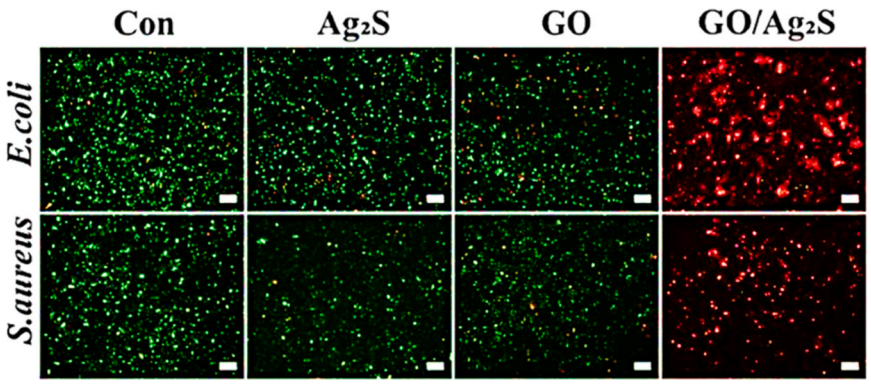

Fig. 16. Comparison of the antibacterial activity of the GO/Ag_2S system with control as the bacteria in PBS buffer, Ag_2S, and GO, under 808 nm irradiation. Reproduced with permission from ref. [358]. Copyright 2023, Elsevier Ltd.

raises the temperature to 59.3 °C, killing cancer cells and inhibiting proliferation. They also evaluated long-term toxicity and found that the nanocomposite is well metabolized and has negligible toxicity. Likewise, covalent organic frameworks with Ag_2Se QDs have been shown to be potential candidates for PDT and PTT agents [355]. A study by Shi and coworkers has introduced GO with TOP-capped $CuInS_2$/ZnS QDs delivered by PEGylated liposomes for treating cancerous cells [321]. This nanosystem, when intravenously injected into a tumor-bearing mouse, has shown a temperature increase to 48.9 °C under 671 nm irradiation. Both GO and $CuInS_2$/ZnS contributed significantly to PTT and cancer cell death. Moreover, under 671 nm irradiation, the rGO--$CuInS_2$/ZnS/liposome QDs generated 10-fold ROS when compared to only $CuInS_2$/ZnS QDs. *In vivo* studies have shown that all the tumors that were irradiated have significantly reduced their volume and disappeared within 18 days with minimal toxicity.

In conclusion, *in vivo* studies have demonstrated the efficacy of Cd-free QDs as promising PDT and PTT agents, with significant tumor suppression and complete recovery with minimal toxicity.

5.4. Antimicrobial PDT

Beyond oncology, semiconductor nanomaterials have shown great potential for antimicrobial PDT to combat antibiotic resistance and promote wound healing [322]. Biofilm disruption is perhaps the most difficult clinical issue. QDs can penetrate bacterial biofilms and induce ROS-mediated disruption, reducing biomass and colony-forming units by considerable amounts. In contrast to antibiotics, PDT is not dependent on specific metabolic pathways, and resistance is less likely to develop. In addition, QDs can be re-irradiated for repeated treatments. Carbon dots provide advantages in biocompatibility and clearance, whereas ZnO/TiO_2 NCs exhibit intensive radical-mediated killing.

The significant challenges in QD-based antimicrobial therapy include limited light penetration into deep host tissues, potential cytotoxicity to host tissues, and unknown long-term biosafety. Synthesis of QDs excitable with NIR, as well as targeted delivery to bacteria (*via* peptide or antibody conjugation), is actively pursued. Dong et al. demonstrated that Ag_2S-ZIF-90/Arg/ICG nanocomposite provided a synergistic therapeutic effect under 808 nm irradiation in a rat periodontitis model [334]. The nanocomposite exhibited PDT, PTT, and NO therapies, effectively eliminating deep-seated periodontal biofilms. This treatment significantly reduced gingival inflammation, decreased inflammatory cell infiltration, prevented collagen degradation in periodontal tissues, and improved periodontal tissue morphology. Similarly, photoactivated ZnO-Ag_2S core-shell nanostructures enable spatiotemporal synergy for osteomyelitis treatment in a mouse femur model [356]. It shows rapid bacterial eradication and biofilm disruption through ROS and PTT effects. Moreover, it also promotes bone healing and regeneration by controlled Zn^{2+} release from the ZnO core. Another study showed that a bilayer hydrogel composed of polypeptides ($AC_{10}A$ and $AC_{10}ARGD$) loaded with Ce6 and aptamer-conjugated Ag_2S QDs showed precise spatiotemporal antibacterial and anti-inflammatory control in osteomyelitis treatment [357]. Likewise, graphene oxide (GO)/Ag_2S nanosheets exhibited efficient antibacterial efficacy by their combined PDT and PTT, with controlled release of Ag^+ ions [358]. Under 808 nm irradiation, GO/Ag_2S heterostructure improves charge separation, resulting in both Type I and II ROS production, while the combined NIR absorption of GO and Ag_2S QDs enhances the PTT. The release of Ag^+ ions was substantially below the threshold, demonstrating minimal cytotoxicity. An antibacterial study in *Escherichia coli* and *Staphylococcus aureus* showed that the GO/Ag_2S system efficiently killed bacteria, achieving $>$ 99.9% efficacy under NIR irradiation (Fig. 16).

Vacancy-engineered Ag_2S NCs exhibited ~99% bactericidal efficiency against *Escherichia coli* and *Staphylococcus aureus* by inducing ROS through oxygen vacancy-mediated charge separation and enhanced electron transfer to adsorbed oxygen molecules [359]. The generated $O_2\bullet^-$, •OH radicals effectively disrupted the bacterial membranes, caused intracellular oxidative stress, and led to bacterial death. *In vivo* studies showed that wound infection in mice resulted in rapid healing and tissue regeneration. Incorporating Ag_2S QDs into a mesoporous silica-polymer hydrogel enabled a dual PDT-PTT process under 808 nm irradiation with controlled Ag^+ release [136]. The hydrogel achieved a high photothermal conversion efficiency of 57.3% and ROS-mediated hyperthermia, thereby accelerating wound healing. Furthermore, InP/ZnSe QDs have shown strong efficacy against infections caused by multidrug-resistant (MDR) bacteria [200]. InP/ZnSe QDs generated superoxide radicals by the Type I PDT mechanism under 400 nm LED irradiation. Murine subcutaneous abscess models demonstrated 99.83% bactericidal activity over 2 h, without inducing systemic toxicity. Similarly, PEGylated InP/ZnS QDs produced $O_2\bullet^-$ as the ROS by the Type I pathway under 660 nm irradiation [201]. These QDs, when introduced into mice with MDR bacterial infections, killed 90% of the bacteria, while cytotoxicity tests on mammalian cells showed 90% cell viability, demonstrating real-time abscess cure in mice.

6. Summary and outlook

Over the past quarter-century, semiconductor quantum dots have captivated researchers with their promise to revolutionize PDT, offering tunable optical properties and multifunctional capabilities that

traditional photosensitizers cannot match. The success has been marked by genuine scientific breakthroughs, including compelling evidence of both Type I and Type II photodynamic pathways, impressive tumor shrinkage in animal models, and notable antimicrobial effects, hinting at broader therapeutic potential. Yet, as with many transformative technologies, the path from the laboratory to clinical practice has proven far more complex than initially anticipated. The properties that made cadmium- and lead-based quantum dots attractive, with their brilliant PL and efficient ROS generation, have become their benchmark. Nevertheless, heavy metal toxicity looms large as a fundamental barrier to clinical translation. Even sophisticated surface passivation strategies cannot fully address the long-term pharmacokinetics of these NCs, which accumulate in the liver, spleen, and reticuloendothelial system, where degradation over time poses a risk of releasing toxic metal ions. Add to this the challenges of hypoxic tumor microenvironments that resist oxygen-dependent therapies, to understand the difficulties in achieving reproducible large-scale synthesis with consistent quality control, and to assess the magnitude of the challenge.

However, the lessons learned from these classic examples do not end in disappointment but rather pivot toward innovation and renewed hope. The field has undergone a paradigm shift, deliberately moving away from toxic heavy metals toward safer alternatives based on copper, silver, indium, and gallium, representing not merely incremental improvement but a fundamental advance in QD design strategy. These newer I-VI, III-V, and I-III-VI QDs are being engineered to retain the desirable absorption and emission characteristics of their predecessors while fundamentally addressing biocompatibility and environmental concerns. This evolution reflects a maturing field that has learned from early setbacks and is now building on a foundation of sophisticated bioconjugate chemistry, rigorous preclinical testing, and thoughtful consideration of pharmacokinetics and biodistribution. The integration of advanced surface modifications, targeted delivery strategies, and multifunctional platforms that combine imaging and therapy suggests we are approaching a tipping point at which QDs may finally fulfill their long-promised image-guided therapeutic potential.

While the narrow-bandgap QDs discussed in this review enable imaging, PDT, and image-guided PDT modalities, a range of wide-bandgap nanomaterials, including ZnO, TiO_2, carbon quantum dots (CQDs), carbon dots (CDs), and graphene quantum dots (GQDs), have also been extensively explored for PDT because of their biocompatibility, chemical stability, and ability to generate reactive oxygen species (ROS) through multiple mechanistic pathways. *In vivo* studies have demonstrated that CDs can effectively inhibit tumor growth in nude mice while being rapidly cleared from the body, thereby minimizing the risks associated with long-term toxicity [360,361]. Similarly, ZnO and TiO_2 NCs have been widely investigated for their PDT performance [325,362,363]. Under visible-light irradiation, ZnO efficiently generates hydroxyl radicals, thereby effectively eradicating drug-resistant bacteria and inducing apoptosis in cancer cells [363]. TiO_2 nanocrystals have also been shown to accelerate wound healing in mouse models, primarily due to their antimicrobial PDT activity [364,365]. Consequently, the rational combination of narrow-bandgap and wide-bandgap nanomaterials and QDs is expected to yield highly efficient PDT platforms while simultaneously offering advanced imaging capabilities. Nevertheless, the development of environmentally friendly nanomaterials, such as titanium nitride QDs [366], and the design of integrated therapeutic and imaging systems are expected to advance biomedical imaging, early disease detection, and therapeutic modalities.

Declaration of Competing Interest

The authors declare that they have no known competing financial interests or personal relationships that could have appeared to influence the work reported in this paper.

Acknowledgments

VB acknowledges the JSPS Grant-in-Aid for Scientific Research 23H01781, the Hokkaido University Photoexcitonix Program, and the 5 Star Crossover Alliance to Create the Future with People, Intelligence, and Materials. ESS acknowledges the support from the DST, ANRF, DBT and KSCSTE for a SR/PURSE/2023/191 grant, the PAIR program (2025/000021/PAIR-A), the quantum biotechnology grant (QTBT/176/32/2025) and an SRS grant (123/2025). SLA acknowledges a MEXT scholarship for doctoral studies.

Data availability

Figures used in the manuscript are linked to literature references. Reference numbers are given in the Figure captions. Also, links to the references are given in the reference section.

References

[1] A.M. Smith, H. Duan, A.M. Mohs, S. Nie, Bioconjugated quantum dots for in vivo molecular and cellular imaging, Adv. Drug Deliv. Rev. 60 (2008) 1226–1240, https://doi.org/10.1016/j.addr.2008.03.015.
[2] S.B. Rizvi, S. Ghaderi, M. Keshtgar, A.M. Seifalian, Semiconductor quantum dots as fluorescent probes for in vitro and in vivo bio-molecular and cellular imaging, Nano Rev. 1 (2010) 5161, https://doi.org/10.3402/nano.v1i0.5161.
[3] U. Resch-Genger, M. Grabolle, S. Cavaliere-Jaricot, R. Nitschke, T. Nann, Quantum dots versus organic dyes as fluorescent labels, Nat. Methods 5 (2008) 763–775, https://doi.org/10.1038/nmeth.1248.
[4] J. Zhang, R.E. Campbell, A.Y. Ting, R.Y. Tsien, Creating new fluorescent probes for cell biology, Nat. Rev. Mol. Cell Biol. 3 (2002) 906–918, https://doi.org/10.1038/nrm976.
[5] A.I. Ekimov, A.A. Onushchenko, Quantum size effects in three-dimensional microscopic semiconductor crystals, JEPT Lett. 34 (1981) 363–366, https://doi.org/10.1134/S0021364023130040.
[6] M.G. Bawendi, M.L. Steigerwald, L.E. Brus, The quantum mechanics of larger semiconductor clusters ("Quantum dots"), Annu Rev. Phys. Chem. 41 (1990) 477–496, https://doi.org/10.1146/annurev.pc.41.100190.002401.
[7] M. Nirmal, L. Brus, Luminescence photophysics in semiconductor nanocrystals, Acc. Chem. Res. 32 (1999) 407–414, https://doi.org/10.1021/ar9700320.
[8] D.F. Underwood, T. Kippeny, S.J. Rosenthal, Ultrafast carrier dynamics in CdSe nanocrystals determined by femtosecond fluorescence upconversion spectroscopy, J. Phys. Chem. B 105 (2001) 436–443, https://doi.org/10.1021/jp003088b.
[9] B. Xing, W. Li, H. Dou, P. Zhang, K. Sun, Systematic study of the properties of CdSe quantum dots synthesized in paraffin liquid with potential application in multiplexed bioassays, J. Phys. Chem. C 112 (2008) 14318–14323, https://doi.org/10.1021/jp8045577.
[10] A.L. Efros, M. Rosen, M. Kuno, M. Nirmal, D.J. Norris, M. Bawendi, Band-edge exciton in quantum dots of semiconductors with a degenerate valence band: dark and bright exciton states, Phys. Rev. B 54 (1996) 4843–4855, https://doi.org/10.1103/PhysRevB.54.4843.
[11] F.P. García de Arquer, D.V. Talapin, V.I. Klimov, Y. Arakawa, M. Bayer, E. H. Sargent, Semiconductor quantum dots: technological progress and future challenges, Science 373 (2021), https://doi.org/10.1126/science.aaz8541.
[12] S.M. Farkhani, A. Valizadeh, Review: Three synthesis methods of CdX (X = Se, S or Te) quantum dots, IET Nanobiotechnol. 8 (2014) 59–76, https://doi.org/10.1049/iet-nbt.2012.0028.
[13] C.R. Bullen, P. Mulvaney, Nucleation and growth kinetics of CdSe nanocrystals in octadecene, Nano Lett. 4 (2004) 2303–2307, https://doi.org/10.1021/nl0496724.
[14] Z.A. Peng, X. Peng, Formation of high-quality CdTe, CdSe, and CdS nanocrystals using CdO as precursor, J. Am. Chem. Soc. 123 (2001) 183–184, https://doi.org/10.1021/ja003633m.
[15] C.B. Murray, D.J. Norris, M.G. Bawendi, Synthesis and characterization of nearly monodisperse CdE (E = S, Se, Te) semiconductor nanocrystallites, J. Am. Chem. Soc. 115 (1993) 8706–8715, https://doi.org/10.1021/ja00072a025.
[16] J.E. Bowen Katari, V.L. Colvin, A.P. Alivisatos, X-ray photoelectron spectroscopy of CdSe nanocrystals with applications to studies of the nanocrystal surface, J. Phys. Chem. 98 (1994) 4109–4117, https://doi.org/10.1021/j100066a034.
[17] X. Peng, M.C. Schlamp, A.V. Kadavanich, A.P. Alivisatos, Epitaxial Growth of Highly Luminescent CdSe/CdS Core/Shell Nanocrystals with Photostability and Electronic Accessibility, J. Am. Chem. Soc. 119 (1997) 7019–7029, https://doi.org/10.1021/ja970754m.
[18] D.V. Talapin, R. Koeppe, S. Götzinger, A. Kornowski, J.M. Lupton, A.L. Rogach, O. Benson, J. Feldmann, H. Weller, Highly Emissive Colloidal CdSe/CdS Heterostructures of Mixed Dimensionality, Nano Lett. 3 (2003) 1677–1681, https://doi.org/10.1021/nl034815s.
[19] D.V. Talapin, I. Mekis, S. Götzinger, A. Kornowski, O. Benson, H. Weller, CdSe/CdS/ZnS and CdSe/ZnSe/ZnS core-shell-shell nanocrystals, J. Phys. Chem. B 108 (2004) 18826–18831, https://doi.org/10.1021/jp046481g.

[20] T. Vossmeyer, L. Katsikas, M. Giersig, I.G. Popovic, K. Diesner, A. Chemseddine, A. Eychmiuler, H. Weller, CdS Nanoclusters: Synthesis, Characterization, Size Dependent Oscillator Strength, Temperature Shift of the Excitonic Transition Energy, and Reversible Absorbance Shift, J. Phys. Chem. 98 (1994) 7665–7673, https://doi.org/10.1021/j100082a044.
[21] D. Deng, J. Xia, J. Cao, L. Qu, J. Tian, Z. Qian, Y. Gu, Z. Gu, Forming highly fluorescent near-infrared emitting PbS quantum dots in water using glutathione as surface-modifying molecule, J. Colloid Interface Sci. 367 (2012) 234–240, https://doi.org/10.1016/j.jcis.2011.09.043.
[22] J. Pichaandi, F.C.J.M. Van Veggel, Near-infrared emitting quantum dots: Recent progress on their synthesis and characterization, Coord. Chem. Rev. 263–264 (2014) 138–150, https://doi.org/10.1016/j.ccr.2013.10.011.
[23] J.E. Murphy, M.C. Beard, A.G. Norman, S.P. Ahrenkiel, J.C. Johnson, P. Yu, O. I. Mićić, R.J. Ellingson, A.J. Nozik, PbTe colloidal nanocrystals: synthesis, characterization, and multiple exciton generation, J. Am. Chem. Soc. 128 (2006) 3241–3247, https://doi.org/10.1021/ja0574973.
[24] H. Liu, J.S. Owen, A.P. Alivisatos, Mechanistic study of precursor evolution in colloidal group II-VI semiconductor nanocrystal synthesis, J. Am. Chem. Soc. 129 (2007) 305–312, https://doi.org/10.1021/ja0656696.
[25] S. Taniguchi, M. Green, S.B. Rizvi, A. Seifalian, The one-pot synthesis of core/shell/shell CdTe/CdSe/ZnSe quantum dots in aqueous media for in vivo deep tissue imaging, J. Mater. Chem. 21 (2011) 2877–2882, https://doi.org/10.1039/c0jm03527k.
[26] B.C. Fitzmorris, J.K. Cooper, J. Edberg, S. Gul, J. Guo, J.Z. Zhang, Synthesis and structural, optical, and dynamic properties of core/shell/shell CdSe/ZnSe/ZnS quantum dots, J. Phys. Chem. C. 116 (2012) 25065–25073, https://doi.org/10.1021/jp3092013.
[27] M. Grabolle, J. Ziegler, A. Merkulov, T. Nann, U. Resch-Genger, Stability and fluorescence quantum yield of CdSe-ZnS quantum dots - Influence of the thickness of the ZnS shell, Ann. N. Y Acad. Sci. 1130 (2008) 235–241, https://doi.org/10.1196/annals.1430.021.
[28] A.B. Greytak, P.M. Allen, W. Liu, J. Zhao, E.R. Young, Z. Popović, B.J. Walker, D. G. Nocera, M.G. Bawendi, Alternating layer addition approach to CdSe/CdS core/shell quantum dots with near-unity quantum yield and high on-time fractions, Chem. Sci. 3 (2012) 2028–2034, https://doi.org/10.1039/c2sc00561a.
[29] X. Liu, Y. Jiang, X. Lan, Y. Zhang, S. Li, J. Li, T. Han, B. Wang, H. Zhong, Highly luminescent blue emitting CdS/ZnS core/shell quantum dots via a single-molecular precursor for shell growth, Mater. Chem. Phys. 130 (2011) 909–914, https://doi.org/10.1016/j.matchemphys.2011.08.009.
[30] A.A. Marder, J. Cassidy, D. Harankahage, J. Beavon, L. Gutiérrez-Arzaluz, O. F. Mohammed, A. Mishra, A.C. Adams, J.D. Slinker, Z. Hu, S. Savoy, M. Zamkov, A.V. Malko, CdS/CdSe/CdS Spherical Quantum Wells with Near-Unity Biexciton Quantum Yield for Light-Emitting-Device Applications, ACS Mater. Lett. 5 (2023) 1411–1419, https://doi.org/10.1021/acsmaterialslett.3c00110.
[31] J. Wang, Y. Lu, F. Peng, Y. Zhong, Y. Zhou, X. Jiang, Y. Su, Y. He, Photostable water-dispersible NIR-emitting CdTe/CdS/ZnS core-shell-shell quantum dots for high-resolution tumor targeting, Biomaterials 34 (2013) 9509–9518, https://doi.org/10.1016/j.biomaterials.2013.09.005.
[32] R.C. Page, D. Espinobarro-Velazquez, M.A. Leontiadou, C. Smith, E.A. Lewis, S. J. Haigh, C. Li, H. Radtke, A. Pengpad, F. Bondino, E. Magnano, I. Pis, W. R. Flavell, P. O'Brien, D.J. Binks, Near-Unity Quantum Yields from Chloride Treated CdTe Colloidal Quantum Dots, Small 11 (2015) 1548–1554, https://doi.org/10.1002/smll.201402264.
[33] G. Shen, P. Guyot-Sionnest, HgS and HgS/CdS Colloidal Quantum Dots with Infrared Intraband Transitions and Emergence of a Surface Plasmon, J. Phys. Chem. C. 120 (2016) 11744–11753, https://doi.org/10.1021/acs.jpcc.6b04014.
[34] J. Yang, Y. Hu, J. Luo, Y.H. Zhu, J.S. Yu, Highly fluorescent, near-infrared-emitting Cd2+-Tuned HgS nanocrystals with optical applications, Langmuir 31 (2015) 3500–3509, https://doi.org/10.1021/la504879m.
[35] A. Kamath, R.D. Schaller, P. Guyot-Sionnest, Bright Fluorophores in the Second Near-Infrared Window: HgSe/CdSe Quantum Dots, J. Am. Chem. Soc. 145 (2023) 10809–10816, https://doi.org/10.1021/jacs.3c02190.
[36] W.H. Zhang, J. Yang, J.S. Yu, Synthesis of stable near-infrared emitting HgTe/CdS core/shell nanocrystals using dihydrolipoic acid as stabilizer, J. Mater. Chem. 22 (2012) 6383–6388, https://doi.org/10.1039/c2jm15630j.
[37] B. Coffey, E. Skytte, T. Ahmed, E.S. Vasileiadou, E.Y. Lin, A. Sueh Hua, E. Cook, S. M. Tenney, E.M. Sletten, J.R. Caram, Ultrasmall HgTe Quantum Dots with Near-Unity Photoluminescent Quantum Yields in the Near and Shortwave Infrared, Chem. Mater. 36 (2024) 7561–7569, https://doi.org/10.1021/acs.chemmater.4c01619.
[38] F. Ren, H. Zhao, F. Vetrone, D. Ma, Microwave-assisted cation exchange toward synthesis of near-infrared emitting PbS/CdS core/shell quantum dots with significantly improved quantum yields through a uniform growth path, Nanoscale 5 (2013) 7800–7804, https://doi.org/10.1039/c3nr02181e.
[39] Y. Zhang, Q. Dai, X. Li, Q. Cui, Z. Gu, B. Zou, Y. Wang, W.W. Yu, Formation of PbSe/CdSe Core/Shell nanocrystals for stable near-infrared high photoluminescence emission, Nanoscale Res. Lett. 5 (2010) 1279–1283, https://doi.org/10.1007/s11671-010-9637-7.
[40] A. Tubtimtae, K.L. Wu, H.Y. Tung, M.W. Lee, G.J. Wang, Ag2S quantum dot-sensitized solar cells, Electrochem. Commun. 12 (2010) 1158–1160, https://doi.org/10.1016/j.elecom.2010.06.006.
[41] D. Che, D. Ding, H. Wang, Q. Zhang, Y. Li, Aqueous synthesis of high bright Ag2Se-ZnSe quantum dots with tunable near-infrared emission, J. Alloy. Compd. 678 (2016) 51–56, https://doi.org/10.1016/j.jallcom.2016.03.172.
[42] H. Jin, R. Gui, J. Sun, Y. Wang, Glycerol-regulated facile synthesis and targeted cell imaging of highly luminescent Ag2Te quantum dots with tunable near-infrared emission, Colloids Surf. B Biointerfaces 143 (2016) 118–123, https://doi.org/10.1016/j.colsurfb.2016.03.030.
[43] H. Van Avermaet, P. Schiettecatte, S. Hinz, L. Giordano, F. Ferrari, C. Nayral, F. Delpech, J. Maultzsch, H. Lange, Z. Hens, Full-Spectrum InP-Based Quantum Dots with Near-Unity Photoluminescence Quantum Efficiency, ACS Nano 16 (2022) 9701–9712, https://doi.org/10.1021/acsnano.2c03138.
[44] R. Xie, K. Chen, X. Chen, X. Peng, InAs/InP/ZnSe core/shell/shell quantum dots as near-infrared emitters: Bright, narrow-band, non-cadmium containing, and biocompatible, Nano Res 1 (2008) 457–464, https://doi.org/10.1007/s12274-008-8048-x.
[45] R. Xie, M. Rutherford, X. Peng, Formation of high-quality I#III#VI semiconductor nanocrystals by tuning relative reactivity of cationic precursors, J. Am. Chem. Soc. 131 (2009) 5691–5697, https://doi.org/10.1021/ja9005767.
[46] M.R. Bergren, N.S. Makarov, K. Ramasamy, A. Jackson, R. Guglielmetti, H. McDaniel, High-Performance CuInS2 Quantum Dot Laminated Glass Luminescent Solar Concentrators for Windows, ACS Energy Lett. 3 (2018) 520–525, https://doi.org/10.1021/acsenergylett.7b01346.
[47] E. Cassette, T. Pons, C. Bouet, M. Helle, L. Bezdetnaya, F. Marchal, B. Dubertret, Synthesis and characterization of near-infrared Cu-In-Se/ZnS core/shell quantum dots for in vivo imaging, Chem. Mater. 22 (2010) 6117–6124, https://doi.org/10.1021/cm101881b.
[48] D.Y. Jo, D. Kim, J.H. Kim, H. Chae, H.J. Seo, Y.R. Do, H. Yang, Tunable White Fluorescent Copper Gallium Sulfide Quantum Dots Enabled by Mn Doping, ACS Appl. Mater. Interfaces 8 (2016) 12291–12297, https://doi.org/10.1021/acsami.6b01763.
[49] T. Torimoto, S. Ogawa, T. Adachi, T. Kameyama, K.I. Okazaki, T. Shibayama, A. Kudo, S. Kuwabata, Remarkable photoluminescence enhancement of ZnS-AgInS2 solid solution nanoparticles by post-synthesis treatment, Chem. Commun. 46 (2010) 2082–2084, https://doi.org/10.1039/b924186h.
[50] O.S. Oluwafemi, B.M.M. May, S. Parani, N. Tsolekile, Facile, large scale synthesis of water soluble AgInSe2/ZnSe quantum dots and its cell viability assessment on different cell lines, Mater. Sci. Eng. C 106 (2020), https://doi.org/10.1016/j.msec.2019.110181.
[51] V. Biju, T. Itoh, M. Ishikawa, Delivering quantum dots to cells: bioconjugated quantum dots for targeted and nonspecific extracellular and intracellular imaging, Chem. Soc. Rev. 39 (2010) 3031–3056, https://doi.org/10.1039/B926512K.
[52] Photoluminescence of CdSe and CdSe/ZnS quantum dots: modifications for making the invisible visible at ensemble and single-molecule levels, in: E.S. Shibu, M. Hamada, S. Nakanishi, S. Wakida, V. Biju (Eds.), Coord. Chem. Rev, 263, 2014, pp. 2–12, https://doi.org/10.1016/j.ccr.2013.10.014.
[53] V. Biju, S. Mundayoor, R.V. Omkumar, A. Anas, M. Ishikawa, Bioconjugated quantum dots for cancer research: present status, prospects and remaining issues, Biotechnol. Adv. 28 (2010) 199–213, https://doi.org/10.1016/j.biotechadv.2009.11.007.
[54] V. Biju, T. Itoh, A. Anas, A. Sujith, M. Ishikawa, Semiconductor quantum dots and metal nanoparticles: syntheses, optical properties, and biological applications, Anal. Bioanal. Chem. 391 (2008) 2469–2495, https://doi.org/10.1007/s00216-008-2185-7.
[55] J. Sobhanan, J.V. Rival, A. Anas, E.S. Shibu, Y. Takano, V. Biju, Luminescent quantum dots: Synthesis, optical properties, bioimaging and toxicity, Adv. Drug Deliv. Rev. 197 (2023) 114830, https://doi.org/10.1016/j.addr.2023.114830.
[56] J. Sobhanan, A. Anas, V. Biju, Nanomaterials for fluorescence and multimodal bioimaging, Chem. Rec. 23 (2023) e202200253, https://doi.org/10.1002/tcr.202200253.
[57] S. Wang, J. Yu, P. Zhao, S. Guo, S. Han, One-step synthesis of water-soluble CdS quantum dots for silver-ion detection, ACS Omega 6 (2021) 7139–7146, https://doi.org/10.1021/acsomega.1c00162.
[58] D. Zhou, M. Lin, Z. Chen, H. Sun, H. Zhang, H. Sun, B. Yang, Simple synthesis of highly luminescent water-soluble CdTe quantum dots with controllable surface functionality, Chem. Mater. 23 (2011) 4857–4862, https://doi.org/10.1021/cm202368w.
[59] I.L. Medintz, H. Tetsuo Uyeda, E.R. Goldman, H. Mattoussi, Quantum dot bioconjugates for imaging, labelling and sensing, Nat. Mater. 4 (2005) 435–446, https://doi.org/10.1038/nmat1390.
[60] D.J. Bharali, D.W. Lucey, H. Jayakumar, H.E. Pudavar, P.N. Prasad, Folate-receptor-mediated delivery of InP quantum dots for bioimaging using confocal and two-photon microscopy, J. Am. Chem. Soc. 127 (2005) 11364–11371, https://doi.org/10.1021/ja051455x.
[61] N. Gomez, J.O. Winter, F. Shieh, A.E. Saunders, B.A. Korgel, C.E. Schmidt, Challenges in quantum dot-neuron active interfacing, Talanta 67 (2005) 462–471, https://doi.org/10.1016/j.talanta.2005.06.041.
[62] L.S. Li, Z.Q. Zhang, Y. Zhang, Y.F. Liu, M.X. Zhao, Efficient drug delivery by polyethylenimine capped CdSe/ZnS quantum dots and their biological activity, Mater. Des. 220 (2022), https://doi.org/10.1016/j.matdes.2022.110890.
[63] A.L. Rogach, D. Nagesha, J.W. Ostrander, M. Giersig, N.A. Kotov, 'Raisin bun'-type composite spheres of silica and semiconductor nanocrystals, Chem. Mater. 12 (2000) 2676–2685, https://doi.org/10.1021/cm000244i.
[64] J.K. Jaiswal, H. Mattoussi, J.M. Mauro, S.M. Simon, Long-term multiple color imaging of live cells using quantum dot bioconjugates, Nat. Biotechnol. 21 (2003) 47–51, https://doi.org/10.1038/nbt767.
[65] H. Soo Choi, W. Liu, P. Misra, E. Tanaka, J.P. Zimmer, B. Itty Ipe, M.G. Bawendi, J.V. Frangioni, Renal clearance of quantum dots, Nat. Biotechnol. 25 (2007) 1165–1170, https://doi.org/10.1038/nbt1340.

[66] W. Liu, S.C. Hak, J.P. Zimmer, E. Tanaka, J.V. Frangioni, M. Bawendi, Compact cysteine-coated CdSe(ZnCdS) quantum dots for in vivo applications, J. Am. Chem. Soc. 129 (2007) 14530–14531, https://doi.org/10.1021/ja073790m.
[67] N. Gaponik, D.V. Talapin, A.L. Rogach, K. Hoppe, E.V. Shevchenko, A. Kornowski, A. Eychmüller, H. Weller, Thiol-capping of CDTe nanocrystals: an alternative to organometallic synthetic routes, J. Phys. Chem. B 106 (2002) 7177–7185, https://doi.org/10.1021/jp025541k.
[68] B. Ballou, B.C. Lagerholm, L.A. Ernst, M.P. Bruchez, A.S. Waggoner, Noninvasive imaging of quantum dots in mice, Bioconjug Chem. 15 (2004) 79–86, https://doi.org/10.1021/bc034153y.
[69] S.M. Rozenzhak, M.P. Kadakia, T.M. Caserta, T.R. Westbrook, M.O. Stone, R. R. Naik, Cellular internalization and targeting of semiconductor quantum dots, Chem. Commun. 17 (2005) 2217–2219, https://doi.org/10.1039/b418454h.
[70] A. Anas, T. Okuda, N. Kawashima, K. Nakayama, T. Itoh, M. Ishikawa, V. Biju, Clathrin-mediated endocytosis of quantum dot-peptide conjugates in living cells, ACS Nano 3 (2009) 2419–2429, https://doi.org/10.1021/nn900663r.
[71] X. Gao, Y. Cui, R.M. Levenson, L.W.K. Chung, S. Nie, In vivo cancer targeting and imaging with semiconductor quantum dots, Nat. Biotechnol. 22 (2004) 969–976, https://doi.org/10.1038/nbt994.
[72] L. Liu, K.T. Yong, I. Roy, W.C. Law, L. Ye, J. Liu, J. Liu, R. Kumar, X. Zhang, P. N. Prasad, Bioconjugated pluronic triblock-copolymer micelle-encapsulated quantum dots for targeted imaging of cancer: In vitro and in vivo studies, Theranostics 2 (2012) 705–713, https://doi.org/10.7150/thno.3456.
[73] M. Rafipoor, C. Schmidtke, C. Wolter, C. Strelow, H. Weller, H. Lange, Clustering of CdSe/CdS quantum dot/quantum rods into micelles can form bright, non-blinking, stable, and biocompatible probes, Langmuir 31 (2015) 9441–9447, https://doi.org/10.1021/acs.langmuir.5b01570.
[74] E.L. Bentzen, I.D. Tomlinson, J. Mason, P. Gresch, M.R. Warnement, D. Wright, E. Sanders-Bush, R. Blakely, S.J. Rosenthal, Surface modification to reduce nonspecific binding of quantum dots in live cell assays, Bioconjug. Chem. 16 (2005) 1488–1494, https://doi.org/10.1021/bc0502006.
[75] B. Ballou, L.A. Ernst, S. Andreko, T. Harper, J.A.J. Fitzpatrick, A.S. Waggoner, M. P. Bruchez, Sentinel lymph node imaging using quantum dots in mouse tumor models, Bioconjug. Chem. 18 (2007) 389–396, https://doi.org/10.1021/bc060261j.
[76] J.R. Slotkin, L. Chakrabarti, N.D. Hai, R.S.E. Carney, T. Hirata, B.S. Bregman, G. I. Gallicano, J.G. Corbin, T.F. Haydar, vivo quantum dot labeling of mammalian stem and progenitor cells, Dev. Dyn. 236 (2007) 3393–3401, https://doi.org/10.1002/dvdy.21235.
[77] M.A. Correa-Duarte, M. Giersig, L.M. Liz-Marzan, S. Spain, Stabilization of CdS semiconductor nanoparticles against photodegradation by a silica coating procedure, Chem. Phys. Lett. 286 (1998) 497–501, https://doi.org/10.1016/S0009-2614(98)00012-8.
[78] D. Gerion, F. Pinaud, S.C. Williams, W.J. Parak, D. Zanchet, S. Weiss, A. P. Alivisatos, Synthesis and properties of biocompatible water-soluble silica-coated CdSe/ZnS semiconductor quantum dots, J. Phys. Chem. B 105 (2001) 8861–8871, https://doi.org/10.1021/jp0105488.
[79] P. Mulvaney, L.M. Liz-Marzán, M. Giersig, T. Ung, Silica encapsulation of quantum dots and metal clusters, J. Mater. Chem. 10 (2000) 1259–1270, https://doi.org/10.1039/b000136h.
[80] T. Nann, P. Mulvaney, Single quantum dots in spherical silica particles, Angew. Chem. Int. Ed. 43 (2004) 5393–5396, https://doi.org/10.1002/anie.200460752.
[81] S.T. Selvan, T.T. Tan, J.Y. Ying, Robust, non-cytotoxic, silica-coated CdSe quantum dots with efficient photoluminescence, Adv. Mater. 17 (2005) 1620–1625, https://doi.org/10.1002/adma.200401960.
[82] P. Yang, S. Gai, J. Lin, Functionalized mesoporous silica materials for controlled drug delivery, Chem. Soc. Rev. 41 (2012) 3679–3698, https://doi.org/10.1039/c2cs15308d.
[83] X. Wu, H. Liu, J. Liu, K.N. Haley, J.A. Treadway, J.P. Larson, N. Ge, F. Peale, M. P. Bruchez, Immunofluorescent labeling of cancer marker Her2 and other cellular targets with semiconductor quantum dots, Nat. Biotechnol. 21 (2003) 41–46, https://doi.org/10.1038/nbt764.
[84] D.S. Lidke, P. Nagy, R. Heintzmann, D.J. Arndt-Jovin, J.N. Post, H.E. Grecco, E. A. Jares-Erijman, T.M. Jovin, Quantum dot ligands provide new insights into erbB/HER receptor-mediated signal transduction, Nat. Biotechnol. 22 (2004) 198–203, https://doi.org/10.1038/nbt929.
[85] E.S. Shibu, S. Sugino, K. Ono, H. Saito, A. Nishioka, S. Yamamura, M. Sawada, Y. Nosaka, V. Biju, Singlet-oxygen-sensitizing near-infrared-fluorescent multimodal nanoparticles, Angew. Chem. Int Ed. 52 (2013) 10559–10563, https://doi.org/10.1002/anie.201304264.
[86] V. Biju, M. Hamada, K. Ono, S. Sugino, T. Ohnishi, E.S. Shibu, S. Yamamura, M. Sawada, S. Nakanishi, Y. Shigeri, S.I. Wakida, Nanoparticles speckled by ready-to-conjugate lanthanide complexes for multimodal imaging, Nanoscale 7 (2015) 14829–14837, https://doi.org/10.1039/c5nr00959f.
[87] E.S. Shibu, K. Ono, S. Sugino, A. Nishioka, A. Yasuda, Y. Shigeri, S.I. Wakida, M. Sawada, V. Biju, Photouncaging nanoparticles for MRI and fluorescence imaging in vitro and in vivo, ACS Nano 7 (2013) 9851–9859, https://doi.org/10.1021/nn4043699.
[88] M.E. Åkerman, W.C.W. Chan, P. Laakkonen, S.N. Bhatia, E. Ruoslahti, Nanocrystal targeting in vivo, PNAS 99 (2002) 12617–12621, https://doi.org/10.1073/pnas.152463399.
[89] N. Bag, R. Mathur, F. Hussain, N. Indracanti, S. Singh, S. Singh, R.P. Chauhan, K. Chuttani, A.K. Mishra, Synthesis and in vivo toxicity assessment of CdSe:ZnS quantum dots functionalized with EDTA-Bis-Cysteamine, Toxicol. Res. (Camb.) 4 (2015) 1416–1425, https://doi.org/10.1039/c5tx00090d.
[90] P. Jones, S. Sugino, S. Yamamura, F. Lacy, V. Biju, Impairments of cells and genomic DNA by environmentally transformed engineered nanomaterials, Nanoscale 5 (2013) 9511–9516, https://doi.org/10.1039/C3NR03118G.
[91] J. Sobhanan, P. Jones, R. Kohara, S. Sugino, M. Vacha, C. Subrahmanyam, Y. Takano, F. Lacy, V. Biju, Toxicity of nanomaterials due to photochemical degradation and the release of heavy metal ions, Nanoscale 12 (2020) 22049–22058, https://doi.org/10.1039/D0NR03957H.
[92] J. Sobhanan, Y. Takano, S. Sugino, E. Hirata, S. Yamamura, V. Biju, Multimodal CTC detection using stem cell antigen-specific immunosilica particles and immunofluorescent quantum dots, NPG Asia Mater. 14 (2022) 3, https://doi.org/10.1038/s41427-021-00353-5.
[93] G. Xu, G. Lin, S. Lin, N. Wu, Y. Deng, G. Feng, Q. Chen, J. Qu, D. Chen, S. Chen, H. Niu, S. Mei, K.T. Yong, X. Wang, The Reproductive Toxicity of CdSe/ZnS Quantum Dots on the in vivo Ovarian Function and in vitro Fertilization, Sci. Rep. 6 (2016) 37677, https://doi.org/10.1038/srep37677.
[94] B. Gidwani, V. Sahu, S.S. Shukla, R. Pandey, V. Joshi, V.K. Jain, A. Vyas, Quantum dots: Prospectives, toxicity, advances and applications, J. Drug Deliv. Sci. Technol. 61 (2021) 102308, https://doi.org/10.1016/j.jddst.2020.102308.
[95] D. Wu, Y. Ma, Y. Cao, T. Zhang, Mitochondrial toxicity of nanomaterials, Sci. Total Environ. 702 (2020) 134994, https://doi.org/10.1016/j.scitotenv.2019.134994.
[96] D. Mo, L. Hu, G. Zeng, G. Chen, J. Wan, Z. Yu, Z. Huang, K. He, C. Zhang, M. Cheng, Cadmium-containing quantum dots: properties, applications, and toxicity, Appl. Microbiol Biotechnol. 101 (2017) 2713–2733, https://doi.org/10.1007/s00253-017-8140-9.
[97] C. Kirchner, T. Liedl, S. Kudera, T. Pellegrino, A.M. Javier, H.E. Gaub, S. Stölzle, N. Fertig, W.J. Parak, Cytotoxicity of colloidal CdSe and CdSe/ZnS nanoparticles, Nano Lett. 5 (2005) 331–338, https://doi.org/10.1021/nl047996m.
[98] K.C. Nguyen, P. Rippstein, A.F. Tayabali, W.G. Willmore, Mitochondrial toxicity of cadmium telluride quantum dot nanoparticles in mammalian hepatocytes, Toxicol. Sci. 146 (2015) 31–42, https://doi.org/10.1093/toxsci/kfv068.
[99] J.M. Shen, X.M. Guan, X.Y. Liu, J.F. Lan, T. Cheng, H.X. Zhang, Luminescent/magnetic hybrid nanoparticles with folate-conjugated peptide composites for tumor-targeted drug delivery, Bioconjug Chem. 23 (2012) 1010–1021, https://doi.org/10.1021/bc300008k.
[100] W.M. Girma, M.Z. Fahmi, A. Permadi, M.A. Abate, J.Y. Chang, Synthetic strategies and biomedical applications of I-III-VI ternary quantum dots, J. Mater. Chem. B 5 (2017) 6193–6216, https://doi.org/10.1039/c7tb01156c.
[101] W. Ge, G. Yu, Y. Jiang, H. Yu, F. Wang, NIR-II silver chalcogenide nanocrystals: synthesis, photophysical modulation and deep-tissue fluorescence imaging, Nanoscale (2026), https://doi.org/10.1039/d5nr04957a.
[102] Y. Zhao, M. Su, Z. Wu, W. Yang, Y. Du, Y. Pang, N. Li, Y. Li, B. Xing, J. Zhang, Z. Wang, Review of Second Near-Infrared Biosensing, Bioimaging, and Imaging-Guided Therapy with Quantum Dots, ACS Appl. Nano Mater. (2024), https://doi.org/10.1021/acsanm.4c04273.
[103] Y. Zhang, H. Yang, C. Li, G. Chen, J. Jiang, Q. Wang, NIR-II-Emitting Silver Chalcogenide Quantum Dots, Acc. Mater. Res. 7 (2026) 263–274, https://doi.org/10.1021/accountsmr.5c00300.
[104] C. Ding, Y. Huang, Z. Shen, X. Chen, Synthesis and Bioapplications of Ag2S Quantum Dots with Near-Infrared Fluorescence, Adv. Mater. 33 (2021), https://doi.org/10.1002/adma.202007768.
[105] M.C. Brelle, J.Z. Zhang, L. Nguyen, R.K. Mehra, Synthesis and ultrafast study of cysteine- and glutathione-capped Ag2S semiconductor colloidal nanoparticles, J. Phys. Chem. A 103 (1999) 10194–10201, https://doi.org/10.1021/jp991999j.
[106] L. Motte, F. Billoudet, E. Lacaze, J. Douin, M.P. Pileni, M. Curie, P. Vi, D. Diderot, Self-organization into 2d and 3d superlattices of nanosized particles differing by their size, J. Phys. Chem. B 101 (1997) 138–144, https://doi.org/10.1021/jp962398k.
[107] Y. Du, B. Xu, T. Fu, M. Cai, F. Li, Y. Zhang, Q. Wang, Near-infrared photoluminescent Ag2S quantum dots from a single source precursor, J. Am. Chem. Soc. 132 (2010) 1470–1471, https://doi.org/10.1021/ja909490r.
[108] C. Li, Y. Zhang, M. Wang, Y. Zhang, G. Chen, L. Li, D. Wu, Q. Wang, vivo real-time visualization of tissue blood flow and angiogenesis using Ag2S quantum dots in the NIR-II window, Biomaterials 35 (2014) 393–400, https://doi.org/10.1016/j.biomaterials.2013.10.010.
[109] Y. Zhang, G. Hong, Y. Zhang, G. Chen, F. Li, H. Dai, Q. Wang, Ag 2S quantum dot: A bright and biocompatible fluorescent nanoprobe in the second near-infrared window, ACS Nano 6 (2012) 3695–3702, https://doi.org/10.1021/nn301218z.
[110] C. Wang, Y. Wang, L. Xu, D. Zhang, M. Liu, X. Li, H. Sun, Q. Lin, B. Yang, Facile aqueous-phase synthesis of biocompatible and fluorescent Ag 2S nanoclusters for bioimaging: Tunable photoluminescence from red to near infrared, Small 8 (2012) 3137–3142, https://doi.org/10.1002/smll.201200376.
[111] G. Hong, J.T. Robinson, Y. Zhang, S. Diao, A.L. Antaris, Q. Wang, H. Dai, vivo fluorescence imaging with Ag2S quantum dots in the second near-infrared region, Angew. Chem. Int Ed. 51 (2012) 9818–9821, https://doi.org/10.1002/anie.201206059.
[112] H. Chen, B. Li, M. Zhang, K. Sun, Y. Wang, K. Peng, M. Ao, Y. Guo, Y. Gu, Characterization of tumor-targeting Ag2S quantum dots for cancer imaging and therapy in vivo, Nanoscale 6 (2014) 12580–12590, https://doi.org/10.1039/c4nr03613a.
[113] R. Tang, J. Xue, B. Xu, D. Shen, G.P. Sudlow, S. Achilefu, Tunable ultrasmall visible-to-extended near-infrared emitting silver sulfide quantum dots for integrin-targeted cancer imaging, ACS Nano 9 (2015) 220–230, https://doi.org/10.1021/nn5071183.
[114] Q. Wen, Y. Zhang, C. Li, S. Ling, X. Yang, G. Chen, Y. Yang, Q. Wang, NIR-II Fluorescent Self-Assembled Peptide Nanochain for Ultrasensitive Detection of

Peritoneal Metastasis, Angew. Chem. Int Ed. 131 (2019) 11117–11122, https://doi.org/10.1002/ange.201905643.
[115] C. Li, L. Cao, Y. Zhang, P. Yi, M. Wang, B. Tan, Z. Deng, D. Wu, Q. Wang, Preoperative Detection and Intraoperative Visualization of Brain Tumors for More Precise Surgery: A New Dual-Modality MRI and NIR Nanoprobe, Small 11 (2015) 4517–4525, https://doi.org/10.1002/smll.201500997.
[116] J.C. Hsu, D. Barragan, A.E. Tward, M. Hajfathalian, A. Amirshaghaghi, K. J. Mossburg, D.N. Rosario-Berríos, M. Bouché, A.K. Andrianov, E.J. Delikatny, D. P. Cormode, A Biodegradable "One-For-All" Nanoparticle for Multimodality Imaging and Enhanced Photothermal Treatment of Breast Cancer, Adv Healthc, Mater 13 (2024) 2303018, https://doi.org/10.1002/adhm.202303018.
[117] P. Awasthi, X. An, J. Xiang, N. Kalva, Y. Shen, C. Li, Facile synthesis of noncytotoxic PEGylated dendrimer encapsulated silver sulfide quantum dots for NIR-II biological imaging, Nanoscale 12 (2020) 5678–5684, https://doi.org/10.1039/c9nr10918h.
[118] Y. Du, M. Su, W. Yang, Z. Wu, Y. Zhao, T. Yan, N. Li, Y. Pang, Y. Li, H. Ma, Z. Wang, Y. Deng, J. Zhang, Acid-Resistant bioorthogonal quantum nanoprobes for noninvasive NIR-II imaging of simulated microgravity-induced gastric bacterial alterations in rats, Chem. Eng. J. 499 (2024) 155916, https://doi.org/10.1016/j.cej.2024.155916.
[119] T. Liu, X. Zhang, D. Liu, B. Chen, X. Ge, S. Gao, J. Song, Self-Assembled Ag2S-QD Vesicles for In Situ Responsive NIR-II Fluorescence Imaging-Guided Photothermal Cancer Therapy, Adv. Opt. Mater. 9 (2021) 2100233, https://doi.org/10.1002/adom.202100233.
[120] X. Cui, Z. Hu, R. Li, P. Jiang, Y. Wei, Z. Chen, CA IX-targeted Ag2S quantum dots bioprobe for NIR-II imaging-guided hypoxia tumor chemo-photothermal therapy, J. Pharm. Anal. 14 (2024) 100969, https://doi.org/10.1016/j.jpha.2024.100969.
[121] J.Y. Zhao, G. Chen, Y.P. Gu, R. Cui, Z.L. Zhang, Z.L. Yu, B. Tang, Y.F. Zhao, D. W. Pang, Ultrasmall Magnetically Engineered Ag2Se Quantum Dots for Instant Efficient Labeling and Whole-Body High-Resolution Multimodal Real-Time Tracking of Cell-Derived Microvesicles, J. Am. Chem. Soc. 138 (2016) 1893–1903, https://doi.org/10.1021/jacs.5b10340.
[122] G. Chen, F. Tian, C. Li, Y. Zhang, Z. Weng, Y. Zhang, R. Peng, Q. Wang, Invivo real-time visualization of mesenchymal stem cells tropism for cutaneous regeneration using NIR-II fluorescence imaging, Biomaterials 53 (2015) 265–273, https://doi.org/10.1016/j.biomaterials.2015.02.090.
[123] G. Chen, F. Tian, Y. Zhang, Y. Zhang, C. Li, Q. Wang, Tracking of transplanted human mesenchymal stem cells in living mice using near-infrared Ag2S quantum dots, Adv. Funct. Mater. 24 (2014) 2481–2488, https://doi.org/10.1002/adfm.201303263.
[124] C.N. Zhu, G. Chen, Z.Q. Tian, W. Wang, W.Q. Zhong, Z. Li, Z.L. Zhang, D.W. Pang, Near-Infrared Fluorescent Ag2Se–Cetuximab Nanoprobes for Targeted Imaging and Therapy of Cancer, Small 13 (2017), https://doi.org/10.1002/smll.201602309.
[125] C. Lv, T.Y. Zhang, Y. Lin, M. Tang, C.H. Zhai, H.F. Xia, J. Wang, Z.L. Zhang, Z. X. Xie, G. Chen, D.W. Pang, Transformation of Viral Light Particles into Near-Infrared Fluorescence Quantum Dot-Labeled Active Tumor-Targeting Nanovectors for Drug Delivery, Nano Lett. 19 (2019) 7035–7042, https://doi.org/10.1021/acs.nanolett.9b02483.
[126] Q. Ding, J. Zhao, H. Zhang, C. Li, M. Sun, C. Chen, H. Lin, C. Xu, H. Kuang, L. Xu, Enantiomeric NIR-II Emitting Rare-Earth-Doped Ag2Se Nanoparticles with Differentiated In Vivo Imaging Efficiencies, Angew. Chem. Int. Ed. 61 (2022), https://doi.org/10.1002/anie.202210370.
[127] B. Li, G. Wang, Y. Tong, Y. Zhang, S.K. Sun, C. Yu, Noninvasive Gastrointestinal Tract Imaging Using BSA-Ag2Te Quantum Dots as a CT/NIR-II Fluorescence Dual-Modal Imaging Probe in Vivo, ACS Biomater. Sci. Eng. 9 (2023) 449–457, https://doi.org/10.1021/acsbiomaterials.2c00886.
[128] J.J. Zhang, Y. Lin, H. Zhou, H. He, J.J. Ma, M.Y. Luo, Z.L. Zhang, D.W. Pang, Cell Membrane-Camouflaged NIR II Fluorescent Ag2Te, Quantum Dots-Based Nanobioprobes for Enhanced In Vivo Homotypic Tumor Imaging, Adv. Healthc, Mater 8 (2019), https://doi.org/10.1002/adhm.201900341.
[129] S. Ling, X. Yang, C. Li, Y. Zhang, H. Yang, G. Chen, Q. Wang, Tumor Microenvironment-Activated NIR-II Nanotheranostic System for Precise Diagnosis and Treatment of Peritoneal Metastasis, Angew. Chem. Int Ed. 59 (2020) 7219–7223, https://doi.org/10.1002/anie.202000947.
[130] H.D.A. Santos, D. Ruiz, G. Lifante, C. Jacinto, B.H. Juarez, D. Jaque, Time resolved spectroscopy of infrared emitting Ag2S nanocrystals for subcutaneous thermometry, Nanoscale 9 (2017) 2505–2513, https://doi.org/10.1039/c6nr08534b.
[131] C. Li, W. Li, H. Liu, Y. Zhang, G. Chen, Z. Li, Q. Wang, An Activatable NIR-II Nanoprobe for In Vivo Early Real-Time Diagnosis of Traumatic Brain Injury, Angew Chem Int{C}{C}{C}{C} {C}{C}{C}{C}Ed 132 (2020) 253–258. https://doi.org/10.1002/ange.201911803.
[132] H.D.A. Santos, I. Zabala Gutiérrez, Y. Shen, J. Lifante, E. Ximendes, M. Laurenti, D. Méndez-González, S. Melle, O.G. Calderón, E. López Cabarcos, N. Fernández, I. Chaves-Coira, D. Lucena-Agell, L. Monge, M.D. Mackenzie, J. Marqués-Hueso, C.M.S. Jones, C. Jacinto, B. del Rosal, A.K. Kar, J. Rubio-Retama, D. Jaque, Ultrafast photochemistry produces superbright short-wave infrared dots for low-dose in vivo imaging, Nat. Commun. 11 (2020), https://doi.org/10.1038/s41467-020-16333-2.
[133] X.L. Hou, X. Dai, J. Yang, B. Zhang, D.H. Zhao, C.Q. Li, Z.Y. Yin, Y. Di Zhao, B. Liu, Injectable polypeptide-engineered hydrogel depot for amplifying the anti-tumor immune effect induced by chemo-photothermal therapy, J. Mater. Chem. B 8 (2020) 8623–8633, https://doi.org/10.1039/d0tb01370f.
[134] T. Du, J. Liang, N. Dong, J. Lu, Y. Fu, L. Fang, S. Xiao, H. Han, Glutathione-Capped Ag2S Nanoclusters Inhibit Coronavirus Proliferation through Blockage of Viral RNA Synthesis and Budding, ACS Appl. Mater. Interfaces 10 (2018) 4369–4378, https://doi.org/10.1021/acsami.7b13811.
[135] P. Sun, K. Li, X. Liu, J. Wang, X. Qiu, W. Wei, J. Zhao, Peptide-mediated Aqueous Synthesis of NIR-II Emitting Ag2S Quantum Dots for Rapid Photocatalytic Bacteria Disinfection, Angew. Chem. Int Ed. 62 (2023), https://doi.org/10.1002/anie.202300085.
[136] T. Du, Z. Xiao, J. Cao, L. Wei, C. Li, J. Jiao, Z. Song, J. Liu, X. Du, S. Wang, NIR-activated multi-hit therapeutic Ag2S quantum dot-based hydrogel for healing of bacteria-infected wounds, Acta Biomater. 145 (2022) 88–105, https://doi.org/10.1016/j.actbio.2022.04.013.
[137] H. Wang, L. Yang, Y. Tan, W. Deng, Q. Xie, Ag2S quantum dots loaded dendritic mesoporous silica nanospheres as signal amplification labels for ultrasensitive electrochemical immuno-biosensor for Staphylococcus aureus, J. Electro Chem. 919 (2022) 116496, https://doi.org/10.1016/j.jelechem.2022.116496.
[138] Y. Huang, H. Geng, Z. Wu, L. Sun, C. Ji, C.A. Grimes, X. Feng, Q. Cai, An Ag2S@ZIF-Van nanosystem for NIR-II imaging of bacterial-induced inflammation and treatment of wound bacterial infection, Biomater. Sci. 10 (2022) 3972–3980, https://doi.org/10.1039/d2bm00550f.
[139] W. Wang, Y. Geng, Y. Qian, J. Mingrong, Y. Xie, A novel room temperature method to nanocrystalline Ag2Se, Mater. Res Bull. 34 (1999) 877–882, https://doi.org/10.1016/S0025-5408(99)00083-5.
[140] Y.J. Glanville, D.G. Narehood, P.E. Sokol, A. Amma, T. Mallouk, Preparation and synthesis of Ag2Se nanowires produced by template directed synthesis, J. Mater. Chem. 12 (2002) 2433–2434, https://doi.org/10.1039/b202913h.
[141] D.H. Son, S.M. Huges, Y. Yin, A.P. Alivisatos, Cation exchange reactions in ionic nanocrystals, Science 306 (2004) 1009–1012, https://doi.org/10.1126/science.1103755.
[142] D. Wang, T. Xie, Q. Peng, Y. Li, Ag, Ag2S, and Ag2Se nanocrystals: Synthesis, assembly, and construction of mesoporous structures, J. Am. Chem. Soc. 130 (2008) 4016–4022, https://doi.org/10.1021/ja710004h.
[143] Y.P. Gu, R. Cui, Z.L. Zhang, Z.X. Xie, D.W. Pang, Ultrasmall near-infrared Ag 2Se quantum dots with tunable fluorescence for in vivo imaging, J. Am. Chem. Soc. 134 (2012) 79–82, https://doi.org/10.1021/ja2089553.
[144] B. Dong, C. Li, G. Chen, Y. Zhang, Y. Zhang, M. Deng, Q. Wang, Facile synthesis of highly photoluminescent Ag2Se quantum dots as a new fluorescent probe in the second near-infrared window for in vivo imaging, Chem. Mater. 25 (2013) 2503–2509, https://doi.org/10.1021/cm400812v.
[145] C.N. Zhu, P. Jiang, Z.L. Zhang, D.L. Zhu, Z.Q. Tian, D.W. Pang, Ag2Se quantum dots with tunable emission in the second near-infrared window, ACS Appl. Mater. Interfaces 5 (2013) 1186–1189, https://doi.org/10.1021/am303110x.
[146] Z.L. Yu, W. Zhang, J.Y. Zhao, W.Q. Zhong, J.G. Ren, M. Wu, Z.L. Zhang, D. W. Pang, Y.F. Zhao, G. Chen, Development of a Dual-Modally Traceable Nanoplatform for Cancer Theranostics Using Natural Circulating Cell-Derived Microparticles in Oral Cancer Patients, Adv. Funct. Mater. 27 (2017), https://doi.org/10.1002/adfm.201703482.
[147] X.L. Ge, B. Huang, Z.L. Zhang, X. Liu, M. He, Z. Yu, B. Hu, R. Cui, X.J. Liang, D. W. Pang, Glucose-functionalized near-infrared Ag2Se quantum dots with renal excretion ability for long-term: In vivo tumor imaging, J. Mater. Chem. B 7 (2019) 5782–5788, https://doi.org/10.1039/c9tb01112a.
[148] L.L. Yang, W. Zhao, Z.Y. Liu, M. Ren, J. Kong, X. Zong, M.Y. Luo, B. Tang, J. Xie, D.W. Pang, A.A. Liu, Acid-Resistant Near-Infrared II Ag2Se Quantum Dots for Gastrointestinal Imaging, Anal. Chem. 95 (2023) 15540–15548, https://doi.org/10.1021/acs.analchem.3c01967.
[149] D.T. Schoen, C. Xie, Y. Cui, Electrical switching and phase transformation in silver selenide nanowires, J. Am. Chem. Soc. 129 (2007) 4116–4117, https://doi.org/10.1021/ja068365s.
[150] P. Boolchand, W.J. Bresser, Mobile silver ions and glass formation in solid electrolytes, Nature 410 (2001) 1070–1073, https://doi.org/10.1038/35074049.
[151] W.M. Lee, D.K. Shin, I.H. Kim, Thermoelectric and Transport Properties of YbzFe4−xNixSb12 Skutterudites, J. Electron Mater. 44 (2015) 1432–1437, https://doi.org/10.1007/s11664-014-3401-1.
[152] A. Sahu, L. Qi, M.S. Kang, D. Deng, D.J. Norris, Facile synthesis of silver chalcogenide (Ag2E; E = Se, S, Te) semiconductor nanocrystals, J. Am. Chem. Soc. 133 (2011) 6509–6512, https://doi.org/10.1021/ja200012e.
[153] D. Song, M. Zhu, C. Li, Y. Zhou, Y. Xie, Z. Li, Z. Liu, Boosting and Activating NIR-IIb Luminescence of Ag2Te Quantum Dots with a Molecular Trigger, Anal. Chem. 93 (2021) 16932–16939, https://doi.org/10.1021/acs.analchem.1c04164.
[154] Z.Y. Liu, A.A. Liu, H. Fu, Q.Y. Cheng, M.Y. Zhang, M.M. Pan, L.P. Liu, M.Y. Luo, B. Tang, W. Zhao, J. Kong, X. Shao, D.W. Pang, Breaking through the Size Control Dilemma of Silver Chalcogenide Quantum Dots via Trialkylphosphine-Induced Ripening: Leading to Ag2Te Emitting from 950 to 2100 nm, J. Am. Chem. Soc. 143 (2021) 12867–12877, https://doi.org/10.1021/jacs.1c06661.
[155] L.J. Shi, C.N. Zhu, H. He, D.L. Zhu, Z.L. Zhang, D.W. Pang, Z.Q. Tian, Near-infrared Ag2Se quantum dots with distinct absorption features and high fluorescence quantum yields, RSC Adv. 6 (2016) 38183–38186, https://doi.org/10.1039/c6ra04987g.
[156] X. Yang, H. Yang, T. Li, S. Ling, M. Li, Y. Zhang, F. Wu, S. Liu, C. Li, Q. Wang, Designable Nanoadaptor for Enhanced Recognition of Natural Killer Cell to Tumor via Bio-orthogonal Click Reaction, Nano Lett. 24 (2024) 7698–7705, https://doi.org/10.1021/acs.nanolett.4c01711.
[157] X. Yin, X. Li, C. Zhu, X. Lin, Z. Xie, Integration of fluorescence/photoacoustic imaging and targeted chemo/photothermal therapy with Ag2Se@BSA-RGD nanodots, N. J. Chem. 44 (2020) 4850–4857, https://doi.org/10.1039/d0nj00240b.
[158] X.H. Shi, Y.Y. Dai, L. Wang, Z.G. Wang, S.L. Liu, Water-Soluble High-Quality Ag2Te Quantum Dots Prepared by Mutual Adaptation of Synthesis and Surface

Modification for in Vivo Imaging, ACS Appl. Bio Mater. 4 (2021) 7692–7700, https://doi.org/10.1021/acsabm.1c00917.
[159] H. Tang, S.T. Yang, Y.F. Yang, D.M. Ke, J.H. Liu, X. Chen, H. Wang, Y. Liu, Blood Clearance, Distribution, Transformation, Excretion, and Toxicity of Near-Infrared Quantum Dots Ag2Se in Mice, ACS Appl. Mater. Interfaces 8 (2016) 17859–17869, https://doi.org/10.1021/acsami.6b05057.
[160] Y. Zhang, Y. Zhang, G. Hong, W. He, K. Zhou, K. Yang, F. Li, G. Chen, Z. Liu, H. Dai, Q. Wang, Biodistribution, pharmacokinetics and toxicology of Ag2S near-infrared quantum dots in mice, Biomaterials 34 (2013) 3639–3646, https://doi.org/10.1016/j.biomaterials.2013.01.089.
[161] X. Zeng, Y. Yuan, T. Wang, H. Wang, X. Hu, Z. Fu, G. Zhang, B. Liu, G. Lu, Targeted imaging and induction of apoptosis of drug-resistant hepatoma cells by miR-122-loaded graphene-InP nanocompounds, J. Nanobiotechnol 15 (2017), https://doi.org/10.1186/s12951-016-0237-2.
[162] Y.Z. Wu, J. Sun, Y. Zhang, M. Pu, G. Zhang, N. He, X. Zeng, Effective Integration of Targeted Tumor Imaging and Therapy Using Functionalized InP QDs with VEGFR2 Monoclonal Antibody and miR-92a Inhibitor, ACS Appl. Mater. Interfaces 9 (2017) 13068–13078, https://doi.org/10.1021/acsami.7b02641.
[163] Y. Wang, Y. Wang, G. Chen, Y. Li, W. Xu, S. Gong, Quantum-Dot-Based Theranostic Micelles Conjugated with an Anti-EGFR Nanobody for Triple-Negative Breast Cancer Therapy, ACS Appl. Mater. Interfaces 9 (2017) 30297–30305, https://doi.org/10.1021/acsami.7b05654.
[164] J. Gao, K. Chen, R. Luong, D.M. Bouley, H. Mao, T. Qiao, S.S. Gambhir, Z. Cheng, A novel clinically translatable fluorescent nanoparticle for targeted molecular imaging of tumors in living subjects, Nano Lett. 12 (2012) 281–286, https://doi.org/10.1021/nl203526f.
[165] J.P. Zimmer, S.W. Kim, S. Ohnishi, E. Tanaka, J.V. Frangioni, M.G. Bawendi, Size series of small indium arsenide-zinc selenide core-shell nanocrystals and their application to in vivo imaging, J. Am. Chem. Soc. 128 (2006) 2526–2527, https://doi.org/10.1021/ja0579816.
[166] D. Deng, Y. Chen, J. Cao, J. Tian, Z. Qian, S. Achilefu, Y. Gu, High-quality CuInS 2/ZnS quantum dots for in vitro and in vivo bioimaging, Chem. Mater. 24 (2012) 3029–3037, https://doi.org/10.1021/cm3015594.
[167] E.M. Kim, S.T. Lim, M.H. Sohn, H.J. Jeong, Facile synthesis of near-infrared CuInS2/ZnS quantum dots and glycol-chitosan coating for in vivo imaging, J. Nanopart. Res 19 (2017) 251, https://doi.org/10.1007/s11051-017-3944-1.
[168] Z. Liu, N. Chen, C. Dong, W. Li, W. Guo, H. Wang, S. Wang, J. Tan, Y. Tu, J. Chang, Facile Construction of Near Infrared Fluorescence Nanoprobe with Amphiphilic Protein-Polymer Bioconjugate for Targeted Cell Imaging, ACS Appl. Mater. Interfaces 7 (2015) 18997–19005, https://doi.org/10.1021/acsami.5b05406.
[169] W. Lian, D. Tu, P. Hu, X. Song, Z. Gong, T. Chen, J. Song, Z. Chen, X. Chen, Broadband excitable NIR-II luminescent nano-bioprobes based on CuInSe2 quantum dots for the detection of circulating tumor cells, Nano Today 35 (2020), https://doi.org/10.1016/j.nantod.2020.100943.
[170] X. Sun, M. Shi, C. Zhang, J. Yuan, M. Yin, S. Du, S. Yu, B. Ouyang, F. Xue, S. T. Yang, Fluorescent Ag-In-S/ZnS Quantum Dots for Tumor Drainage Lymph Node Imaging in Vivo, ACS Appl. Nano Mater. 4 (2021) 1029–1037, https://doi.org/10.1021/acsanm.0c02542.
[171] L. Liu, R. Hu, I. Roy, G. Lin, L. Ye, J.L. Reynolds, J. Liu, J. Liu, S.A. Schwartz, X. Zhang, K.T. Yong, Synthesis of luminescent near-infrared AgInS2 nanocrystals as optical probes for in vivo applications, Theranostics 3 (2013) 109–115, https://doi.org/10.7150/thno.5133.
[172] Y. Ogihara, H. Yukawa, T. Kameyama, H. Nishi, D. Onoshima, T. Ishikawa, T. Torimoto, Y. Baba, Labeling and in vivo visualization of transplanted adipose tissue-derived stem cells with safe cadmium-free aqueous ZnS coating of ZnS-AgInS 2 nanoparticles, Sci. Rep. 7 (2017), https://doi.org/10.1038/srep40047.
[173] D. Deng, L. Qu, Y. Gu, Near-infrared broadly emissive AgInSe2/ZnS quantum dots for biomedical optical imaging, J. Mater. Chem. C. Mater. 2 (2014) 7077–7085, https://doi.org/10.1039/c4tc01147c.
[174] A.K. Tan, N.A. Hamzah, M.A. Ahmad, S.S. Ng, Z. Hassan, Recent advances and challenges in the MOCVD growth of indium gallium nitride: A brief review, Mater. Sci. Semicond. Process 143 (2022), https://doi.org/10.1016/j.mssp.2022.106545.
[175] Z. Chen, Y. Li, C. Cao, S. Zhao, S. Fathololoumi, Z. Mi, X. Xu, Large-scale cubic InN nanocrystals by a combined solution- and vapor-phase method under silica confinement, J. Am. Chem. Soc. 134 (2012) 780–783, https://doi.org/10.1021/ja209072v.
[176] Y. Chen, N.T. Landes, D.J. Little, R. Beaulac, Conversion Mechanism of Soluble Alkylamide Precursors for the Synthesis of Colloidal Nitride Nanomaterials, J. Am. Chem. Soc. 140 (2018) 10421–10424, https://doi.org/10.1021/jacs.8b06063.
[177] J. Nagakubo, M. Hirakawa, T. Sawada, T. Nishihashi, K. Horita, H. Murakami, Solution Synthesis of High-Quality Indium-Nitride Quantum Dots, in: Dig Tech Pap, John Wiley and Sons Inc, 2018, pp. 28–31, https://doi.org/10.1002/SDTP.12483.
[178] D. Wen, N. Kirkwood, P. Mulvaney, Synthesis of Size-Tunable Indium Nitride Nanocrystals, J. Phys. Chem. Lett. 14 (2023) 3669–3676, https://doi.org/10.1021/acs.jpclett.3c00024.
[179] O.I. Micić, C.J. Curtis, K.M. Jones, J.R. Sprague, Synthesis-and-characterization-of-InP-quantum-dots, J. Phys. Chem. 98 (1994) 4966–4969, https://doi.org/10.1021/j100070a004.
[180] O.I. Micić, J.R. Sprague, C.J. Curtis, K.M. Jones, J.L. Machol, A.J. Nozik, H. Giessen, B. Fluegel, G. Mohs, N. Peyghambarian, Synthesis and Characterization of InP, GaP, and GaInP2 Quantum Dots, J. Phys. Chem. 99 (1995) 7754–7759, https://doi.org/10.1021/j100019a063.
[181] D. Battaglia, X. Peng, Formation of High Quality InP and InAs Nanocrystals in a Noncoordinating Solvent, Nano Lett. 2 (2002) 1027–1030, https://doi.org/10.1021/nl025687v.
[182] S. Adam, D.V. Talapin, H. Borchert, A. Lobo, C. McGinley, A.R.B. De Castro, M. Haase, H. Weller, T. Möller, The effect of nanocrystal surface structure on the luminescence properties: Photoemission study of HF-etched InP nanocrystals, J. Chem. Phys. 123 (2005), https://doi.org/10.1063/1.2004901.
[183] A.A. Guzelian, J.E.B. Katari, A.V. Kadavanich, U. Banin, K. Hamad, E. Juban, A. P. Alivisatos, R.H. Wolters, C.C. Arnold, J.R. Heath, Synthesis of size-selected, surface-passivated InP nanocrystals, J. Phys. Chem. 100 (1996) 7212–7219, https://doi.org/10.1021/jp953719f.
[184] S.R. Ankireddy, J. Kim, Selective detection of dopamine in the presence of ascorbic acid via fluorescence quenching of inp/zns quantum dots, Int J. Nanomed. 10 (2015) 113–119, https://doi.org/10.2147/IJN.S88388.
[185] A.M. Saeboe, A.Y. Nikiforov, R. Toufanian, J.C. Kays, M. Chern, J.P. Casas, K. Han, A. Piryatinski, D. Jones, A.M. Dennis, Extending the Near-Infrared Emission Range of Indium Phosphide Quantum Dots for Multiplexed in Vivo Imaging, Nano Lett. 21 (2021) 3271–3279, https://doi.org/10.1021/acs.nanolett.1c00600.
[186] S.M. Click, S.J. Rosenthal, Synthesis, Surface Chemistry, and Fluorescent Properties of InP Quantum Dots, Chem. Mater. 35 (2023) 822–836, https://doi.org/10.1021/acs.chemmater.2c03074.
[187] P.M. Allen, B.J. Walker, M.G. Bawendi, Mechanistic insights into the formation of InP quantum dots, Angew. Chem. Int Ed. 49 (2010) 760–762, https://doi.org/10.1002/anie.200905632.
[188] S. Tamang, C. Lincheneau, Y. Hermans, S. Jeong, P. Reiss, Chemistry of InP Nanocrystal Syntheses, Chem. Mater. 28 (2016) 2491–2506, https://doi.org/10.1021/acs.chemmater.5b05044.
[189] P. Ramasamy, K.J. Ko, J.W. Kang, J.S. Lee, Two-Step "seed-Mediated" Synthetic Approach to Colloidal Indium Phosphide Quantum Dots with High-Purity Photo- and Electroluminescence, Chem. Mater. 30 (2018) 3643–3647, https://doi.org/10.1021/acs.chemmater.8b02049.
[190] B.M. McMurtry, K. Qian, J.K. Teglasi, A.K. Swarnakar, J. De Roo, J.S. Owen, Continuous Nucleation and Size Dependent Growth Kinetics of Indium Phosphide Nanocrystals, Chem. Mater. 32 (2020) 4358–4368, https://doi.org/10.1021/acs.chemmater.0c01561.
[191] P. Roy, M. Virmani, P.P. Pillai, Blue-emitting InP quantum dots participate in an efficient resonance energy transfer process in water, Chem. Sci. 14 (2023) 5167–5176, https://doi.org/10.1039/d3sc00164d.
[192] D.Y. Jo, H.M. Kim, G.M. Park, D. Shin, Y. Kim, Y.H. Kim, C.W. Ryu, H. Yang, Unity quantum yield of InP/ZnSe/ZnS quantum dots enabled by Zn halide-derived hybrid shelling approach, Soft Sci. 4 (2024), https://doi.org/10.20517/ss.2024.19.
[193] Z. Cui, S. Qin, H. He, Z. Wen, D. Yang, Z. Piao, S. Mei, W. Zhang, R. Guo, Sequential Growth of InP Quantum Dots and Coordination between Interfacial Heterovalency and Shell Confinement: Implication for Light-Emitting Devices, ACS Appl. Nano Mater. 7 (2024) 1181–1190, https://doi.org/10.1021/acsanm.3c05167.
[194] Z. Cui, S. Qin, H. He, J. Zhao, R. Jiang, Y. Xing, S. Mei, W. Zhang, R. Guo, Efficient and environmentally friendly white light-emitting diodes with InP-based quantum dots embedded in mesoporous silica, J. Mater. Sci. Technol. 200 (2024) 104–111, https://doi.org/10.1016/j.jmst.2024.02.047.
[195] H.A. Nguyen, F.Y. Dou, N. Park, S. Wu, H. Sarsito, B. Diakubama, H. Larson, E. Nishiwaki, M. Homer, M. Cash, B.M. Cossairt, Predicting Indium Phosphide Quantum Dot Properties from Synthetic Procedures Using Machine Learning, Chem. Mater. 34 (2022) 6296–6311, https://doi.org/10.1021/acs.chemmater.2c00640.
[196] Z. Ranjbar-Navazi, M. Eskandani, M. Johari-Ahar, A. Nemati, H. Akbari, S. Davaran, Y. Omidi, Doxorubicin-conjugated D-glucosamine- and folate- bi-functionalised InP/ZnS quantum dots for cancer cells imaging and therapy, J. Drug Target 26 (2018) 267–277, https://doi.org/10.1080/1061186X.2017.1365876.
[197] L. Zhang, X.Q. Yang, J. An, S.D. Zhao, T.Y. Zhao, F. Tan, Y.C. Cao, Y. Di Zhao, vivo tumor active cancer targeting and CT-fluorescence dual-modal imaging with nanoprobe based on gold nanorods and InP/ZnS quantum dots, J. Mater. Chem. B 6 (2018) 2574–2583, https://doi.org/10.1039/c7tb02643a.
[198] S. Chen, Y. Chen, Y. Chen, Z. Yao, InP/ZnS quantum dots cause inflammatory response in macrophages through endoplasmic reticulum stress and oxidative stress, Int J. Nanomed. 14 (2019) 9577–9586, https://doi.org/10.2147/IJN.S218748.
[199] J. Gao, K. Chen, R. Xie, J. Xie, S. Lee, Z. Cheng, X. Peng, X. Chen, Ultrasmall near-infrared non-cadmium quantum dots for in vivo tumor imaging, Small 6 (2010) 256–261, https://doi.org/10.1002/smll.200901672.
[200] I. Lee, J. Moon, H. Lee, S. Koh, G.M. Kim, L. Gauthé, F. Stellacci, Y.S. Huh, P. Kim, D.C. Lee, Photodynamic treatment of multidrug-resistant bacterial infection using indium phosphide quantum dots, Biomater. Sci. 10 (2022) 7149–7161, https://doi.org/10.1039/d2bm01393b.
[201] C.R. McCollum, J.R. Bertram, P. Nagpal, A. Chatterjee, Photoactivated Indium Phosphide Quantum Dots Treat Multidrug-Resistant Bacterial Abscesses in Vivo, ACS Appl. Mater. Interfaces 13 (2021) 30404–30419, https://doi.org/10.1021/acsami.1c08306.
[202] E. Yaghini, H. Turner, A. Pilling, I. Naasani, A.J. MacRobert, vivo biodistribution and toxicology studies of cadmium-free indium-based quantum dot nanoparticles in a rat model, Nanomedicine 14 (2018) 2644–2655, https://doi.org/10.1016/j.nano.2018.07.009.

[203] E. Yaghini, E. Tacconi, A. Pilling, P. Rahman, J. Broughton, I. Naasani, M.R. S. Keshtgar, A.J. MacRobert, O. Della Pasqua, Population pharmacokinetic modelling of indium-based quantum dot nanoparticles: preclinical in vivo studies, Eur. J. Pharm. Sci. 157 (2021), https://doi.org/10.1016/j.ejps.2020.105639.
[204] G. Veronesi, M. Moros, H. Castillo-Michel, L. Mattera, G. Onorato, K.D. Wegner, W.L. Ling, P. Reiss, C. Tortiglione, Vivo Biotransformations of Indium Phosphide Quantum Dots Revealed by X-Ray Microspectroscopy, ACS Appl. Mater. Interfaces 11 (2019) 35630–35640, https://doi.org/10.1021/acsami.9b15433.
[205] M. Allocca, L. Mattera, A. Bauduin, B. Miedziak, M. Moros, L. De Trizio, A. Tino, P. Reiss, A. Ambrosone, C. Tortiglione, An Integrated Multilevel Analysis Profiling Biosafety and Toxicity Induced by Indium- and Cadmium-Based Quantum Dots in Vivo, Environ. Sci. Technol. 53 (2019) 3938–3947, https://doi.org/10.1021/acs.est.9b00373.
[206] V. Brunetti, H. Chibli, R. Fiammengo, A. Galeone, M.A. Malvindi, G. Vecchio, R. Cingolani, J.L. Nadeau, P.P. Pompa, InP/ZnS as a safer alternative to CdSe/ZnS core/shell quantum dots: In vitro and in vivo toxicity assessment, Nanoscale 5 (2013) 307–317, https://doi.org/10.1039/c2nr33024e.
[207] T. Sheikh, W.J. Mir, A. Alofi, M. Skoroterski, R. Zhou, S. Nematulloev, M. N. Hedhili, M. Ben Hassine, M.S. Khan, K.E. Yorov, B.E. Hasanov, H. Liao, Y. Yang, A. Shamim, M. Abulikemu, O.F. Mohammed, O.M. Bakr, Surface-Reconstructed InAs Colloidal Nanorod Quantum Dots for Efficient Deep-Shortwave Infrared Emission and Photodetection, J. Am. Chem. Soc. 146 (2024) 29094–29103, https://doi.org/10.1021/jacs.4c10755.
[208] H. Bahmani Jalali, L. De Trizio, L. Manna, F. Di Stasio, Indium arsenide quantum dots: an alternative to lead-based infrared emitting nanomaterials, Chem. Soc. Rev. 51 (2022) 9861–9881, https://doi.org/10.1039/d2cs00490a.
[209] R.L. Wells, C.G. Pitt, A.T. Mcphail, A.P. Purdy, S. Shafieezad, R.B. Hallock, The use of tris(trimethylsilyl)arsine to prepare gallium arsenide and indium arsenide, Chem. Mater. 1 (1989) 4–6, https://doi.org/10.1021/cm00001a002.
[210] R. Xie, K. Chen, X. Chen, X. Peng, InAs/InP/ZnSe core/shell/shell quantum dots as near-infrared emitters: Bright, narrow-band, non-cadmium containing, and biocompatible, Nano Res 1 (2008) 457–464, https://doi.org/10.1007/s12274-008-8048-x.
[211] D. Franke, D.K. Harris, O. Chen, O.T. Bruns, J.A. Carr, M.W.B. Wilson, M. G. Bawendi, Continuous injection synthesis of indium arsenide quantum dots emissive in the short-wavelength infrared, Nat. Commun. 7 (2016), https://doi.org/10.1038/ncomms12749.
[212] A.A. Guzelian, U. Banin, A.V. Kadavanich, X. Peng, A.P. Alivisatos, Colloidal chemical synthesis and characterization of InAs nanocrystal quantum dots, Appl. Phys. Lett. 69 (1996) 1432–1434, https://doi.org/10.1063/1.117605.
[213] M. Ginterseder, D. Franke, C.F. Perkinson, L. Wang, E.C. Hansen, M.G. Bawendi, Scalable Synthesis of InAs Quantum Dots Mediated through Indium Redox Chemistry, J. Am. Chem. Soc. 142 (2020) 4088–4092, https://doi.org/10.1021/jacs.9b12350.
[214] V. Srivastava, E. Dunietz, V. Kamysbayev, J.S. Anderson, D.V. Talapin, Monodisperse InAs Quantum Dots from Aminoarsine Precursors: Understanding the Role of Reducing Agent, Chem. Mater. 30 (2018) 3623–3627, https://doi.org/10.1021/acs.chemmater.8b01137.
[215] P.M. Allen, W. Liu, V.P. Chauhan, J. Lee, A.Y. Ting, D. Fukumura, R.K. Jain, M. G. Bawendi, InAs(ZnCdS) auantum dots optimized for biological imaging in the near-infrared, J. Am. Chem. Soc. 132 (2010) 470–471, https://doi.org/10.1021/ja908250r.
[216] O.T. Bruns, T.S. Bischof, D.K. Harris, D. Franke, Y. Shi, L. Riedemann, A. Bartelt, F.B. Jaworski, J.A. Carr, C.J. Rowlands, M.W.B. Wilson, O. Chen, H. Wei, G. W. Hwang, D.M. Montana, I. Coropceanu, O.B. Achorn, J. Kloepper, J. Heeren, P. T.C. So, D. Fukumura, K.F. Jensen, R.K. Jain, M.G. Bawendi, Next-generation in vivo optical imaging with short-wave infrared quantum dots, Nat. Biomed. Eng. 1 (2017), https://doi.org/10.1038/s41551-017-0056.
[217] S.W. Kim, J.P. Zimmer, S. Ohnishi, J.B. Tracy, J.V. Frangioni, M.G. Bawendi, Engineering InAsxP1-x/InP/ZnSe III-V alloyed core/shell quantum dots for the near-infrared, J. Am. Chem. Soc. 127 (2005) 10526–10532, https://doi.org/10.1021/ja0434331.
[218] J. Gao, K. Chen, R. Xie, J. Xie, Y. Yan, Z. Cheng, X. Peng, X. Chen, vivo tumor-targeted fluorescence imaging using near-infrared non-cadmium quantum dots, Bioconjug Chem. 21 (2010) 604–609, https://doi.org/10.1021/bc900323v.
[219] M. Omura, M. Hirata, A. Tanakaa, M. Zhao, Y. Makita, N. Inoue, K. Gotohb, N. Ishinishi, Testicular toxicity evaluation of arsenic-containing binary compound semiconductors, gallium arsenide and indium arsenide, in hamsters, Toxico Lett. 89 (1996) 123–129, https://doi.org/10.1016/S0378-4274(96)03796-4.
[220] M. Omura, K. Yamazaki, A. Tanaka, M. Hirata, Y. Makita, N. Inoue, Changes in the Testicular Damage Caused by Indium Arsenide and Indium Phosphide in Hamsters during Two Years after Intratracheal Instillations, J. Occup. Health 42 (2000) 196–204, https://doi.org/10.1539/joh.42.196.
[221] A. Tanaka, Toxicity of indium arsenide, gallium arsenide, and aluminium gallium arsenide, Toxicol. Appl. Pharm. 198 (2004) 405–411, https://doi.org/10.1016/j.taap.2003.10.019.
[222] W. Liu, A.Y. Chang, R.D. Schaller, D.V. Talapin, Colloidal InSb nanocrystals, J. Am. Chem. Soc. 134 (2012) 20258–20261, https://doi.org/10.1021/ja309821j.
[223] M. Yarema, M.V. Kovalenko, Colloidal synthesis of InSb nanocrystals with controlled polymorphism using indium and antimony amides, Chem. Mater. 25 (2013) 1788–1792, https://doi.org/10.1021/cm400320r.
[224] Q. Wang, C. Sun, Z. Liu, B. Zeng, Y. Chen, Z. Liu, H. You, X. Hu, P. Li, J. Zhang, X. Hou, N. Dai, Y. Li, Stepwise Crystallization Synthetic Strategy for Monodisperse InSb Colloidal Quantum Dots with Mid-Infrared Absorption, Angew. Chem. Int Ed. (2025), https://doi.org/10.1002/anie.202506387.
[225] W.J. Mir, T. Sheikh, S. Nematulloev, P. Maity, K.E. Yorov, A.H. Emwas, M. N. Hedhili, M.S. Khan, M. Abulikemu, O.F. Mohammed, O.M. Bakr, One-Pot Colloidal Synthesis Enables Highly Tunable InSb Short-Wave Infrared Quantum Dots Exhibiting Carrier Multiplication, Small 20 (2024), https://doi.org/10.1002/smll.202306535.
[226] Y. Kwon, O. Yeromina, M. Cavallo, M.G. Silly, D. Pierucci, E. Lhuillier, D. Aldakov, B. Hyot, P. Reiss, Synthesis of NIR/SWIR Absorbing InSb Nanocrystals Using Indium(I) Halide and Aminostibine Precursors, Adv. Funct. Mater. (2024), https://doi.org/10.1002/adfm.202403912.
[227] S. Chatterjee, K. Nemoto, H.T. Sun, N. Shirahata, Rational ligand design for enhanced carrier mobility in self-powered SWIR photodiodes based on colloidal InSb quantum dots, Nanoscale Horiz. 9 (2024) 817–827, https://doi.org/10.1039/d4nh00038b.
[228] C.M. Evans, S.L. Castro, J.J. Worman, R.P. Raffaelle, Synthesis and use of tris (trimethylsilyl)antimony for the preparation of InSb quantum dots, Chem. Mater. 20 (2008) 5727–5730, https://doi.org/10.1021/cm702856v.
[229] D.V. Krylsky, N.D. Zhukov, Synthesis, Composition, Photoluminescence, and Stability of Properties of Colloidal InSb-Based Quantum Dots, Tech. Phys. Lett. 45 (2019) 801–804, https://doi.org/10.1134/S106378501908025X.
[230] H. Seo, H.J. Eun, A.Y. Lee, H.K. Lee, J.H. Kim, S.W. Kim, Colloidal InSb Quantum Dots for 1500 nm SWIR Photodetector with Antioxidation of Surface, Adv. Sci. 11 (2024), https://doi.org/10.1002/advs.202306439.
[231] T.J. Goodwin, V.J. Leppert, S.H. Risbud, I.M. Kennedy, H.W.H. Lee, Synthesis of gallium nitride quantum dots through reactive laser ablation, Appl. Phys. Lett. 70 (1997) 3122–3124, https://doi.org/10.1063/1.119109.
[232] N.B. Uner, E. Thimsen, Nonequilibrium plasma aerotaxy of size controlled GaN nanocrystals, J. Phys. D. Appl. Phys. 53 (2020) 095201, https://doi.org/10.1088/1361-6463/ab59e6.
[233] F. Gyger, P. Bockstaller, H. Grager, D. Gerthsen, C. Feldmann, Quantum-confined GaN nanoparticles synthesized via liquid-ammonia-in-oil-microemulsions, Chem. Commun. 50 (2014) 2939–2942, https://doi.org/10.1039/c4cc00180j.
[234] H. Lu, C. Reese, S. Jeon, A. Sundar, Y. Fan, E. Rizzi, Y. Zhuo, L. Qi, R.S. Goldman, Mechanisms of GaN quantum dot formation during nitridation of Ga droplets, Appl. Phys. Lett. 116 (2020), https://doi.org/10.1063/1.5133965.
[235] D. Moher, G. Ren, D.M. Niedzwiedzki, R. Mishra, E. Thimsen, Photonic Properties of Thin Films Composed of Gallium Nitride Quantum Dots Synthesized by Nonequilibrium Plasma Aerotaxy, ACS Appl. Mater. Interfaces 16 (2024) 17927–17936, https://doi.org/10.1021/acsami.4c01909.
[236] K. Sardar, C.N.R. Rao, New Solvothermal Routes for GaN Nanocrystals, Adv. Mater. 16 (2004) 425–429, https://doi.org/10.1002/adma.200306050.
[237] G. Pan, M.E. Kordesch, P.G.Van Patten, Room-temperature synthesis of GaN nanopowder, Chem. Mater. 18 (2006) 5392–5394, https://doi.org/10.1021/cm060525b.
[238] F.A. Pizzarello, S. Ana, Method for the preparation of gallium phosphide, U.S Patent 3 (1963) 305,385. ⟨https://patents.google.com/patent/US3305385A/en⟩.
[239] S. Gao, J. Lu, Y. Zhao, N. Chen, Y. Xie, The growth process, stability of GaP nanocrystals and formation of Ga3P nanocrystals under solvothermal conditions in benzene, Eur. J. Inorg. Chem. (2003) 1822–1827, https://doi.org/10.1002/ejic.200200647.
[240] S. Kim, K. Lee, S. Kim, O.P. Kwon, J.H. Heo, S.H. Im, S. Jeong, D.C. Lee, S.W. Kim, Origin of photoluminescence from colloidal gallium phosphide nanocrystals synthesized via a hot-injection method, RSC Adv. 5 (2015) 2466–2469, https://doi.org/10.1039/c4ra10115d.
[241] W. Shi, K. Lin, X. Lin, Structural and optical characteristics of SiO2 thin film containing GaAs microcrystallites, J. Appl. Phys. 81 (1997) 2822–2824, https://doi.org/10.1063/1.363939.
[242] S.S. Kher, R.L. Wells, A Straightforward, New Method for the Synthesis of Nanocrystalline GaAs and GaP, Chem. Mater. 6 (1994) 2056–2062, https://doi.org/10.1021/cm00047a027.
[243] J.F. Janik, R.L. Wells, V.G. Young, A.L. Rheingold, I.A. Guzei, New Pnictinogallanes [H2 GaE(SiMe3)2]3 (E = P, As) Formation, Structural Characterization, and Thermal Decomposition to Afford Nanocrystalline GaP and GaAs, J. Am. Chem. Soc. 120 (1997) 532–537, https://doi.org/10.1021/ja9731837.
[244] C.K. Sun, G. Wang, J.E. Bowers, B. Brar, H.R. Blank, H. Kroemer, M.H. Pilkuhn, Optical investigations of the dynamic behavior of GaSb/GaAs quantum dots, Appl. Phys. Lett. 68 (1996) 1543–1545, https://doi.org/10.1063/1.115693.
[245] T. Kawazu, T. Noda, T. Mano, Y. Sakuma, H. Sakaki, Growth and optical properties of GaSb/GaAs type-II quantum dots with and without wetting layer, Jpn J. Appl. Phys. 54 (2015) 04DH01, https://doi.org/10.7567/JJAP.54.04DH01.
[246] R.L. Wells, E.E. Foos, P.S. White, A.L. Rheingold, L.M. Liable-Sands, Synthesis and Characterization of tert-Butylgallium-Antimony Compounds: X-ray Crystal Structures of t-Bu 3 Ga,Sb(SiMe 3) 3, [t-Bu 2 GaSb(SiMe 3) 2] 2, and t-Bu 2 GaSb (SiMe 3) 2 Ga(t-Bu) 2 Cl, the First Example of a Gallium-Antimony Mixed-Bridge Compound, Organometallics 16 (1997) 4771–4775, https://doi.org/10.1021/om9704915.
[247] J. Bae, Y. Shin, H. Yoo, Y. Choi, J. Lim, D. Jeon, I. Kim, M. Han, S. Lee, Quantum dot-integrated GaN light-emitting diodes with resolution beyond the retinal limit, Nat. Commun. 13 (2022), https://doi.org/10.1038/s41467-022-29538-4.
[248] F. Mollaamin, M. Monajjemi, Trapping of toxic heavy metals from water by GN–nanocage: Application of nanomaterials for contaminant removal technique, J. Mol. Struct. 1300 (2024), https://doi.org/10.1016/j.molstruc.2023.137214.
[249] S.A. Jewett, M.S. Makowski, B. Andrews, M.J. Manfra, A. Ivanisevic, Gallium nitride is biocompatible and non-toxic before and after functionalization with

peptides, Acta Biomater. 8 (2012) 728–733, https://doi.org/10.1016/j.actbio.2011.09.038.
[250] T.H. Young, C.R. Chen, Assessment of GaN chips for culturing cerebellar granule neurons, Biomaterials 27 (2006) 3361–3367, https://doi.org/10.1016/j.biomaterials.2006.02.001.
[251] T. Berthing, M. Lard, P.H. Danielsen, L. Abariute, K.K. Barfod, K. Adolfsson, K. B. Knudsen, H. Wolff, C.N. Prinz, U. Vogel, Pulmonary toxicity and translocation of gallium phosphide nanowires to secondary organs following pulmonary exposure in mice, J. Nanobiotechnology 21 (2023) 322, https://doi.org/10.1186/s12951-023-02049-0.
[252] C.E. Linsmeier, L. Wallman, L. Faxius, J. Schouenborg, L.M. Bjursten, N. Danielsen, Soft tissue reactions evoked by implanted gallium phosphide, Biomaterials 29 (2008) 4598–4604, https://doi.org/10.1016/j.biomaterials.2008.08.028.
[253] D.R. Webb, I.G. Sipes, D.E. Carter, I. Vitro, Vitro Solubility, in vivo toxicity of gallium arsenide WEBB, in vitro solubility and in viva toxicity of gallium arsenide, Toxicol. Appl. Pharm. 76 (1984) 96–104, https://doi.org/10.1016/0041-008X(84)90032-2.
[254] C.S. Ivanoff, A.E. Ivanoff, T.L. Hottel, Gallium poisoning: a rare case report, Food Chem. Toxicol. 50 (2012) 212–215, https://doi.org/10.1016/j.fct.2011.10.041.
[255] C.J. Boreiko, T.G. Rossman, Antimony and its compounds: Health impacts related to pulmonary toxicity, cancer, and genotoxicity, Toxicol. Appl. Pharm. 403 (2020), https://doi.org/10.1016/j.taap.2020.115156.
[256] J. Fujihara, N. Nishimoto, Dermal absorption of gallium antimonide in vitro and pro-inflammatory effects on human dermal fibroblasts, Toxicol. Vitr. 71 (2021), https://doi.org/10.1016/j.tiv.2020.105064.
[257] T. Torimoto, T. Kameyama, T. Uematsu, S. Kuwabata, Controlling optical properties and electronic energy structure of I–III–VI semiconductor quantum dots for improving their photofunctions, J. Photochem. Photo C Photochem. Rev. 54 (2023), https://doi.org/10.1016/j.jphotochemrev.2022.100569.
[258] R.C. Fitzmorris, R.P. Oleksak, Z. Zhou, B.D. Mangum, J.N. Kurtin, G.S. Herman, Structural and optical characterization of CuInS2 quantum dots synthesized by microwave-assisted continuous flow methods, J. Nanopart. Res 17 (2015) 319, https://doi.org/10.1007/s11051-015-3123-1.
[259] C. Coughlan, M. Ibáñez, O. Dobrozhan, A. Singh, A. Cabot, K.M. Ryan, Compound copper chalcogenide nanocrystals, Chem. Rev. 117 (2017) 5865–6109, https://doi.org/10.1021/acs.chemrev.6b00376.
[260] C. Xia, W. Wu, T. Yu, X. Xie, C. Van Oversteeg, H.C. Gerritsen, C. De Mello Donega, Size-dependent band-gap and molar absorption coefficients of colloidal CuInS2 quantum dots, ACS Nano 12 (2018) 8350–8361, https://doi.org/10.1021/acsnano.8b03641.
[261] E.S. Speranskaya, C. Sevrin, S. De Saeger, Z. Hens, I.Y. Goryacheva, C. Grandfils, Synthesis of Hydrophilic CuInS2/ZnS Quantum Dots with Different Polymeric Shells and Study of Their Cytotoxicity and Hemocompatibility, ACS Appl. Mater. Interfaces 8 (2016) 7613–7622, https://doi.org/10.1021/acsami.5b11258.
[262] L. Li, A. Pandey, D.J. Werder, B.P. Khanal, J.M. Pietryga, V.I. Klimov, Efficient synthesis of highly luminescent copper indium sulfide-based core/shell nanocrystals with surprisingly long-lived emission, J. Am. Chem. Soc. 133 (2011) 1176–1179, https://doi.org/10.1021/ja108261h.
[263] T. Omata, K. Nose, S. Otsuka-Yao-Matsuo, Size dependent optical band gap of ternary I-III-VI2 semiconductor nanocrystals, J. Appl. Phys. 105 (2009) 073106, https://doi.org/10.1063/1.3103768.
[264] M. Booth, A.P. Brown, S.D. Evans, K. Critchley, Determining the concentration of CuInS 2 quantum dots from the size-dependent molar extinction coefficient, Chem. Mater. 24 (2012) 2064–2070, https://doi.org/10.1021/cm300227b.
[265] J. Park, C. Dvoracek, K.H. Lee, J.F. Galloway, H.E.C. Bhang, M.G. Pomper, P. C. Searson, CuInSe/ZnS core/shell NIR quantum dots for biomedical imaging, Small 7 (2011) 3148–3152, https://doi.org/10.1002/smll.201101558.
[266] C. Zhao, Z. Bai, X. Liu, Y. Zhang, B. Zou, H. Zhong, Small GSH-Capped CuInS2 Quantum Dots: MPA-Assisted Aqueous Phase Transfer and Bioimaging Applications, ACS Appl. Mater. Interfaces 7 (2015) 17623–17629, https://doi.org/10.1021/acsami.5b05503.
[267] E.S. Speranskaya, N.V. Beloglazova, S. Abé, T. Aubert, P.F. Smet, D. Poelman, I. Y. Goryacheva, S. De Saeger, Z. Hens, Hydrophilic, bright CuInS2quantum dots as cd-free fluorescent labels in quantitative immunoassay, Langmuir 30 (2014) 7567–7575, https://doi.org/10.1021/la501268b.
[268] S. Mallick, P. Kumar, A.L. Koner, Freeze-Resistant Cadmium-Free Quantum Dots for Live-Cell Imaging, ACS Appl. Nano Mater. 2 (2019) 661–666, https://doi.org/10.1021/acsanm.8b02231.
[269] K. Nose, T. Omata, O.Y.M. Shinya, Colloidal synthesis of ternary copper indium diselenide quantum dots and their optical properties, J. Phys. Chem. C. 113 (2009) 3455–3460, https://doi.org/10.1021/jp809398k.
[270] P.M. Allen, M.G. Bawendi, Ternary I-III-VI quantum dots luminescent in the red to near-infrared, J. Am. Chem. Soc. 130 (2008) 9240–9241, https://doi.org/10.1021/ja8036349.
[271] S. Kim, M. Kang, S. Kim, J.H. Heo, J.H. Noh, S.H. Im, S. Il Seok, S.W. Kim, Fabrication of CuInTe2 and CuInTe2-xSe xternary gradient quantum dots and their application to solar cells, ACS Nano 7 (2013) 4756–4763, https://doi.org/10.1021/nn401274e.
[272] O. Yarema, M. Yarema, W.M.M. Lin, V. Wood, Cu-In-Te and Ag-In-Te colloidal nanocrystals with tunable composition and size, Chem. Commun. 52 (2016) 10878–10881, https://doi.org/10.1039/c6cc05571k.
[273] M.G. Panthani, T.A. Khan, D.K. Reid, D.J. Hellebusch, M.R. Rasch, J.A. Maynard, B.A. Korgel, vivo whole animal fluorescence imaging of a microparticle-based oral vaccine containing (CuInSexS2- x)/ZnS core/shell quantum dots, Nano Lett. 13 (2013) 4294–4298, https://doi.org/10.1021/nl402054w.
[274] X. Gao, X. Liu, Z. Lin, S. Liu, X. Su, CuInS2 quantum dots as a near-infrared fluorescent probe for detecting thrombin in human serum, Analyst 137 (2012) 5620–5624, https://doi.org/10.1039/c2an35888c.
[275] L.C. Spangler, R. Chu, L. Lu, C.J. Kiely, B.W. Berger, S. McIntosh, Enzymatic biomineralization of biocompatible CuInS2, (CuInZn)S2 and CuInS2/ZnS core/shell nanocrystals for bioimaging, Nanoscale 9 (2017) 9340–9351, https://doi.org/10.1039/c7nr02852k.
[276] X. An, Y. Zhang, J. Wang, D.M. Kong, X.W. He, L. Chen, Y. Zhang, The preparation of CuInS2-ZnS-Glutathione quantum dots and their application on the sensitive determination of cytochrome c and imaging of hela cells, ACS Omega 6 (2021) 17501–17509, https://doi.org/10.1021/acsomega.1c01983.
[277] Y. Xi, J. Yang, Y. Ge, S. Zhao, J. Wang, Y. Li, Y. Hao, J. Chen, Y. Zhu, One-pot synthesis of water-soluble near-infrared fluorescence RNase A capped CuInS2 quantum dots for: In vivo imaging, RSC Adv. 7 (2017) 50949–50954, https://doi.org/10.1039/c7ra08418h.
[278] C.W. Chen, D.Y. Wu, Y.C. Chan, C.C. Lin, P.H. Chung, M. Hsiao, R.S. Liu, Evaluations of the chemical stability and cytotoxicity of CuInS2 and CuInS2/ZnS core/shell quantum dots, J. Phys. Chem. C. 119 (2015) 2852–2860, https://doi.org/10.1021/jp510908f.
[279] M.F. Foda, L. Huang, F. Shao, H.Y. Han, Biocompatible and highly luminescent near-infrared CuInS2/ZnS quantum dots embedded silica beads for cancer cell imaging, ACS Appl. Mater. Interfaces 6 (2014) 2011–2017, https://doi.org/10.1021/am4050772.
[280] J.C. Kays, A.M. Saeboe, R. Toufanian, D.E. Kurant, A.M. Dennis, Shell-Free Copper Indium Sulfide Quantum Dots Induce Toxicity in Vitro and in Vivo, Nano Lett. 20 (2020) 1980–1991, https://doi.org/10.1021/acs.nanolett.9b05259.
[281] W. Zou, L. Li, Y. Chen, T. Chen, Z. Yang, J. Wang, D. Liu, G. Lin, X. Wang, vivo toxicity evaluation of PEGylated CuInS2/ZnS quantum dots in BALB/c mice, Front Pharm. 10 (2019) 437, https://doi.org/10.3389/fphar.2019.00437.
[282] T. Uematsu, K. Wajima, D.K. Sharma, S. Hirata, T. Yamamoto, T. Kameyama, M. Vacha, T. Torimoto, S. Kuwabata, Narrow band-edge photoluminescence from AgInS2 semiconductor nanoparticles by the formation of amorphous III–VI semiconductor shells, NPG Asia Mater. 10 (2018) 713–726, https://doi.org/10.1038/s41427-018-0067-9.
[283] I. Tsuji, H. Kato, H. Kobayashi, A. Kudo, Photocatalytic H2 evolution reaction from aqueous solutions over band structure-controlled (Agln)xZn2(1-x)S2 solid solution photocatalysts with visible-light response and their surface nanostructures, J. Am. Chem. Soc. 126 (2004) 13406–13413, https://doi.org/10.1021/ja048296m.
[284] T. Torimoto, T. Adachi, K.I. Okazaki, M. Sakuraoka, T. Shibayama, B. Ohtani, A. Kudo, S. Kuwabata, Facile synthesis of ZnS-AglnS2 solid solution nanoparticles for a color-adjustable luminophore, J. Am. Chem. Soc. 129 (2007) 12388–12389, https://doi.org/10.1021/ja0750470.
[285] A. Hirase, Y. Hamanaka, T. Kuzuya, Ligand-Induced Luminescence Transformation in AgInS2 Nanoparticles: From Defect Emission to Band-Edge Emission, J. Phys. Chem. Lett. 11 (2020) 3969–3974, https://doi.org/10.1021/acs.jpclett.0c01197.
[286] W. Xiang, C. Xie, J. Wang, J. Zhong, X. Liang, H. Yang, L. Luo, Z. Chen, Studies on highly luminescent AgInS2 and Ag-Zn-In-S quantum dots, J. Alloy. Compd. 588 (2014) 114–121, https://doi.org/10.1016/j.jallcom.2013.10.188.
[287] J. Song, C. Ma, W. Zhang, X. Li, W. Zhang, R. Wu, X. Cheng, A. Ali, M. Yang, L. Zhu, R. Xia, X. Xu, Bandgap and Structure Engineering via Cation Exchange: From Binary Ag2S to Ternary AgInS2, Quaternary AgZnInS alloy and AgZnInS/ZnS Core/Shell Fluorescent Nanocrystals for Bioimaging, ACS Appl. Mater. Interfaces 8 (2016) 24826–24836, https://doi.org/10.1021/acsami.6b07768.
[288] P.N. Li, A.V. Ghule, J.Y. Chang, Direct aqueous synthesis of quantum dots for high-performance AgInSe2 quantum-dot-sensitized solar cell, J. Power Sources 354 (2017) 100–107, https://doi.org/10.1016/j.jpowsour.2017.04.040.
[289] N.D. Abazović, M.I. Čomor, M.N. Mitrić, E. Piscopiello, T. Radetić, I.A. Janković, J.M. Nedeljković, Ligand mediated synthesis of AgInSe2 nanoparticles with tetragonal/orthorhombic crystal phases, J. Nanopart. Res 14 (2012) 810, https://doi.org/10.1007/s11051-012-0810-z.
[290] D. Che, X. Zhu, H. Wang, Y. Duan, Q. Zhang, Y. Li, Aqueous synthesis of high bright and tunable near-infrared AgInSe2-ZnSe quantum dots for bioimaging, J. Colloid Interface Sci. 463 (2016) 1–7, https://doi.org/10.1016/j.jcis.2015.10.039.
[291] M.D. Regulacio, K.Y. Win, S.L. Lo, S.Y. Zhang, X. Zhang, S. Wang, M.Y. Han, Y. Zheng, Aqueous synthesis of highly luminescent AgInS2-ZnS quantum dots and their biological applications, Nanoscale 5 (2013) 2322–2327, https://doi.org/10.1039/c3nr34159c.
[292] D.Y. Jo, H. Yang, Synthesis of highly white-fluorescent Cu-Ga-S quantum dots for solid-state lighting devices, Chem. Commun. 52 (2016) 709–712, https://doi.org/10.1039/c5cc07968c.
[293] B.Y. Kim, J.H. Kim, K.H. Lee, E.P. Jang, C.Y. Han, J.H. Jo, H.S. Jang, H. Yang, Synthesis of highly efficient azure-to-blue-emitting Zn-Cu-Ga-S quantum dots, Chem. Commun. 53 (2017) 4088–4091, https://doi.org/10.1039/c7cc00952f.
[294] M.A. Haque, A. Lohar, Y. Jadhav, R. Kumar, S.N. Jha, D. Bhattacharyya, S. Jadkar, S. Sartale, S. Mahamuni, Zn alloying strategy to improve the photoluminescence of CuGaS2/ZnS core/shell quantum dots, J. Mater. Chem. A 12 (2024) 10726–10736, https://doi.org/10.1039/d4ta01134a.
[295] S.O.M. Hinterding, A.C. Berends, M. Kurttepeli, M.E. Moret, J.D. Meeldijk, S. Bals, W. Van Der Stam, C. De Mello Donega, Tailoring Cu+ for Ga3+ Cation Exchange in Cu2- xS and CuInS2 Nanocrystals by Controlling the Ga Precursor Chemistry, ACS Nano 13 (2019) 12880–12893, https://doi.org/10.1021/acsnano.9b05337.

[296] Y. Duan, M. Shim, Kinetics of Concurrent Seed Growth and Cation Exchange in Transforming Cu2-xS Nanocrystals to CuGaS2 Nanorods, J. Am. Chem. Soc. 147 (2025) 9566–9575, https://doi.org/10.1021/jacs.4c17582.
[297] S. Das Adhikari, A. Dutta, G. Prusty, P. Sahu, N. Pradhan, Symmetry Break and Seeded 2D Anisotropic Growth in Ternary CuGaS2 Nanocrystals, Chem. Mater. 29 (2017) 5384–5393, https://doi.org/10.1021/acs.chemmater.7b01775.
[298] W. Niu, X. Xie, Z. Chen, R. Sun, Y. Li, S. Wang, Y. Zhang, C. Yang, A. Tang, Realization of Narrow-Bandwidth Cu-Ga-S-Based Quantum Dots with Controllable Luminescence, Adv. Opt. Mater. 12 (2024), https://doi.org/10.1002/adom.202400762.
[299] J. Tang, S. Hinds, S.O. Kelley, E.H. Sargent, Synthesis of colloidal CuGaSe2, CuInSe2, and Cu(InGa)Se2 nanoparticles, Chem. Mater. 20 (2008) 6906–6910, https://doi.org/10.1021/cm801655w.
[300] T. Bai, X. Wang, Y. Dong, S. Xing, Z. Shi, S. Feng, One-pot synthesis of high-quality AgGaS2/ZnS-based photoluminescent nanocrystals with widely tunable band gap, Inorg. Chem. 59 (2020) 5975–5982, https://doi.org/10.1021/acs.inorgchem.9b03768.
[301] J.-H. Kim, S.-Y. Yoon, K.-H. Kim, H.-B. Lim, H.-J. Kim, H. Yang, Electroluminescence from two I–III–VI quantum dots of A–Ga–S (A=Cu, Ag, Opt. Lett. 43 (2018) 5287, https://doi.org/10.1364/ol.43.005287.
[302] X. Li, X. Tong, S. Yue, C. Liu, A.I. Channa, Y. You, R. Wang, Z. Long, Z. Zhang, Z. Zhao, X.F. Liu, Z.M. Wang, Rational design of colloidal AgGaS2/CdSeS core/shell quantum dots for solar energy conversion and light detection, Nano Energy 89 (2021), https://doi.org/10.1016/j.nanoen.2021.106392.
[303] X. Li, X. Tong, L. Xia, H. Zhao, J. Luo, Z. Li, Z.M. Wang, Modulating Eco-friendly Colloidal AgGaS2 Quantum Dots for Highly Efficient Photodetection and Image Sensing via Direct Growth of Ternary AgInS2 Shell, Small 20 (2024), https://doi.org/10.1002/smll.202404261.
[304] M. Tozawa, S. Ofuji, M. Tanaka, K. Akiyoshi, T. Kameyama, T. Yamamoto, G. Motomura, Y. Fujisaki, T. Uematsu, S. Kuwabata, T. Torimoto, Spectrally Narrow Blue-Light Emission from Nonstoichiometric AgGaS2 Quantum Dots for Application to Light-Emitting Diodes, ACS Appl. Mater. Interfaces 16 (2024) 68169–68180, https://doi.org/10.1021/acsami.4c13987.
[305] J.H. Kim, B.Y. Kim, E.P. Jang, S.Y. Yoon, K.H. Kim, Y.R. Do, H. Yang, Synthesis of widely emission-tunable Ag-Ga-S and its quaternary derivative quantum dots, Chem. Eng. J. 347 (2018) 791–797, https://doi.org/10.1016/j.cej.2018.04.167.
[306] R.S. Feigelson, R.K. Route, Improvements in the optical quality of AgGaSe2 crystals, Mater. Reas Bull. 25 (1990) 1503–1511, https://doi.org/10.1016/0025-5408(90)90127-N.
[307] N. Rismaningsih, H. Yamauchi, T. Kameyama, T. Yamamoto, S. Morita, H. Yukawa, T. Uematsu, Y. Baba, S. Kuwabata, T. Torimoto, Photoluminescence properties of quinary Ag-(In,Ga)-(S,Se) quantum dots with a gradient alloy structure for in vivo bioimaging, J. Mater. Chem. C Mater. 9 (2021) 12791–12801, https://doi.org/10.1039/d1tc02746h.
[308] T. Kameyama, H. Yamauchi, T. Yamamoto, T. Mizumaki, H. Yukawa, M. Yamamoto, S. Ikeda, T. Uematsu, Y. Baba, S. Kuwabata, T. Torimoto, Tailored Photoluminescence Properties of Ag(In,Ga)Se2 Quantum Dots for Near-Infrared in Vivo Imaging, ACS Appl. Nano Mater. 3 (2020) 3275–3287, https://doi.org/10.1021/acsanm.9b02608.
[309] T. Li, C. Liu, R. Li, X. Huang, X. Qi, X. Mi, T. Bai, S. Xing, Luminescent AgGaSe2/ZnSe nanocrystals: rapid synthesis, color tunability, aqueous phase transfer, and bio-labeling application, Dalton Trans. 52 (2023) 4554–4561, https://doi.org/10.1039/d2dt03979f.
[310] X. Huangfu, Y. Shen, A. Yang, L. Liu, W. Luo, W. Zhao, Synthesis of water soluble CuGaS2/ZnS quantum dots for ultrasensitive fluorescent detection of alkaline phosphatase based on inner filter effect, Colloids Surf. B Biointerfaces 191 (2020), https://doi.org/10.1016/j.colsurfb.2020.110984.
[311] A. Anas, H. Akita, H. Harashima, T. Itoh, M. Ishikawa, V. Biju, Photosensitized breakage and damage of DNA by CdSe− ZnS, Quantum dots J. Phys. Chem. B 112 (2008) 10005–10011, https://doi.org/10.1021/jp8018606.
[312] S. Yamashita, M. Hamada, S. Nakanishi, H. Saito, Y. Nosaka, S. Wakida, V. Biju, Auger ionization beats photo-oxidation of semiconductor quantum dots: extended stability of single-molecule photoluminescence, Angew. Chem. Int 54 (2015) 3892–3896, https://doi.org/10.1002/anie.201501131.
[313] S.S. Lucky, K.C. Soo, Y. Zhang, Nanoparticles in photodynamic therapy, Chem. Rev. 115 (2015) 1990–2042, https://doi.org/10.1021/cr5004198.
[314] A.P. Castano, P. Mroz, M.R. Hamblin, Photodynamic therapy and anti-tumour immunity, Nat. Rev. Cancer 6 (2006) 535–545, https://doi.org/10.1038/nrc1894.
[315] V. Biju, Chemical modifications and bioconjugate reactions of nanomaterials for sensing, imaging, drug delivery and therapy, Chem. Soc. Rev. 43 (2014) 744–764, https://doi.org/10.1039/c3cs60273g.
[316] D.K. Chatterjee, L.S. Fong, Y. Zhang, Nanoparticles in photodynamic therapy: An emerging paradigm, Adv. Drug Deliv. Rev. 60 (2008) 1627–1637, https://doi.org/10.1016/j.addr.2008.08.003.
[317] A.C.S. Samia, X. Chen, C. Burda, Semiconductor quantum dots for photodynamic therapy, J. Am. Chem. Soc. 125 (2003) 15736–15737, https://doi.org/10.1021/ja0386905.
[318] S. Roy, N. Bag, S. Bardhan, I. Hasan, B. Guo, Recent progress in NIR-II fluorescence imaging-guided drug delivery for cancer theranostics, Adv. Drug Deliv. Rev. 197 (2023), https://doi.org/10.1016/j.addr.2023.114821.
[319] C. Dong, Q. Yi, W. Fang, J. Zhang, A mini review of nanomaterials on photodynamic therapy, J. Photochem. Photo C: Photochem. Rev. 54 (2023), https://doi.org/10.1016/j.jphotochemrev.2022.100568.
[320] L. Peng, M. He, B. Chen, Q. Wu, Z. Zhang, D. Pang, Y. Zhu, B. Hu, Cellular uptake, elimination and toxicity of CdSe/ZnS quantum dots in HepG2 cells, Biomaterials 34 (2013) 9545–9558, https://doi.org/10.1016/j.biomaterials.2013.08.038.
[321] Q. Wu, M. Chu, Y. Shao, F. Wo, D. Shi, Reduced graphene oxide conjugated with CuInS2/ZnS nanocrystals with low toxicity for enhanced photothermal and photodynamic cancer therapies, Carbon 108 (2016) 21–37, https://doi.org/10.1016/j.carbon.2016.06.070.
[322] A. Anas, J. Sobhanan, K.M. Sulfiya, C. Jasmin, P.K. Sreelakshmi, V. Biju, Advances in photodynamic antimicrobial chemotherapy, J. Photochem. Photobiol. C: Photochem. Rev. 49 (2021), https://doi.org/10.1016/j.jphotochemrev.2021.100452.
[323] E.S. Shibu, M. Hamada, N. Murase, V. Biju, Nanomaterials formulations for photothermal and photodynamic therapy of cancer, J. Photochem. Photobiol. C: Photochem. Rev. 15 (2013) 53–72, https://doi.org/10.1016/j.jphotochemrev.2012.09.004.
[324] Y. Feng, L. Liu, S. Hu, Y. Liu, Y. Ren, X. Zhang, Förster resonance energy transfer properties of a new type of near-infrared excitation PDT photosensitizer: CuInS2/ZnS quantum dots-5-aminolevulinic acid conjugates, RSC Adv. 6 (2016) 55568–55576, https://doi.org/10.1039/c6ra06937a.
[325] E. Obeng, J. Feng, D. Wang, D. Zheng, B. Xiang, J. Shen, Multifunctional phototheranostic agent ZnO@Ag for anti-infection through photothermal/photodynamic therapy, Front Chem. 10 (2022), https://doi.org/10.3389/fchem.2022.1054739.
[326] H. Li, Z. Quan, W. Qi, X. Luo, L. Huang, S. Sun, Y. Xu, Conversion of Type II to Type I photosensitizers: Design strategies and recent advances for photodynamic therapy (Photochem Rev), J. Photochem. Photo C. 67 (2026), https://doi.org/10.1016/j.jphotochemrev.2026.100756.
[327] S.K. Maji, D.H. Kim, AgInS2-Coated Upconversion Nanoparticle as a Photocatalyst for Near-Infrared Light-Activated Photodynamic Therapy of Cancer Cells, ACS Appl. Bio Mater. 1 (2018) 1628–1638, https://doi.org/10.1021/acsabm.8b00467.
[328] X. Wu, J. Yang, J. Xing, Y. Lyu, R. Zou, X. Wang, J. Yao, D. Zhang, D. Qi, G. Shao, A. Wu, J. Li, Using host-guest interactions at the interface of quantum dots to load drug molecules for biocompatible, safe, and effective chemo-photodynamic therapy against cancer, J. Mater. Chem. B 11 (2023) 4855–4864, https://doi.org/10.1039/d3tb00592e.
[329] J. Sobhanan, K. Ono, T. Okamoto, M. Sawada, P.S. Weiss, V. Biju, Photosensitizer-singlet oxygen sensor conjugated silica nanoparticles for photodynamic therapy and bioimaging, Chem. Sci. 15 (2024) 2007–2018, https://doi.org/10.1039/D3SC03877G.
[330] J.M. Tsay, M. Trzoss, L. Shi, X. Kong, M. Selke, M.E. Jung, S. Weiss, Singlet, Oxyg. Prod. Pept. -Coat. Quantum Dot. -Photosensit. Conjug. J. Am. Chem. Soc. 129 (2007) 6865–6871, https://doi.org/10.1021/ja070713i.
[331] E. Yaghini, K.F. Pirker, C.W.M. Kay, A.M. Seifalian, A.J. Macrobert, Quantification of reactive oxygen species generation by photoexcitation of PEGylated quantum dots, Small 10 (2014) 5106–5115, https://doi.org/10.1002/smll.201401209.
[332] O.V. Ovchinnikov, S.V. Aslanov, T.S. Kondratenko, M.S. Smirnov, K.S. Chirkov, I. G. Grevtseva, D.A. Chentsov, Photocatalytic generation of reactive oxygen species in the presence of colloidal PbS quantum dots, J. Photochem. Photobiol. A Chem. 467 (2025), https://doi.org/10.1016/j.jphotochem.2025.116455.
[333] R. Yao, P. Sun, Y. Chen, Z. Lei, L. Wang, J. Yu, Y. Liu, W. Hailipitimu, W. Wei, J. Zhao, X. Qiu, NIR-Activated Ag2S Quantum Dots for Efficient Broad-Spectrum Antibacterial and Biofilm Disruption, Adv. Mater. Interfaces (2026), https://doi.org/10.1002/admi.202501030.
[334] X. Wu, M. Qi, C. Liu, Q. Yang, S. Li, F. Shi, X. Sun, L. Wang, C. Li, B. Dong, Near-infrared light-triggered nitric oxide nanocomposites for photodynamic/photothermal complementary therapy against periodontal biofilm in an animal model, Theranostics 13 (2023) 2350–2367, https://doi.org/10.7150/thno.83745.
[335] Y. Yao, Z. Wang, X. Huang, T. Wei, N. Liu, L. Zou, Y. Niu, Y. Hu, Q. Fang, X. Wang, D. Qiao, C. Li, M. Chen, S. Guan, Y. Xue, T. Wu, T. Zhang, M. Tang, Adverse Outcome Pathway-Based Strategies to Mitigate Ag2Se Quantum Dot-Induced Neurotoxicity, ACS Nano 19 (2025) 11029–11048, https://doi.org/10.1021/acsnano.4c16813.
[336] W. Białowąs, R. Boudjemaa, K. Steenkeste, P. Nyssen, M. Hoebeke, J. Lulek, M. P. Fontaine-Aupart, R. Schneider, Reactive oxygen species production by photoexcited (CuInS2)x(ZnS)1-x quantum dots and their phototoxicity towards Staphylococcus aureus bacteria, J. Photochem. Photobiol. A Chem. 446 (2024), https://doi.org/10.1016/j.jphotochem.2023.115165.
[337] Y. Zhang, M. Dai, Z. Yuan, Methods for the detection of reactive oxygen species, Anal. Methods 10 (2018) 4625–4638, https://doi.org/10.1039/c8ay01339j.
[338] M. Hashemkhani, G. Demirci, A. Bayir, A. Muti, A. Sennaroglu, L. Mohammad Hadi, E. Yaghini, M. Loizidou, A.J. Macrobert, H. Yagci Acar, Cetuximab-Ag2S quantum dots for fluorescence imaging and highly effective combination of ALA-based photodynamic/chemo-therapy of colorectal cancer cells, Nanoscale 13 (2021) 14879–14899, https://doi.org/10.1039/d1nr03507j.
[339] M. Hashemkhani, E. Celikbas, M. Khan, A. Sennaroglu, H. Yagci Acar, ALA/Ag2S/MnO2 Hybrid Nanoparticles for Near-Infrared Image-Guided Long-Wavelength Phototherapy of Breast Cancer, ACS Biomater. Sci. Eng. 9 (2023) 4126–4137, https://doi.org/10.1021/acsbiomaterials.3c00105.
[340] A.K. Lakshmanan, M. Gunaseelan, G. Nalupurackal, A. Thirumalai, A. Girigoswami, B. Roy, J. Senthilselvan, Facile synthesis of a NaYF4:Yb,Er-Ag2S nanocomposite, upconversion emission, microbubble formation by optical tweezers, and in vitro photodynamic therapy studies, New J. Chem. 49 (2025) 13292–13303, https://doi.org/10.1039/d5nj00348b.

[341] G. Charron, T. Stuchinskaya, D.R. Edwards, D.A. Russell, T. Nann, Insights into the mechanism of quantum dot-sensitized singlet oxygen production for photodynamic therapy, J. Phys. Chem. C 116 (2012) 9334–9342, https://doi.org/10.1021/jp301103f.
[342] C. Ren, D. Hu, Y. Cui, P. Chen, X. Xu, J. Cheng, T. He, Ag-doped InP/ZnS quantum dots for type-I photosensitizers, Chem. Commun. 59 (2023) 2311–2314, https://doi.org/10.1039/d2cc06119h.
[343] S.H. Chen, W.W. Huang, K. Dehvari, Y.C. Ling, A.V. Ghule, S.L. Tsai, J.Y. Chang, Photosensitizer–conjugated Cu-In-S heterostructured nanorods for cancer targeted photothermal/photodynamic synergistic therapy, Mater. Sci. Eng. C 97 (2019) 793–802, https://doi.org/10.1016/j.msec.2018.12.107.
[344] N. Tsolekile, V. Ncapayi, S. Parani, E.H.M. Sakho, M.C. Matoetoe, S.P. Songca, O. S. Oluwafemi, Synthesis of fluorescent CuInS2/ZnS quantum dots - porphyrin conjugates for photodynamic therapy, MRS Commun. 8 (2018) 398–403, https://doi.org/10.1557/mrc.2018.60.
[345] S.K. Maji, Luminescence-tunable ZnS-AgInS2 nanocrystals for cancer cell imaging and photodynamic therapy, ACS Appl. Bio Mater. 5 (2022) 1230–1238, https://doi.org/10.1021/acsabm.1c01247.
[346] M. Hashemkhani, M. Loizidou, A.J. Macrobert, H. Yagci Acar, One-step aqueous synthesis of anionic and cationic AgInS2 quantum dots and their utility in improving the efficacy of ALA-based photodynamic therapy, Inorg. Chem. 61 (2022) 2846–2863, https://doi.org/10.1021/acs.inorgchem.1c03298.
[347] T. Yang, Y. Tang, L. Liu, X. Lv, Q. Wang, H. Ke, Y. Deng, H. Yang, X. Yang, G. Liu, Y. Zhao, H. Chen, Size-dependent Ag2S nanodots for second near-infrared fluorescence/photoacoustics imaging and simultaneous photothermal therapy, ACS Nano 11 (2017) 1848–1857, https://doi.org/10.1021/acsnano.6b07866.
[348] M.S. Kim, I.H. Nam, H.J. Cha, Y.K. Jo, Bandgap-engineered proteinic near-infrared nanodots for localized precision cancer theranostics, J. Nanobiotechnol 23 (2025) 541, https://doi.org/10.1186/s12951-025-03619-0.
[349] H. Wang, J. You, D. Shi, L. Cai, H. Shi, H. Shi, Multifunctional Ag2S/g-C3N4 nanoparticles for photodynamic and photothermal cancer therapy under near-infrared excitation, ACS Appl. Nano Mater. 7 (2024) 19904–19914, https://doi.org/10.1021/acsanm.4c01221.
[350] B. Shi, J. Hua, C. Huang, R. Xiong, D. Miao, Photothermal nanomaterials for biomedical therapy and diagnosis: from photothermal conversion mechanisms to clinical translation, J. Photochem. Photobiol. C Photochem. Rev. 66 (2026), https://doi.org/10.1016/j.jphotochemrev.2026.100736.
[351] E. Celikbas, A. Saymaz, H. Gunduz, I. Koc, E. Cakir, A. Sennaroglu, S. Kolemen, H. Yagci Acar, K. Onbasli, Image-guided enhanced PDT/PTT combination therapy using brominated hemicyanine-loaded folate receptor-targeting Ag2S quantum dots, Bioconjug Chem. 34 (2023) 880–892, https://doi.org/10.1021/acs.bioconjchem.3c00096.
[352] K. Cheng, X.S. Zhang, J. An, C. Li, R.Y. Zhang, R. Ye, B.J. Ye, B. Liu, Y. Di Zhao, Hitherto-unexplored photodynamic therapy of Ag2S and enhanced regulation based on polydopamine in vitro and vivo, Chem. Eur. J. 25 (2019) 7553–7560, https://doi.org/10.1002/chem.201900718.
[353] D. Song, S. Chi, X. Li, C. Wang, Z. Li, Z. Liu, Upconversion system with quantum dots as sensitizer: improved photoluminescence and PDT efficiency, ACS Appl. Mater. Interfaces 11 (2019) 41100–41108, https://doi.org/10.1021/acsami.9b16237.
[354] K. Du, P. Lei, L. Dong, M. Zhang, X. Gao, S. Yao, J. Feng, H. Zhang, situ decorating of ultrasmall Ag2Se on upconversion nanoparticles as novel nanotheranostic agent for multimodal imaging-guided cancer photothermal therapy, Appl. Mater. Today 18 (2020), https://doi.org/10.1016/j.apmt.2019.100497.
[355] C. Hu, L. Cai, S. Liu, M. Pang, Integration of a highly monodisperse covalent organic framework photosensitizer with cation exchange synthesized Ag2Se nanoparticles for enhanced phototherapy, Chem. Commun. 55 (2019) 9164–9167, https://doi.org/10.1039/c9cc04668b.
[356] J. Wu, H. Wei, Y. Wei, T. Deng, Y. Wang, Y. Qiu, Y. Zhang, Spatiotemporal synergism in osteomyelitis treatment with photoactivated core-shell zinc oxide/silver sulfide heterogeneous nanoparticles, ACS Appl. Mater. Interfaces 16 (2024) 11194–11205, https://doi.org/10.1021/acsami.3c16546.
[357] X. Xie, J. Wei, B. Zhang, W. Xiong, Z. He, Y. Zhang, C. Gao, Y. Zhao, B. Liu, A self-assembled bilayer polypeptide-engineered hydrogel for spatiotemporal modulation of bactericidal and anti-inflammation process in osteomyelitis treatment, J. Nanobiotechnology 20 (2022) 416, https://doi.org/10.1186/s12951-022-01614-3.
[358] J. Wu, T. Deng, Q. Wu, Y. Qiu, Y. Wei, Q. Zhao, Y. Zhang, NIR-responsive GO/Ag2S heterostructure for rapid bacteria-killing and wound healing, Appl. Mater. Today 32 (2023), https://doi.org/10.1016/j.apmt.2023.101826.
[359] J.G. Kim, J. Sun, Y. Zhao, J. Wen, B. Zhou, Z. Zhang, S. Mo, J. Wang, H. Liu, G. Wang, Q. Yu, M. Liu, Electronic structure modulation of Ag2S by vacancy engineering for efficient bacterial infection, Small 18 (2022), https://doi.org/10.1002/smll.202107807.
[360] N.A. Pechnikova, K. Domvri, K. Porpodis, M.S. Istomina, A.V. Iaremenko, A. V. Yaremenko, Carbon quantum dots in biomedical applications: advances, challenges, and future prospects, Aggregate 6 (2025) e707, https://doi.org/10.1002/agt2.707.
[361] D. Yang, G. Yang, Q. Sun, S. Gai, F. He, Y. Dai, C. Zhong, P. Yang, Carbon-dot-decorated TiO2 nanotubes toward photodynamic therapy based on water-splitting mechanism, Adv. Healthc. Mater. 7 (2018), https://doi.org/10.1002/adhm.201800042.
[362] H. Zhang, Y. Shan, L. Dong, A comparison of TiO2and ZnO nanoparticles as photosensitizers in photodynamic therapy for cancer, J. Biomed. Nanotechnol. 10 (2014) 1450–1457, https://doi.org/10.1166/jbn.2014.1961.
[363] Z. Luo, Q. Wu, J. Xue, Y. Ding, Selectively enhanced antibacterial effects and ultraviolet activation of antibiotics with ZnO nanorods against Escherichia coli, J. Biomed. Nanotechnol. 9 (2013) 69–76, https://doi.org/10.1166/jbn.2013.1472.
[364] J. Yang, Q. Han, L. Li, R. Zhang, Visible-light-driven TiO2/Pt nanozyme-embedded dressings: integrating PDT, oxygenation, and biomechanical support for pressure ulcer repair, Small 21 (2025) e05278, https://doi.org/10.1002/smll.202505278.
[365] H. Nosrati, M. Heydari, Titanium dioxide nanoparticles: a promising candidate for wound healing applications, Burns Trauma 13 (2025) tkae069, https://doi.org/10.1093/burnst/tkae069.
[366] A. Maladan, T. Okamoto, M. Kumar, M.F. Khatun, Y. Matsuo, C. Subrahmanyam, V. Biju, Colloidally synthesized and bandgap-engineered luminescent titanium nitride quantum dots, Nanoscale 17 (2025) 25484–25489, https://doi.org/10.1039/D5NR03290C.

S L Aneesha is a doctoral student at Hokkaido University. She completed her master's in Chemistry from the National Institute of Technology Meghalaya in 2023. Subsequently, she was a visiting student at the Indian Institute of Technology Hyderabad and Hokkaido University. Since April 2024, she has been a MEXT research student and a Ph.D. scholar at Hokkaido University.

Jeladhara Sobhanan completed her Ph. D. in Environmental Materials Chemistry from Hokkaido University in 2023. Subsequently, she was a postdoctoral fellow at Rice University and a research associate at Baylor College of Medicine. Since 2025, she has been a staff member at Virginia Commonwealth University. Her research interests include quantum dots and bioimaging.

Jose V. Rival completed his Ph. D. in Chemistry from the University of Calicut in 2025. Subsequently, he joined Tohoku University as a postdoctoral researcher. His research interests include quantum clusters and other luminescent materials.

Edakkattuparambil Sidharth Shibu is an assistant Professor at the University of Calicut. He obtained his Ph.D. degree in Chemistry from the Indian Institute of Technology Madras. Subsequently, during 2011–2014, he was a Research Associate and a JSPS postdoctoral fellow at AIST, Japan. During 2014–2016, he was a Marie Sklodowska Curie Postdoctoral Fellow at the University of Bordeaux. Later, he was a scientist at the CSIR-Central Electrochemical Research Institute, India. His research interests include lumincent nanomaterials and quantum clusters.

Abdulaziz Anas is a Senior Principal Scientist at the CSIR-National Institute of Oceanography. He obtained his Ph.D. in Marine Biotechnology. Subsequently, he was a postdoctoral fellow at AIST, Japan. His research interests include environmental microbiology, environmental toxicology, bioimaging, and luminescent nanomaterials.

Bengang Xing is a chemical biologist specializing in molecular imaging, nanomedicine, and chemical biology. He was previously a professor at Nanyang Technological University, Singapore. He is currently a Chair Professor at The Hong Kong Polytechnic University, where his research focuses on molecular probes, bioimaging, and nanotheranostic systems for disease diagnosis and therapy.

Vasudevanpillai Biju is a Chemistry Professor at Hokkaido University. He is also a visiting professor at the Indian Institute of Technology Hyderabad and a distinguished professor at the University of Calicut. He is the recipient of the 2025 Presidential Award for Excellence in Teaching and Research and the 2024 Japanese Photochemistry Association Award. His research interests include low-dimensional luminescent materials.